DIPLOMARBEIT

Determination of the relative slow pion efficiency using 72/fb of Belle II experimental data collected in the years 2019/2020

zur Erlangung des akademischen Grades

Diplom-Ingenieur

im Rahmen des Studiums

066 461 Technische Physik

unter der Anleitung von

Privatdoz. Dipl.-Ing. Dr.techn. Christoph Schwanda

eingereicht von

Sebastian Dorer, BSc

Matrikelnummer: 01525332

ausgeführt am Atominstitut
der Fakultät für Physik der Technischen Universität Wien
in Zusammenarbeit mit dem Institut für Hochenergiephysik
der Österreichischen Akademie der Wissenschaften

Wien, 06.12.2021

_____ _____
Unterschrift Verfasser   Unterschrift Betreuer

Zusammenfassung

Das Ziel dieser Diplomarbeit ist die Untersuchung der Track-Rekonstruktionseffizienz langsamer Pionen bei Belle II, welche bei $D^{*-} \to \bar{D}^0 \pi_s^-$ Zerfällen entstehen. Die Motivation zur Durchführung dieser Arbeit liegt in dem Streben nach einer Steigerung der Präzision der experimentellen Messungen von $B^0 \to D^{*-} l^+ \nu_l$ Zerfällen, mit $l \in \{e, \mu\}$, begründet. Es besteht spezielles Interesse an $B^0 \to D^{*-} l^+ \nu_l$ Zerfällen, da diese zur Bestimmung des Cabibbo-Kobayashi-Maskawa Matrixelements $|V_{cb}|$ verwendet werden können.

Die Cabibbo-Kobayashi-Maskawa Matrixelemente spielen eine äußerst relevante Rolle für die Erforschung des Standardmodells der Teilchenphysik und mögliche Erweiterungen jenseits des derzeitigen Standardmodells. Daher besteht die Notwendigkeit, diese Matrixelemente mit möglichst hoher Präzision bestimmen zu können.

Die Extraktion von $|V_{cb}|$ aus experimentellen Messungen von $B^0 \to D^{*-} l^+ \nu_l$ Zerfällen wird von Dungel et al. in [24] ausführlich beschrieben. Aus diesem Paper geht auch hervor, dass etwaige Unsicherheiten der Track-Rekonstruktion langsamer Pionen direkten Einfluss auf die Genauigkeit der $|V_{cb}|$ Berechnung haben.

Diese Unsicherheit der Track-Rekonstruktionseffizienz langsamer Pionen liegt bei dem Belle II Experiment derzeit bei etwa 10 % [21], und damit deutlich höher als noch bei dem Vorgängerexperiment Belle mit etwa 1.3 % [24]. Um auf der Grundlage der Daten des neuen Bellen II Experiments kompetitive $|V_{cb}|$ Berechnungen zu ermöglichen, ist daher eine Reduktion dieser Unsicherheit notwendig, da diese zurzeit die gesamte Unsicherheit des $|V_{cb}|$ Wertes maßgeblich dominiert.

Im Rahmen dieser Diplomarbeit wurden vier D^0 Zerfallsmoden aus $B^0 \to D^{*-} \pi^+ \to \left(\bar{D}^0 \pi_s^- \right) \pi^+$ Zerfällen analysiert, um die Rekonstruktionseffizienz langsamer Pionen zu untersuchen. Hierfür wurden 72 fb^{-1} Realdaten des Belle II Experiments und 200 fb^{-1} aus Monte-Carlo Simulationen verwendet. Die Rekonstruktion der B^0 Mesonen erfolgte mittels Belle II analysis software framework `basf2` und das Fitten der Simulationsdaten an die realen Daten mit Hilfe von `TFractionFitter`. Aus den Ergebnissen der Fits wurden Yield-ratios berechnet, die als Maß der Rekonstruktionseffizienz dienen. Nachdem keine signifikanten Abweichungen der Yield-ratios von deren Sollwert beobachtet werden konnten, bestand keine Notwendigkeit, Korrekturfaktoren für die langsamen Pionen einzuführen. Die Unsicherheit der Tracking-Effizienz der langsamen Pionen konnte schließlich im Laufe dieser Diplomarbeit auf 4.06 % reduziert werden.

Ein Vergleich mit den aktuellen Ergebnissen von Chaoyi Lyu [11] zeigt eine hohe Kompatibilität der beiden unabhängig voneinander durchgeführten Untersuchungen.

i

Abstract

The main goal of this thesis is the investigation of the tracking efficiency of slow pions, that are produced at $D^{*-} \to \bar{D}^0 \pi_s^-$ decays, at Belle II. This analysis is motivated by the efforts of increasing the precision of the experimental measurement of $B^0 \to D^{*-} l^+ \nu_l$ decays, with $l \in \{e, \mu\}$, since they provide the opportunity of extracting the Cabibbo-Kobayashi-Maskawa matrix element $|V_{cb}|$.

Due to its profound linkage to numerous elementary particle physics processes, the Cabibbo-Kobayashi-Maskawa matrix is of utmost importance for the quest of gaining a deeper understanding of the Standard Model of particle physics and possibly pushing the boundaries of physics into new, yet to be explored, realms beyond the Standard Model. Therefore, seeking high precision measurements of the matrix elements is necessary.

The numerical extraction of $|V_{cb}|$ from experimental measurements of $B^0 \to D^{*-} l^+ \nu_l$ decays is described in detail by Dungel et al. in [24]. Moreover, the dependence of the final $|V_{cb}|$ result on the uncertainty of slow pions, using the proposed method, is shown in this paper. Thus, any increase of the slow pion tracking precision will be directly beneficial for the calculation of $|V_{cb}|$.

Currently, the uncertainty of the slow pion tracking efficiency at Belle II is considered to be about 10% [21], and therefore significantly higher than at its predecessor Belle with about 1.3 % [24]. Hence, in order to perform competitive $|V_{cb}|$ calculations based on data collected by the new Belle II experiment, a tremendous reduction of this uncertainty has to be achieved or otherwise, the $|V_{cb}|$ uncertainty is dominated by the slow pion uncertainty.

Over the course of this thesis, four different decay modes of D^0 mesons originating from $B^0 \to D^{*-} \pi^+ \to \left(\bar{D}^0 \pi_s^- \right) \pi^+$ decays have been analyzed to examine the slow pion reconstruction efficiency. This analysis is based on 72 fb^{-1} real data from the Belle II experiment and 200 fb^{-1} Monte Carlo simulated data. Using the Belle II analysis software framework `basf2`, the B^0 mesons were reconstructed. Fitting the Monte Carlo data to the experimental data was performed with `TFractionFitter`. From the fit results, the yield-ratios were calculated, which are used as a benchmark for the reconstruction efficiency. Since no significant deviations of the yield-ratios from unity were observed, there was no necessity to introduce correction factors for the slow pions. Finally, over the course of this thesis, the uncertainty of the slow pion tracking efficiency could be reduced to 4.06 %.

Comparing the outcome of this thesis with recent independent findings of Chaoyi Lyu [11], a good compatibility of the results can be seen.

Contents

Chapter 1

Introduction

While continuously pushing the boundaries of modern physics towards new unknown frontiers, particle physicists around the world made ground breaking discoveries in the field of high energy physics. Many of which influenced neighboring fields of study. One of those astonishing discoveries is the so called Cabibbo-Kobayashi-Maskawa matrix – or CKM matrix for short – named after its inventors. It is a 3×3 matrix describing how quarks are mixing with quarks of different flavors. Knowledge about the values of the CKM matrix provides the insight into the completeness of the current Standard Model of particle physics and possible extensions beyond the Standard Model. Therefore, precise measurements of the matrix elements are of utmost importance for modern particle physics.

One of its elements, $|V_{cb}|$ can be extracted from data of $B^0 \to D^{*-}l^+\nu_l$ decays, where $l \in \{e, \mu\}$. However, currently a large amount of systematic uncertainty in the results of branching ratio calculations of $B^0 \to D^{*-}l^+\nu_l$ decays is attributed by the tracking and reconstruction efficiency of slow pions [21]. Slow – sometimes also called *soft* – pions are produced in $D^{*-} \to \bar{D}^0\pi_s^-$ decays and their name originates from the small mass difference of D^{*-} and $\bar{D}^0$, which only allows for a momentum in the low hundreds of MeV range for the slow pions. At the moment, the uncertainty of the slow pion efficiency is about 10% [21]. The aim of this thesis is to improve the accuracy of slow pion momentum reconstructions, in order to render more precise $|V_{cb}|$ measurements in the future possible.

The analysis in this thesis is based on data from the Belle II experiment located at the particle physics research facility KEK in Tsukuba, Japan. The Belle II experiment in combination with SuperKEKB investigates B meson decays. The SuperKEKB asymmetric e^-e^+ particle collider produces $\Upsilon(4S)$ resonances, of which nearly all decay into $B\bar{B}$ meson pairs.

This thesis is structured into six chapters, of which this introduction marks the first one. Next, the underlying theory of the analysis performed for this thesis is explained in chapter 2. This chapter starts with a brief overview of the Standard Model of particle physics and the Cabibbo-Kobayashi-Maskawa matrix. It then guides the reader from the production of B mesons to the theoretical description of the experimental $|V_{cb}|$ CKM matrix element extraction from B decays and finally explains the slow pion tracking efficiency problem that motivates this thesis.

The subsequent chapter combines a general overview of commonly used types of particle accelerators and detectors and a description of their imple-

mentation at SuperKEKB and Belle II, in specific.

Due to its importance to the data analyzed in this thesis, chapter 4 focuses on the reconstruction of particle tracks from measurements of the different detectors at Belle II. This chapter describes how, starting from single hits in the detectors, the trajectories of particles can be reconstructed and particles themselves can be identified.

Chapter 5 is about the data analysis that has been performed over the course of this thesis. It includes a detailed description of the different steps of the analysis, their motivation, intermediate results, cross checks and the final result of the slow pion tracking efficiency uncertainty.

Lastly, chapter 6 provides a summary of the results, a recap about how they were obtained and an outlook for the application of the results.

Throughout this thesis natural units will be used. Additionally, the convention that $\hbar = c = 1$ is used unless $\hbar$ and c are explicitly written. Furthermore, for a given decay, for example $B^0 \rightarrow D^{*-}\pi^+$, its charge-conjugated counterpart, in the example case $\bar{B}^0 \rightarrow D^{*+}\pi^-$, is always implicitly included.

Chapter 2

Theory

2.1 Standard Model of particle physics

The hundreds of years long physicists' quest for discovering the mechanisms and inner workings of our world and the whole universe led to the development of one of the most precise physical theories to date with a rather unremarkable name – the Standard Model of particle physics. The Standard Model describes the elementary particles of which the matter in our universe is made of and their interactions. It is able to describe all physical forces excluding gravitation, which is still attempted to be included in a unified theory. The partitioning of the elementary particles into different categories in the Standard Model is shown in figure 2.1. Furthermore, the Standard Model has an underlying $SU(3)_C \otimes SU(2)_L \otimes U(1)_Y$ symmetry [35].

Using just those 17 elementary particles listed in figure 2.1, all matter surrounding us can be built and three fundamental forces – electromagnetism and the strong and weak nuclear forces – can be described. However, there are still open questions which cannot be explained by the Standard Model and there are other theories that expand beyond the Standard Model, for example the Grand Unified Theory (GUT) and theories with Super Symmetry (SUSY) [9].

2.1.1 Elementary particles

The two main categories of particles are fermions and bosons. Fermions have a spin of $\frac{2n+1}{2}$ with $n \in \mathbb{N}_0$, follow the Pauli exclusion principle and are the particles of which matter is made of. This group of particles contains leptons and quarks which come in three different generations that share the same physical properties and only differ in their mass, with each generation being more massive than the previous one. The first generation of fermions contains the up and down quarks, the electron and electron-neutrino. The charm and strange quarks, muon and muon-neutrino make up the second generation, and the third generation is composed of the top and bottom quarks, tau and tau-neutrino [9, 40].

Bosons have an integer spin, do not follow the Pauli exclusion principle and the ones shown in figure 2.1 are responsible for the interactions of fermions and are therefore force carrying particles known as gauge bosons. Currently, the Standard Model contains five types of bosons [9, 40]:

- **Photon**: The force carrying particle for electromagnetic interactions.
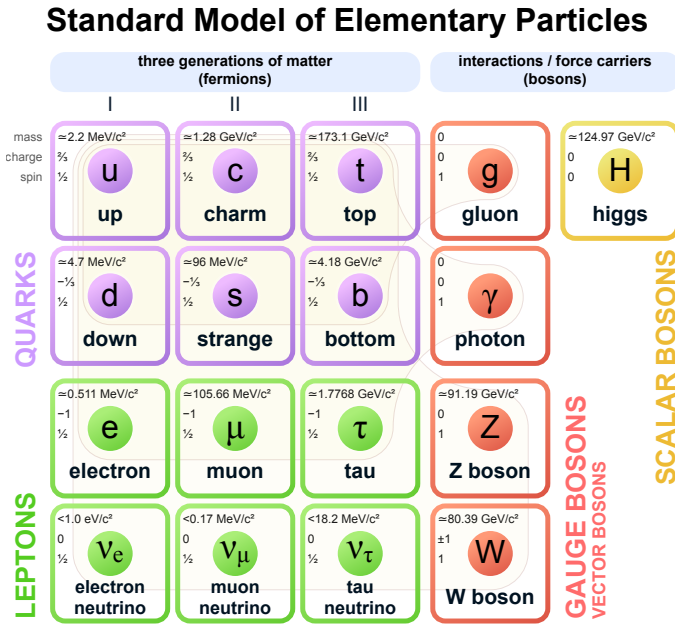
Standard Model of Elementary Particles

Figure 2.1: The Standard Model of particle physics [38].

- **Gluon**: Carries the force of the strong interaction, which "glues" quarks together to form hadrons like the proton and neutron.

- **Z^0**: Is the particle for the neutral weak interaction.

- **$W^\pm$**: Is responsible for the charged weak interaction.

- **Higgs-Boson**: Gives fermions mass via the Higgs-mechanism.

2.1.2 Fundamental forces

To our current knowledge, there are four fundamental forces: gravitation, electromagnetism and the strong and weak nuclear forces. With the exception of gravity, all of them are included in and explained by the Standard Model. To describe the fundamental forces in the Standard Model, there is one Quantum Field Theory for each.

For Electromagnetism this is Quantum Electrodynamics (QED), where the photon is the massless force carrying spin-1 particle. By the exchange of virtual photons, electromagnetic interactions between charged particles are described. Electromagnetism acts on all ten charged particles of the Standard Model – the six quarks, three leptons and the W boson. QED has a $U(1)$ symmetry, because it is invariant under arbitrary phase shifts which do not have physical impact on wave functions and are only a matter of convention [35]. For a simple QED scattering process, as it is shown in figure 2.2, the Lorentz-invariant matrix element can be written by using the Feynman rules for QED as

$$-i\mathcal{M} = \left[\bar{u}(p_3)\left\{ie\gamma^\mu\right\}u(p_1)\right]\frac{-ig_{\mu\nu}}{q^2}\left[\bar{u}(p_4)\left\{ie\gamma^\nu\right\}u(p_2)\right], \qquad (2.1)$$

where

$$\bar{u}(p_3)\left\{ie\gamma^\mu\right\}u(p_1) \qquad (2.2)$$

$$\bar{u}(p_4)\left\{ie\gamma^\nu\right\}u(p_2) \qquad (2.3)$$

are the contributions to the matrix element at the interaction vertices μ and ν with the Dirac spinors u and $\bar{u}$, and

$$\frac{-ig_{\mu\nu}}{q^2} \tag{2.4}$$

is the photon propagator, with $q^2 = (p_1 - p_3)^2$ [40]. The Feynman rules of QED provide a set of instructions for the combination of particles, vertices and propagators to form matrix elements directly from the corresponding Feynman diagrams without requiring rigorous quantum field theory calculations for each interaction [40].
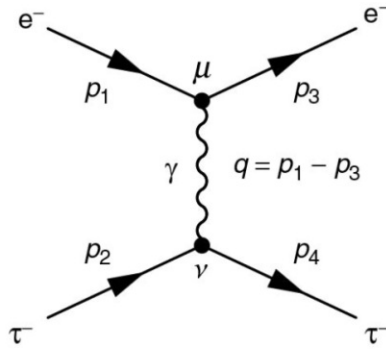

Figure 2.2: QED scattering process [40].

Quantum Chromodynamics (QCD) is the theory which describes the strong nuclear force mediated by eight massless gluons that only acts on quarks and binds them together to form hadrons, e.g. a proton is made up of two up quarks and one down quark, and two down quarks and one up quark form a neutron. However, building up some baryons (hadrons containing three quarks), a problem arises. For example, the Δ^{++} particle with $J_3 = \frac{3}{2}$ has a fully symmetric wave function

$$\left|\Delta^{++}\right\rangle = \left|uuu\right\rangle \left|\uparrow\uparrow\uparrow\right\rangle, \tag{2.5}$$

which is forbidden by the Pauli-exclusion principle, which states that the wave function of a system of identical fermions has to be antisymmetric. This discrepancy can be resolved by introducing a new internal property of quarks: color. Quarks come in three different colors, namely red, green and blue. Since hadrons have to be white or colorless for an observer, only $\left|q\bar{q}\right\rangle$ mesons and $\left|qqq\right\rangle$ baryons are possible. The three color states $\left|r\right\rangle$, $\left|g\right\rangle$ and $\left|b\right\rangle$ form an orthonormal basis within a three-dimensional complex vector space. The group $SU(3)_C$, where C stands for color, is formed by eight unitary matrices U with $\det U = 1$ of the color coordinate transformations

$$q'^i = U^i_k q^k \tag{2.6}$$

and eight real valued parameters [9]. The quark-quark-gluon interaction vertex for a strong interaction shown in figure 2.3 is given by [40]

$$-\frac{1}{2}ig_S\lambda^a_{ji}\left[\bar{u}(p_3)\gamma^\mu u(p_1)\right]. \tag{2.7}$$

The third fundamental force included in the Standard Model is the weak nuclear force mediated by the massive Z^0, W^+ and W^- bosons. Not only is it
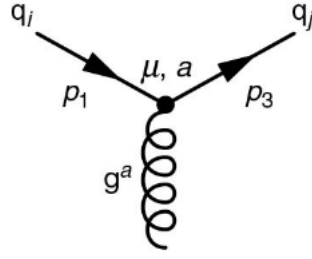
Figure 2.3: One example of a QCD vertex [40].

the only force with massive gauge bosons, but also in other ways very different from the electromagnetic and strong nuclear interaction [40]. This and the very high relevance of the weak interaction for semi-leptonic $B^0 \to D^{*-}l^+\nu_l$ decays necessitates a more in-depth review, in comparison to electromagnetism and the strong nuclear force, of the weak interaction in the next section.

2.1.3 The charged weak interaction

As mentioned before, contrary to QED and QCD the weak interaction is mediated by massive, charged gauge bosons $W^\pm$ and the massive, neutral gauge boson Z^0 and not by massless gauge bosons. It can act on all fermions in the Standard Model, with $W^\pm$ coupling fermions which differ by one unit of electric charge and Z^0 coupling fermions with the same amount of electric charge. As seen in the previous section, the interaction vertices of QED and QCD are of the same form with both being proportional to $\bar{u}(p_i)\gamma^\mu u(p_j)$. However, the interaction vertex of the weak nuclear force is completely different from those for QED and QCD, which also explains why the weak interaction is the only one in the Standard Model where parity conservation is violated [40].

By comparing the angular distribution of emitted electrons in the β-decay of ^{60}Co under parity transformations, Wu et al. [43] showed experimentally that the weak interaction involved in the beta decay does not conserve parity. Since the weak interaction violates parity conservation, the involved four-vector currents cannot be

$$j^\mu = \bar{u}(p_i)\gamma^\mu u(p_j), \tag{2.8}$$

as they are for QED and QCD, because four-vector currents of this form conserve parity by construction. From various constraints regarding the properties of the four-vector current, e.g. that they result in a Lorentz-invariant matrix element or that the Dirac-spinors are combined via products of γ-matrices, a general form for the fermion-boson interaction as a linear combination of bilinear covariants (in this case, vector (γ^μ) and axial vector ($\gamma^\mu\gamma^5$) currents) is given by

$$j^\mu \propto \bar{u}(p_i)\left(g_V\gamma^\mu + g_A\gamma^\mu\gamma^5\right)u(p_j) = g_V j_V^\mu + g_A j_A^\mu, \tag{2.9}$$

when spin-1 bosons are the exchanged particles. Here g_V and g_A are the vector and axial vector coupling constants and j_V^μ and j_A^μ are the vector and axial vector currents. With this mathematical framework and the knowledge that the weak charged current interaction is a $(V - A)$ interaction from experimental measurements, the weak charged current interaction vertex factor can be written as

$$\frac{-ig_W}{\sqrt{2}}\frac{1}{2}\gamma^\mu\left(1 - \gamma^5\right), \tag{2.10}$$

where g_W is the weak coupling constant [40].

Comparing this vertex factor to the chiral projection operators

$$P_R = \frac{1}{2}\left(1 + \gamma^5\right) \tag{2.11}$$

$$P_L = \frac{1}{2}\left(1 - \gamma^5\right), \tag{2.12}$$

which project out right- and left-handed chiral components of a Dirac-spinor, one sees that the weak interaction vertex already includes the left-handed projection operator P_L. Therefore, the weak interaction only acts on left-handed chiral particles and right-handed chiral antiparticles, since [40]

$$
\begin{aligned}
j_{RR}^\mu &= \frac{g_W}{\sqrt{2}}\bar{u}_R(p_i)\gamma^\mu\frac{1}{2}\left(1 - \gamma^5\right)u_R(p_j) \\
&= \frac{g_W}{\sqrt{2}}\bar{u}_R(p_i)\gamma^\mu\frac{1}{2}\underbrace{P_L P_R}_{=0}u(p_j) \\
&= 0,
\end{aligned} \tag{2.13}
$$

and

$$
\begin{aligned}
j_{LL}^\mu &= \frac{g_W}{\sqrt{2}}\bar{u}_L(p_i)\gamma^\mu\frac{1}{2}\left(1 - \gamma^5\right)u_L(p_j) \\
&= \frac{g_W}{\sqrt{2}}\bar{u}_L(p_i)\gamma^\mu\frac{1}{2}P_L u_L(p_j) \\
&\neq 0.
\end{aligned} \tag{2.14}
$$

The W-boson propagator can be calculated to be

$$\frac{-i}{q^2 - m_W^2}\left(g_{\mu\nu} - \frac{q_\mu q_\nu}{m_W^2}\right) \approx \frac{-ig_{\mu\nu}}{q^2 - m_W^2}, \tag{2.15}$$

where the approximation holds for $q^2 \ll m_W^2$ with the W-boson mass $m_W \approx 80.4$ GeV [40].

Furthermore, the weak interaction is based on the $SU(2)$ symmetry group and is combined with the $U(1)_Y$ symmetry of hypercharge through the electroweak theory to $SU(2)_L \otimes U(1)_Y$ [40].

2.2 Cabibbo-Kobayashi-Maskawa matrix

This section closely follows the references [9, 40].

Experiments, in which decay rates of different leptons where observed, showed that the strength of the weak interaction has the same value for all flavors of leptons. The comparison of branching ratios involving different lepton flavors results in

$$\frac{G_F^{(\tau)}}{G_F^{(\mu)}} = 1.0023 \pm 0.0033 \tag{2.16}$$

and

$$\frac{G_F^{(e)}}{G_F^{(\mu)}} = 1.000 \pm 0.004 \tag{2.17}$$

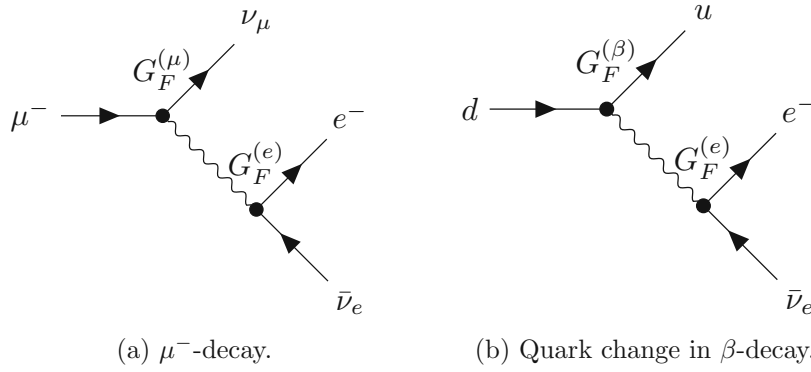(a) μ^--decay.　　　　(b) Quark change in β-decay.

Figure 2.4: Two weak interaction decays with different interaction strengths $G_F^{(\mu)}$ and $G_F^{(\beta)}$ (reproduction of figures in [40]).

for the ratios of the weak interaction coupling constants and therefore shows that $G_F^{(e)} = G_F^{(\mu)} = G_F^{(\tau)}$ [40].

However, a different behavior occurs when the weak interaction involves quarks instead of leptons. For example, by comparing the rates of μ^- and β^- decays depicted in figure 2.4, it can be found that

$$G_F^{(\mu)} = (1.1663787 \pm 0.0000006) \cdot 10^{-5} \text{ GeV}^{-2} \qquad (2.18)$$

and

$$G_F^{(\beta)} = (1.1066 \pm 0.0011) \cdot 10^{-5} \text{ GeV}^{-2} \qquad (2.19)$$

where $G_F^{(\mu)}$ and $G_F^{(\beta)}$ are the weak interaction strengths at the $\mu^-\nu_\mu W$ and duW vertices respectively. The study of other weak decays containing different quark flavors also showed that the weak coupling strengths are not universal for all quark flavors [40].

This discrepancy was first solved by the Cabibbo hypotheses. It states that there is a universal weak interaction coupling constant for leptons and quarks, however, the mass eigenstates and weak interaction eigenstates of quarks are different. The connection between the mass eigenstates d and s, and weak interaction eigenstates d' and s' between down and strange quarks is given by

$$\begin{pmatrix} d' \\ s' \end{pmatrix} = \begin{pmatrix} \cos(\theta_c) & \sin(\theta_c) \\ -\sin(\theta_c) & \cos(\theta_c) \end{pmatrix} \begin{pmatrix} d \\ s \end{pmatrix} \qquad (2.20)$$

with the Cabibbo angle θ_c. However, it is not possible to explain the observed phenomena of CP (charge and parity) violation with Cabibbo's 2×2 matrix, since it only has one real free parameter θ_c. Therefore, Kobayashi and Maskawa extended the Cabibbo hypotheses to a unitary 3×3 matrix, which offers 3 real and one complex free parameter. This occurrence of a phase factor enabled the description of CP violation and predicted a third generation of quarks (top and bottom), that subsequently has been experimentally found. This matrix is called Cabibbo-Kobayashi-Maskawa (CKM) matrix, which describes the relation between the mass and weak eigenstates of quarks by [40]

$$\begin{pmatrix} d' \\ s' \\ b' \end{pmatrix} = \underbrace{\begin{pmatrix} V_{ud} & V_{us} & V_{ub} \\ V_{cd} & V_{cs} & V_{cb} \\ V_{td} & V_{ts} & V_{tb} \end{pmatrix}}_{V_{\text{CKM}}} \begin{pmatrix} d \\ s \\ b \end{pmatrix}. \qquad (2.21)$$

The CKM matrix contains 9 parameters, of which 5 can be written as relative phase factors, so that 4 free parameters are left. Those parameters can be understood as 3 rotations in space and a complex phase, which allows the following representation of the CKM matrix [40, 9]

$$V_{\text{CKM}} = \begin{pmatrix} 1 & 0 & 0 \\ 0 & c(\phi_{23}) & s(\phi_{23}) \\ 0 & -s(\phi_{23}) & c(\phi_{23}) \end{pmatrix} \times \begin{pmatrix} c(\phi_{13}) & 0 & s(\phi_{13})e^{-i\delta} \\ 0 & 1 & 0 \\ -s(\phi_{13})e^{-i\delta} & 0 & c(\phi_{13}) \end{pmatrix}$$
$$\times \begin{pmatrix} c(\phi_{12}) & s(\phi_{12}) & 0 \\ -s(\phi_{12}) & c(\phi_{12}) & 0 \\ 0 & 0 & 1 \end{pmatrix} \quad (2.22)$$

where $s(\phi_{ij}) = \sin(\phi_{ij})$, $c(\phi_{ij}) = \cos(\phi_{ij})$, ϕ_{ij} is the angle between the quark generations and δ the complex phase. The complex phase δ is the origin of CP-violation in processes where quark flavors are changed [44]. Because of this complex phase, elements of V_{CKM} could be complex and therefore the absolute value of the elements is given below.

Another commonly used parametrization of the CKM matrix is the Wolfenstein parametrization [44]

$$V_{\text{CKM}} = \begin{pmatrix} 1 - \frac{\lambda^2}{2} & \lambda & A\lambda^3(\rho - i\eta) \\ -\lambda & 1 - \frac{\lambda^2}{2} & A\lambda^2 \\ A\lambda^3(1 - \rho - i\eta) & -A\lambda^2 & 1 \end{pmatrix} + \mathcal{O}(\lambda^4) \quad (2.23)$$

where

$$s_{12} = \lambda = \frac{|V_{us}|}{\sqrt{|V_{ud}|^2 + |V_{us}|^2}} \quad (2.24)$$

$$s_{23} = A\lambda^2 = \lambda \left| \frac{V_{cb}}{V_{us}} \right| \quad (2.25)$$

$$s_{13}e^{i\delta} = V_{ub}^* = A\lambda^3(\rho + i\eta) = \frac{A\lambda^3(\bar{\rho} + i\bar{\eta})\sqrt{1 - A^2\lambda^4}}{\sqrt{1 - \lambda^2}\left[1 - A^2\lambda^4(\bar{\rho} + i\bar{\eta})\right]}. \quad (2.26)$$

The weak interaction coupling strength at weak interaction vertices is given by the matrix elements V_{ij} of the CKM matrix multiplied with $g_W/\sqrt{2}$ [9]. Therefore, the vertices of charged-current weak interactions of quarks can be written as [40]

$$-i\frac{g_W}{\sqrt{2}}\begin{pmatrix} \bar{u} & \bar{c} & \bar{t} \end{pmatrix}\gamma^\mu\frac{1}{2}\left(1 - \gamma^5\right)\begin{pmatrix} V_{ud} & V_{us} & V_{ub} \\ V_{cd} & V_{cs} & V_{cb} \\ V_{td} & V_{ts} & V_{tb} \end{pmatrix}\begin{pmatrix} d \\ s \\ b \end{pmatrix}. \quad (2.27)$$

In order to experimentally determine the values of the entries of the CKM matrix, branching ratios of decays involving a charged-current weak interaction are measured. Table 2.1 lists examples for decays and one scattering which can be used to determine the CKM matrix elements. In addition to the methods listed in table 2.1, it is also common to calculate $|V_{tb}|$ using the unitarity relations of the CKM matrix [40, 9].

The unitarity of the CKM matrix $V_{\text{CKM}}^\dagger V_{\text{CKM}} = \mathbb{1}$ yields three non-zero combinations of the diagonal elements

$$|V_{ud}|^2 + |V_{cd}|^2 + |V_{td}|^2 = 1 \quad (2.28)$$
$$|V_{us}|^2 + |V_{cs}|^2 + |V_{ts}|^2 = 1 \quad (2.29)$$
$$|V_{ub}|^2 + |V_{cb}|^2 + |V_{tb}|^2 = 1 \quad (2.30)$$

and six off-diagonal combinations which sum up to zero, for example

$$V_{ud}V_{ub}^* + V_{cd}V_{cb}^* + V_{td}V_{tb}^* = 0. \tag{2.31}$$

Since the products of $V_{ij}V_{ik}^*$ are themselves complex numbers, they can be represented as points in the two dimensional complex plane. Vectors connecting those points will have a length of $|V_{ij}V_{ik}^*|$ and will add up to zero as they form a closed triangle, called unitarity triangle. Using equation 2.31 and by dividing all side lengths of this triangle by $|V_{cd}V_{cb}^*|$, the unitarity triangle shown in figure 2.5 can be constructed [44].
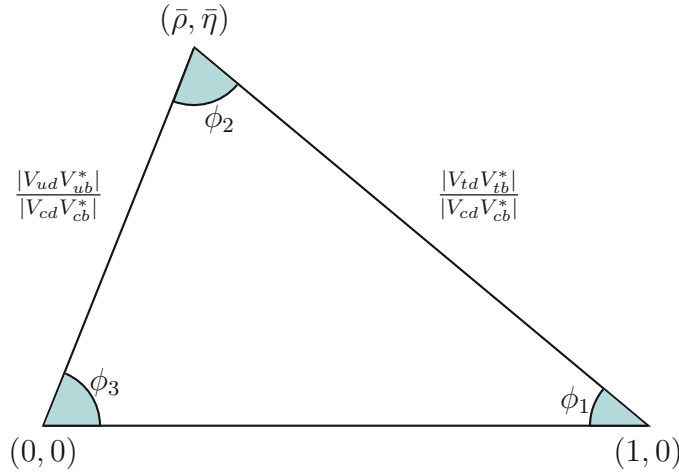
Figure 2.5: The unitarity triangle corresponding to equation 2.31.

$|V_{ij}|$	Observation
$|V_{ud}|$	β-decay
$|V_{us}|$	$K^0 \to \pi^- e^+ \nu_e$
$|V_{ub}|$	$B \to \pi^- e^+ \nu_e$
$|V_{cs}|$	$D_s^+ \to \mu^+ \nu_\mu$
$|V_{cb}|$	$B^0 \to D^- e^+ \nu_e$
$|V_{cd}|$	$\nu_\mu d \to \mu^- c$
$|V_{td}|$	$B^0 \leftrightarrow \bar{B}^0$ oscillations
$|V_{ts}|$	$B^0 \leftrightarrow \bar{B}^0$ oscillations
$|V_{tb}|$	t-quark production cross sections

Table 2.1: Examples for possible measurements of $|V_{ij}|$ [9, 40, 44].

The current values published by the particle data group for the CKM matrix are [44]

$$V_{\text{CKM}} = \begin{pmatrix} 0.97401 \pm 0.00011 & 0.22650 \pm 0.00048 & 0.00361^{+0.00011}_{-0.00009} \\ 0.22636 \pm 0.00048 & 0.97320 \pm 0.00011 & 0.04053^{+0.00083}_{-0.00061} \\ 0.00854^{+0.00023}_{-0.00016} & 0.03978^{+0.00082}_{-0.00060} & 0.999172^{+0.000024}_{-0.000035} \end{pmatrix}. \tag{2.32}$$

2.3 B meson production

Through a e^+e^- collision in a particle accelerator with the right particle energies, the $\Upsilon(4S)$ resonance of an Υ meson, which itself is made up of a bottom

and anti-bottom quark, can be produced. The $\Upsilon(4S)$ resonance is an excited state of the Υ meson and of utmost importance for B meson physics, since it subsequently decays into a $B\bar{B}$ meson pair with a branching ratio of $> 96\%$. It is the lowest Υ resonance with enough mass (about 10.58 GeV) to decay into a $B\bar{B}$ pair, with a mass of around 5.29 GeV each. B-mesons consist of a (anti-)bottom quark and depending on their charge either an (anti-)up or a (anti-)down quark [44]. Table 2.2 shows different common types of B mesons.

Type	Constituents	Mass [MeV]	Charge [e]
B^+	$u\bar{b}$	5279.34 ± 0.12	$+1$
B^-	$\bar{u}b$		-1
B^0	$d\bar{b}$	5279.65 ± 0.12	0
$\bar{B}^0$	$\bar{d}b$		0

Table 2.2: Different types of B mesons [44].
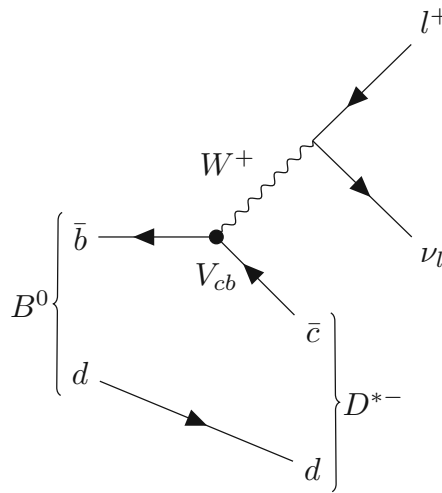
Figure 2.6: Feynman diagram of the $B^0 \to D^{*-}l^+\nu_l$ decay.

2.4   Why semi-leptonic decays?

As mentioned in the introduction, this thesis is motivated by an analysis done on semi-leptonic decays of B mesons. However, $B^0 \to D^{*-}l^+\nu_l$ decays only have a branching ratio of about 5% and there are decays with bigger branching ratios which would result in more usable data and consequently better statistics. The reasons for choosing semi-leptonic decays over hadronic or fully-leptonic decays will now be discussed.

On one hand, some hadronic decays would provide higher branching ratios and would therefore be better suited from an experimental point of view, but the theoretical description for these decays is way more complex than for leptonic decays. On the other hand, fully-leptonic decays would be easier to calculate theoretically, but because of their small branching ratios the data yield would be too low in order to be experimentally feasible. Therefore, under these conditions, semi-leptonic decays provide a decent middle ground considering theoretical and experimental limitations.

2.5 $|V_{cb}|$ extraction from $B^0 \to D^{*-}l^+\nu_l$ decays

In this section, the calculation of the CKM matrix element $|V_{cb}|$ from experimental measurements of $B^0 \to D^{*-}l^+\nu_l$ decays (where the charge-conjugated case is always implicitly included) will be described following [24].

As shown in previous sections, the weak charged current vertices of weak interactions in which a quark changes its flavor include the CKM matrix element V_{ij} corresponding with a quark flavor change from i to j. Therefore, as depicted in figure 2.6, the matrix element M of $B^0 \to D^{*-}l^+\nu_l$ decays is proportional to V_{cb} and since the decay rate $\Gamma \propto |M|^2$, it follows that $\Gamma(B^0 \to D^{*-}l^+\nu_l) \propto |V_{cb}|^2$. This relation is used to determine $|V_{cb}|$ from the experimentally measured decay rates.

In [24] the kinematics of the B^0 decay are parameterized by four parameters. The first one

$$w = \frac{p_B \cdot p_{D^*}}{m_B m_{D^*}} = \frac{m_B^2 + m_{D^*}^2 - q^2}{2m_B m_{D^*}}, \tag{2.33}$$

with $q^2 = (p_l + p_\nu)^2$. And three angles, which are depicted in figure 2.7:

- θ_l: The angle between the direction of the lepton and the opposite direction of the B meson in the W rest frame.

- θ_V: The angle between the direction of the D meson and the opposite direction of the B meson in the D^* rest frame.

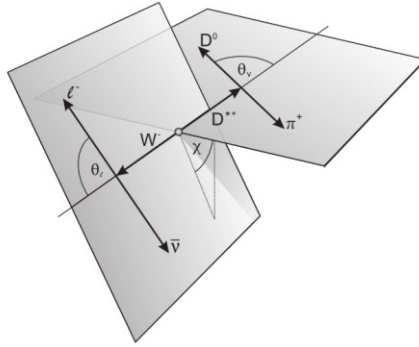- χ: The angle between the two surfaces, which the decay products of the D^* and W decays span.

Figure 2.7: The three angles used in the parametrization of the decay kinematics [24].

The differential decay rate for $B^0 \to D^{*-}l^+\nu_l$ can be written as [24]

$$\frac{\mathrm{d}^4\Gamma\left(B^0 \to D^{*-}l^+\nu_l\right)}{\mathrm{d}w\,\mathrm{d}(\cos\theta_l)\,\mathrm{d}(\cos\theta_V)\,\mathrm{d}\chi} = \frac{6m_B m_{D^*}^2}{8(4\pi)^4}\sqrt{w^2-1}\left(1-2wr+r^2\right)G_F^2|V_{cb}|^2$$
$$\times \left\{(1-\cos\theta_l)^2\sin^2\theta_V H_+^2(w)\right.$$
$$+ (1+\cos\theta_l)^2\sin^2\theta_V H_-^2(w)$$
$$+ 4\sin^2\theta_l\cos^2\theta_V H_0^2(w)$$
$$- 2\sin^2\theta_l\sin^2\theta_V\cos(2\chi)H_+(w)H_-(w)$$
$$- 4\sin\theta_l(1-\cos\theta_l)\sin\theta_V\cos\theta_V\cos\chi H_+(w)H_0(w)$$
$$\left.+ 4\sin\theta_l(1+\cos\theta_l)\sin\theta_V\cos\theta_V\cos\chi H_-(w)H_0(w)\right\}, \tag{2.34}$$

where the neutrino masses are neglected and three helicity amplitudes H_-, H_0 and H_+ for the D^* polarization states are taken into account. The helicity states can be described by the functions $h_{A_1}(w)$, $R_1(w)$ and $R_2(w)$, which themselves can be parameterized using heavy quark effective theory, by

$$H_{\pm,0} = m_B \frac{R^*(1-r^2)(w+1)}{2\sqrt{1-2wr+r^2}} h_{A_1}(w) \tilde{H}_{\pm,0}(w) \tag{2.35}$$

with

$$\tilde{H}_{\mp} = \frac{\sqrt{1-2wr+r^2} \left(1 \pm \sqrt{\frac{w-1}{w+1}} R_1(w)\right)}{1-r}, \tag{2.36}$$

$$\tilde{H}_0 = 1 + \frac{(w-1)(1-R_2(w))}{1-r}, \tag{2.37}$$

$$R^* = \frac{2\sqrt{m_B m_{D^*}}}{m_B + m_{D^*}}, \tag{2.38}$$

$$r = \frac{m_{D^*}}{m_B} \tag{2.39}$$

and

$$h_{A_1}(w) = \frac{1}{R^*} \frac{2}{w+1} A_1(w), \tag{2.40}$$

where $A_1(w)$ is an axial form factor [24].

By integrating equation 2.34 over $d(\cos\theta_l)$, $d(\cos\theta_V)$ and $d\chi$, the differential decay rate with respect to w can be calculated to be [24]

$$\frac{d\Gamma}{dw} = \frac{G_F^2}{48\pi^3} m_{D^*}^3 (m_B - m_{D^*})^2 \mathcal{G}(w) \mathcal{F}^2(w) |V_{cb}|^2 \tag{2.41}$$

where $\mathcal{G}(w)$ is the phase space factor

$$\mathcal{G}(w) = \sqrt{w^2-1}(w+1)^2 \left[1 + 4\frac{w}{w+1}\frac{1-2wr+r^2}{(1-r)^2}\right], \tag{2.42}$$

and

$$\mathcal{G}(w)\mathcal{F}^2(w) = h_{A_1}^2(w)\sqrt{w^2-1}(w+1)^2 \left\{2\left[\frac{1-2wr+r^2}{(1-r)^2}\right]^2 \right.$$
$$\left. \times \left[1 + R_1^2(w)\frac{w^2-1}{w+1}\right] + \left[1 + (1-R_2(w))\frac{w-1}{1-r}\right]^2\right\}. \tag{2.43}$$

In the paper [24], a parametrization similar to the one developed in [17] is used in order to express $h_{A_1}(w)$, $R_1(w)$ and $R_2(w)$ in powers of $(w-1)$ as

$$h_{A_1}(w) = h_{A_1}(1)\left[1 - 8\rho^2 z + \left(53\rho^2 - 15\right)z^2 - \left(231\rho^2 - 91\right)z^3\right], \tag{2.44}$$

$$R_1(w) = R_1(1) - 0.12(w-1) + 0.05(w-1)^2 \tag{2.45}$$

and

$$R_2(w) = R_2(1) + 0.11(w-1) - 0.06(w-1)^2 \tag{2.46}$$

with

$$z = \frac{\sqrt{w+1}-\sqrt{2}}{\sqrt{w+1}+\sqrt{2}}. \tag{2.47}$$

The three newly introduced parameters ρ^2, $R_1(1)$ and $R_2(1)$ can be calculated from binned least χ^2 fits to the experimentally obtained distributions of the four kinematic variables discussed before (w, $\cos\theta_l$, $\cos\theta_V$ and χ) with the fit parameters $\mathcal{F}(1)|V_{cb}|$, ρ^2, $R_1(1)$ and $R_2(1)$ [24]. With this method using 711fb^{-1} of data from the Belle experiment the following values

$$\mathcal{F}(1)|V_{cb}| = (34.6 \pm 0.2 \pm 1.0) \cdot 10^{-3} \tag{2.48}$$
$$\rho^2 = 1.214 \pm 0.034 \pm 0.009 \tag{2.49}$$
$$R_1(1) = 1.401 \pm 0.034 \pm 0.018 \tag{2.50}$$
$$R_2(1) = 0.864 \pm 0.024 \pm 0.008 \tag{2.51}$$

could be extracted in 2010 by W. Dungel et al. as described in [24]. Since $\mathcal{F}(1)$ can be calculated using lattice QCD methods, $|V_{cb}|$ can therefore be obtained by knowing the four kinematic variables w, $\cos\theta_l$, $\cos\theta_V$ and χ mentioned above, and the branching ratio $\mathcal{B}(B^0 \to D^{*-}l^+\nu_l)$. It is thereby a direct consequence, that a more precise knowledge of the reconstructed $B^0 \to D^{*-}l^+\nu_l$ decays also allows for greater precision for the calculation of $|V_{cb}|$. However, currently the slow pion efficiency at Belle II acts as a limiting factor for the precision of the reconstruction of $B^0 \to D^{*-}l^+\nu_l$ decays [21], which is the main motivation for this thesis and will be discussed in greater detail below.

2.6   The slow pion efficiency problem

As mentioned before, being able to precisely reconstruct $B^0 \to D^{*-}l^+\nu_l$ decays is necessary in order to calculate the CKM matrix element $|V_{cb}|$ from experimental measurements. Because of the small mass difference of D^* and D^0 mesons of $m_{D^{*+}} - m_{D^0} = 145.4258 \pm 0.0017$ [MeV] [44], the $D^{*-} \to \bar{D}^0\pi_s^-$ decay involves a pion with a momentum in the low hundreds of MeV range (as shown in figure 2.8), which is called slow or soft pion. In order to reconstruct $D^{*-} \to \bar{D}^0\pi_s^-$ decays, a precise detection of slow pions is necessary. However, as described in [21], currently the uncertainty of the reconstruction efficiency of slow pions is rather large and is therefore dominating the error for the $B^0 \to D^{*-}l^+\nu_l$ branching ratio. The current tracking efficiency uncertainty of slow pions is about 9.9% and affects the $\bar{B}^0 \to D^{*+}l^-\bar{\nu}_l$ branching ratio as [21]

$$\mathcal{B}\left(\bar{B}^0 \to D^{*+}l^-\bar{\nu}_l\right) = (4.60 \pm 0.05_{\text{stat}} \pm 0.17_{\text{syst}} \pm 0.45_{\pi_s})\,\%. \tag{2.52}$$

Gaining a better understanding of and lowering the uncertainty of the slow pion tracking efficiency is the main goal of this thesis.
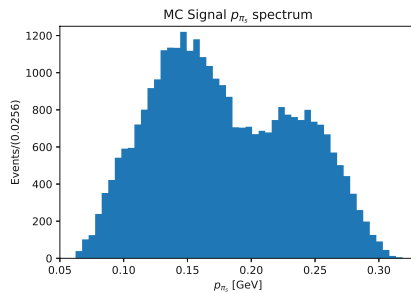

Figure 2.8: p_{π_s} spectrum from $D^{*-} \to \bar{D}^0\,\pi_s^-$ decays.

Chapter 3

Experimental overview

In experimental particle physics, a lot of information is gathered by scattering and colliding particles at high energies. This section will provide a brief overview about particle accelerators and some commonly used components for particle detection. At first, the underlying principles will be explained and later on, their implementation in Belle II will be described.

3.1 Particle accelerators

In order to collide particles at high energies, they have to be accelerated first. There are two different principles of particle accelerators which are commonly used in modern particle physics: linear accelerators and synchrotrons. A short introduction to those types of accelerators will be given below.

3.1.1 Luminosity

When characterizing particle accelerators, the two most relevant properties are the center-of-mass energy $\sqrt{s}$ and the luminosity. The first one acts as an upper-bound for the energy and therefore mass of created particles. The latter describes the rate of collision events per area and time interval and is usually given in units of $\mathrm{cm}^{-2}\mathrm{s}^{-1}$.

Under a few simplifying assumptions, the peak luminosity can be written as

$$\mathcal{L} = f \frac{n_1 n_2}{4\pi \sigma_x \sigma_y}, \tag{3.1}$$

where f is the frequency of collisions, n_1 and n_2 are the number of particles per bunch and σ_x and σ_y are the root-mean-square transverse beam sizes. A particle bunch describes multiple particles that move in close proximity to each other in the beam pipe, due to the acceleration in the RF cavities [6]. Integrating the above equation over the operational lifetime of an accelerator yields the integrated luminosity, which multiplied with the cross section σ results in the number of interactions [40]

$$N = \sigma \int \mathcal{L}(t) \mathrm{d}t. \tag{3.2}$$

3.1.2 Linear accelerator

A particle with charge q and velocity $\vec{v}$ in an electromagnetic field will be accelerated as described by the Lorentz force [25]

$$\vec{F} = q\left(\vec{E} + \vec{v} \times \vec{B}\right). \tag{3.3}$$

Without a magnetic field it follows that [23]

$$W = \int_{P_1}^{P_2} \vec{F} \cdot d\vec{s} = q \int_{P_1}^{P_2} \vec{E} \cdot d\vec{s} = qU, \tag{3.4}$$

with

$$U = \int_{P_1}^{P_2} \vec{E} \cdot d\vec{s}. \tag{3.5}$$

Therefore, the kinetic energy of a charged particle in a capacitor with the voltage U changes by

$$\Delta E_{kin} = qU. \tag{3.6}$$

This basic principle has been utilized since the 1930s to reach energies of up to a few MeV [9]. In order to achieve higher energies, multiple separate regions with a smaller voltage are used as shown in figure 3.1. An alternating voltage is applied to the cylinders C1 to C4. At first, the phase of the voltage will be chosen to accelerate the particle from the source S to C1. Thereby, the particle will gain the energy

$$\Delta E = qU \sin\bar{\phi}, \tag{3.7}$$

where $\bar{\phi}$ is the average phase during the passage. While passing through C1, the phase will have changed so that every tube is now differently charged. This results in an acceleration to the succeeding tube and the same process is repeated. Since the particle gains energy in each gap, the length of the tubes has to be adjusted accordingly to

$$l_i = \frac{v_i}{2f}, \tag{3.8}$$

in order to use a constant voltage frequency [9].
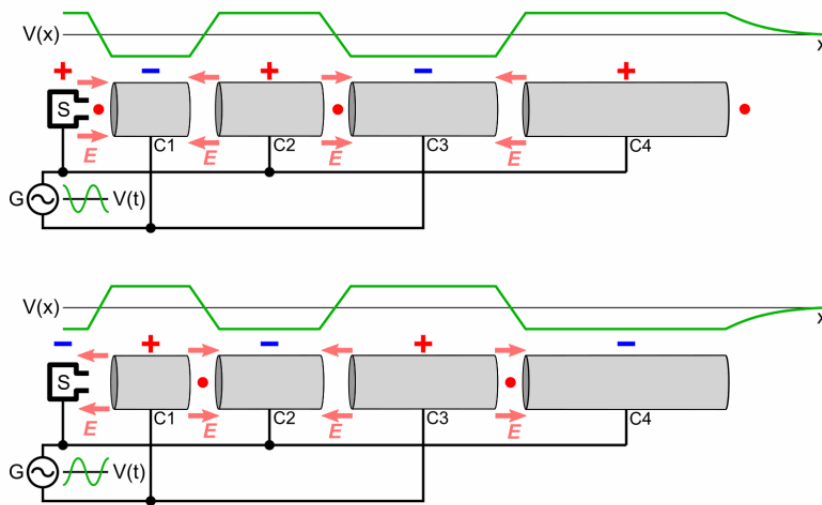
Figure 3.1: Linear accelerator with drift tubes. The two pictures show the different charge configurations due to the alternating voltage [20].

To achieve higher energies, electromagnetic waves in cavity resonators are used. The charged particles in the waveguides are accelerated by the changing electric field due to the propagating electromagnetic waves. For example, the TM_{01} resonance has transversal magnetic field components and only a longitudinal electric field component, which travels in the same direction as the charged particle and accelerates it [9].

3.1.3 Synchrotron

In contrast to linear accelerators, synchrotrons are constructed in a circular shape. They consist of a vacuum chamber, which the particles pass through, a set of magnets, which are used to force the particles onto a closed circular path and to focus the beam, and a linear accelerator. With each revolution inside the synchrotron, the particle gets accelerated further. Since faster particles require a larger magnetic field in order to keep them on a path with constant radius, the magnetic field has to be raised accordingly during the acceleration. Once the desired energy is reached, a synchrotron can be used as a storage ring, where the particle's energy is held constant by only supplying enough energy to the accelerator to compensate for energy losses, for example synchrotron radiation [9].

Due to the synchrotron being a closed circular path, the particles have to be accelerated by a linear accelerator beforehand and subsequently injected into the synchrotron. Currently, the highest collision energies are achieved by LHC at CERN with energies of up to 13 TeV for proton-proton collisions [19].

3.2 Particle detectors

In order to reconstruct particle decays, the knowledge of the momentum, mass, energy and charge of particles is of great interest. Depending on their properties, particles interact differently with matter and therefore modern particle physics experiments utilize a combination of various types of detectors. A typical detector layout at a collider experiment is schematically depicted in figure 3.2, where ECAL stands for electromagnetic calorimeter and HCAL for hadronic calorimeter. The working principles of the shown detectors will be explained below.
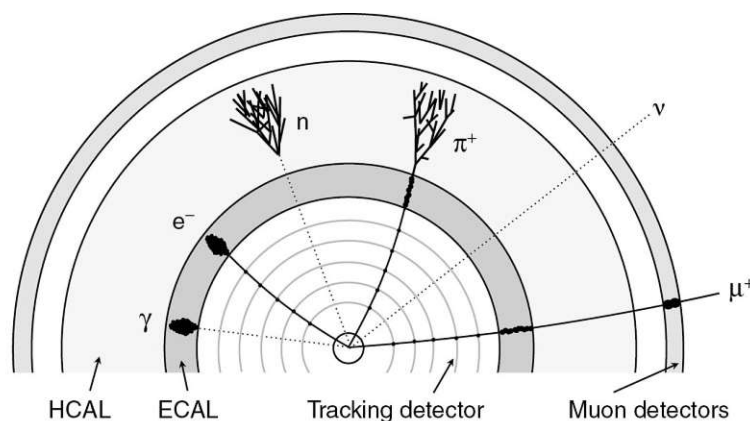

Figure 3.2: Schematic detector layout surrounding the interaction point [40].

3.2.1 Bethe-Bloch equation

While passing through matter, charged relativistic particles ionize the matter's atoms by electromagnetic interactions and the particles decrease their energy in the process. This energy loss due to ionization for a charged particle is approximately described by the Bethe-Bloch equation

$$\frac{\mathrm{d}E}{\mathrm{d}x} \approx -4\pi\hbar^2 c^2\alpha^2\frac{nZ}{m_e v^2}\left\{\ln\left[\frac{2\beta^2\gamma^2 c^2 m_e}{I_e}\right]-\beta^2\right\}, \qquad (3.9)$$

where n is the density, Z the atomic number and I_e the effective ionization potential, which is specific to the traversed matter and can be approximated by

$$I_e \approx 10Z \text{ [eV]}. \qquad (3.10)$$

The Bethe-Bloch equation can also be written as

$$\frac{1}{\rho}\frac{\mathrm{d}E}{\mathrm{d}x} \approx -\frac{4\pi\hbar^2 c^2\alpha^2}{m_e v^2 m_u}\frac{Z}{A}\left\{\ln\left[\frac{2\beta^2\gamma^2 m_e c^2}{I_e}\right]-\beta^2\right\}, \qquad (3.11)$$

with $m_u = 1.66 \cdot 10^{-27}$ kg. Since $Z/A \approx$ const., the general form of the Bethe-Bloch equation is only weakly influenced by the specific matter other than through its density ρ [40]. This behavior is depicted in figure 3.3.
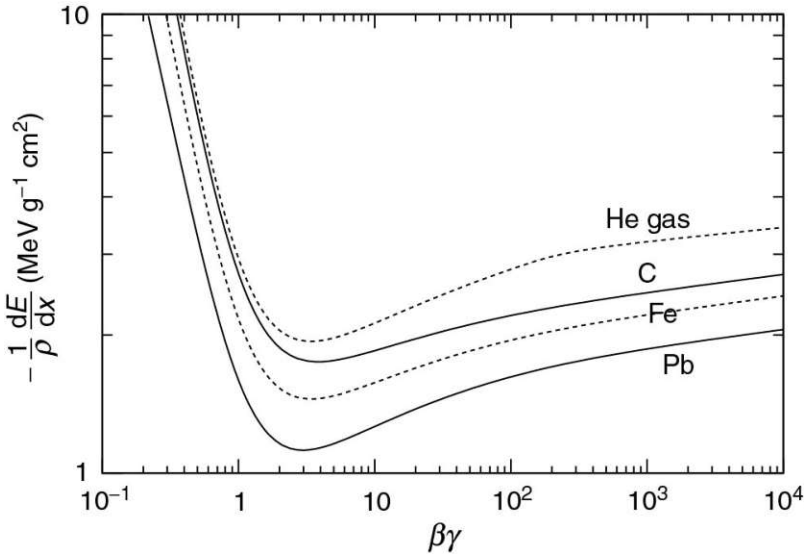
Figure 3.3: Plot of the Bethe-Bloch equation for different target materials [40].

3.2.2 Particle tracking detectors

As mentioned in the previous section, charged particles traversing matter will ionize the atoms in it. This trace of ionized atoms can be used to reconstruct the trajectory of the charged particle which moved through the medium. There are two commonly used methods to track the ionization: drift chambers and semiconducting silicon wafers [40].

Due to an applied magnetic field in the direction of the colliding particle beams (z-axis in this case), the charged particle will move along the path of a helix, which is shown in figure 3.6. From the Lorentz force of a magnetic field $\vec{F}_L \propto \vec{v} \times \vec{B}$ on a particle with charge $|q| = e$ follows

$$p\cos\lambda = 0.3BR, \qquad (3.12)$$

where p is in GeV/c, B in Tesla and R in meters. Therefore, by tracking the path of a charged particle and determining R and λ, its momentum can be calculated [40].

Drift chambers

The functionality of drift chambers is based on the working principle of proportional counters. In its most basic form, a proportional counter consists of a gas-filled cylinder with a wire passing through it. A particle traversing the chamber with sufficient energy will ionize the gas. The resulting electrons and ions are accelerated towards the wall of the cylinder and the wire depending on their charge, if a voltage is applied between the wall (cathode) and the wire (anode). This current results in a voltage drop, which can be measured to gain information about the incident particle [9].

The integration of multiple wires into a single chamber enables the positional determination of the passing particle by individually measuring the voltage for every wire. Such a device is called multi-wire proportional chamber and its schematic construction is shown in figure 3.4. An additional increase of the spatial resolution can be achieved by measuring the time delay between the particle passing the chamber and the detection of the signal. With the knowledge of the drift velocity of the electrons and this time interval, the distance at which the incident particle passed by the wire can be calculated. This configuration is then called drift chamber [9].
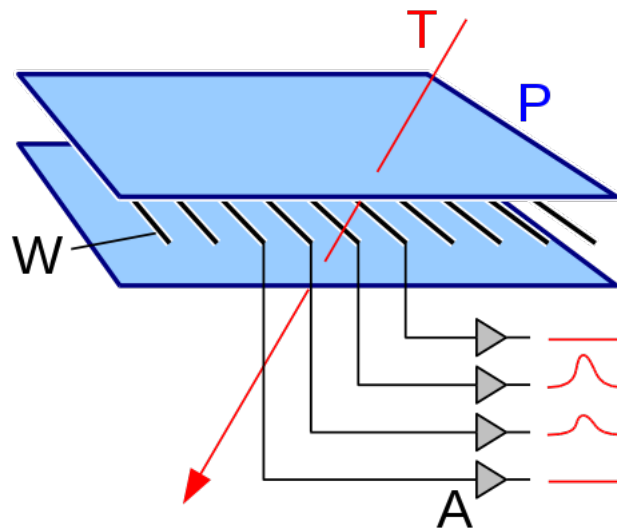
Figure 3.4: Schematic depiction of a multi-wire chamber [37].

Silicon detectors

By arranging n-type and p-type silicon p-n junctions in strips as shown in figure 3.5, the path of a charged particle can be tracked. While traversing the doped silicon, a charged particle will create electron-hole-pairs which will be accelerated by the electric field created by the applied voltage in the direction of the p-n junctions. The resulting signals correspond to the position at which the particle passed through the silicon wafer. When these silicon detectors

are arranged in multiple concentric cylinders around the interaction point, a charged particle traversing will hit each layer at a different position.
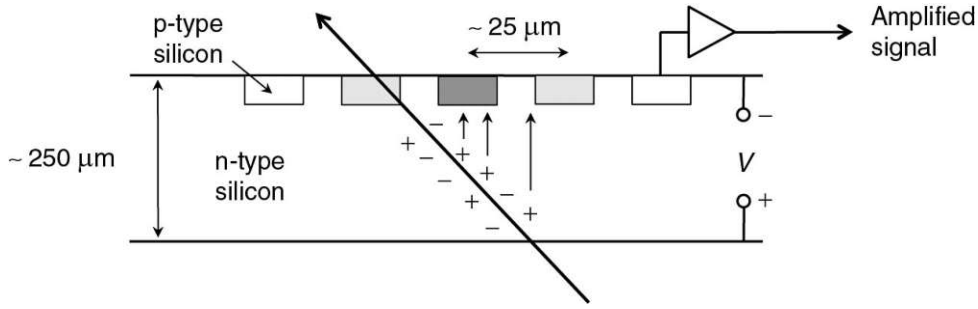

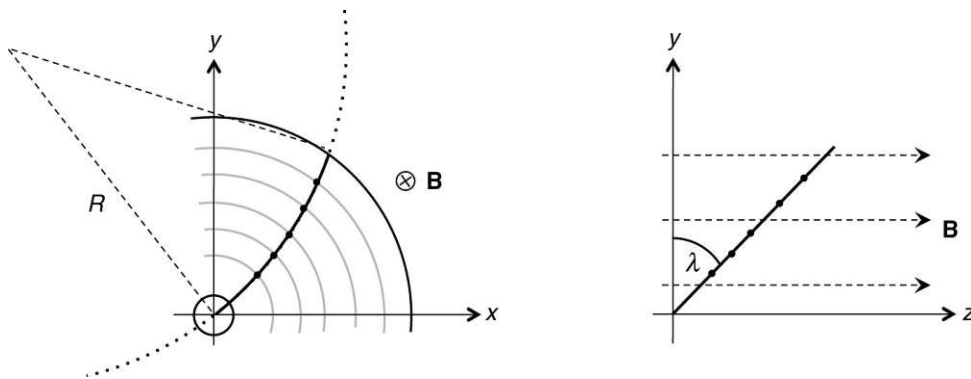Figure 3.5: A silicon semi-conducting p-n junction [40].

Figure 3.6: Tracking a particle's path with multiple cylindrical layers of silicon detectors [40].

3.2.3 Electromagnetic and hadronic calorimeters

There are different mechanism by which electrons and photons loose energy while traversing matter. For electrons, ionization is most common at lower energies and at energies above a medium specific critical energy

$$E_c \sim \frac{800}{Z}\text{MeV}, \tag{3.13}$$

where Z is the atomic number, losses due to bremsstrahlung are predominant. For photons, low energy interactions are typically via the photoelectric effect, mid-range energies lead to Compton scattering and for high energies the e^+e^- pair production in the presence of a nucleus dominates [40].

In addition to the critical energy E_c, the radiation length X_0 is another important value to characterize electromagnetic showers. It is defined as the mean length in which the energy of the electron decreases to $E' = E/e$ and can be approximated by

$$X_0 \approx \frac{1}{4\alpha n Z^2 r_e^2 \ln\left(287/Z^{1/2}\right)}. \tag{3.14}$$

For example, the radiation length for lead is $X_0(Pb) = 0.56$ cm and for iron $X_0(Fe) = 1.76$ cm [40, 9].

An accelerated charge emits radiation proportional to its acceleration. This can be explained by applying the Liénard-Wiechert potentials

$$\phi(t,\vec{r}) = \frac{q}{R(t') - \vec{\beta}(t') \cdot \vec{R}(t')}\bigg|_{t'=t-\frac{R(t')}{c}} \tag{3.15}$$

$$\vec{A}(t,\vec{r}) = \frac{q\vec{\beta}(t')}{R(t') - \vec{\beta}(t') \cdot \vec{R}(t')}\bigg|_{t'=t-\frac{R(t')}{c}} \tag{3.16}$$

to the relations

$$\vec{E} = -\vec{\nabla}\phi - \frac{1}{c}\frac{\partial \vec{A}}{\partial t} \tag{3.17}$$

$$\vec{B} = \vec{\nabla} \times \vec{A}. \tag{3.18}$$

One intermediate result of the calculation is

$$\frac{1}{c}\frac{\partial \vec{A}}{\partial t} = \frac{q\dot{\vec{\beta}}}{Rc\left(1 - \vec{\beta} \cdot \vec{e}_R\right)^2} + \frac{q\vec{\beta}\left(\vec{e}_R \cdot \vec{\beta} + \frac{1}{c}\dot{\vec{\beta}} \cdot \vec{R} - \beta^2\right)}{R^2\left(1 - \vec{\beta} \cdot \vec{e}_R\right)^3}, \tag{3.19}$$

which shows that first, there are terms with $\propto 1/R^2$ that describe a field which arises independent of an acceleration. And secondly, that there are terms with $\propto \dot{\vec{\beta}}/(Rc)$ that are proportional to the charge's acceleration. This leads to

$$\vec{E} = \frac{q}{Rc\left(1 - \vec{\beta} \cdot \vec{e}_R\right)^3}\left(\vec{e}_R \times \left[\left(\vec{e}_R - \vec{\beta}\right) \times \dot{\vec{\beta}}\right]\right) \tag{3.20}$$

$$\vec{B} = \vec{e}_R \times \vec{E}, \tag{3.21}$$

for $R \gg c/\dot{\beta}$. This emission of photons from accelerated charged particles, or charges in general, is the reason for phenomena as bremsstrahlung, which is radiated, when a charged particle interacts with the electromagnetic field of a nucleus, and synchrotron radiation, that is emitted if a charged particle is forced on a given path by magnetic fields [8, 9].
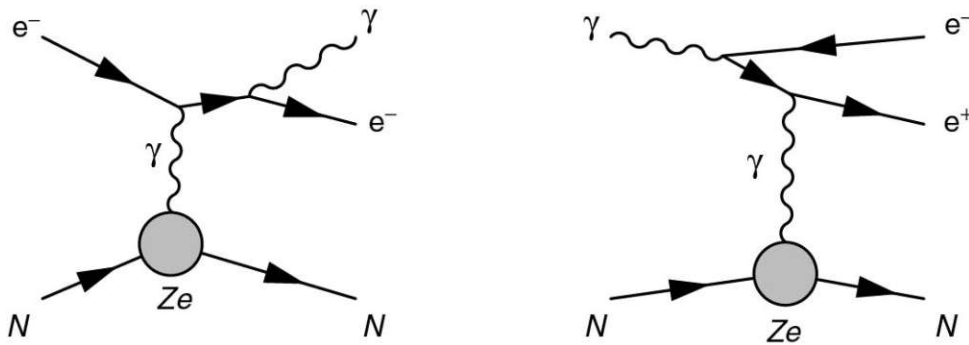
Figure 3.7: Bremsstrahlung (left) and e^+e^- pair-production (right) [40].

In the case of electrons with high energy, the afore-mentioned bremsstrahlung radiated while passing through a medium, the photon has enough energy for e^+e^- pair production. Feynman diagrams showing the processes

of bremsstrahlung and e^+e^- pair production are depicted in figure 3.7. The initial electron and both the electron and positron originating from e^+e^- pair production will subsequently electromagnetically interact with the medium and emit bremsstrahlung themselves. This leads to an cascade of electrons, photons and electron-positron-pairs, which is called electromagnetic shower. In each new generation of the cascade, which corresponds to one radiation length X_0 of passed through matter, the amount of charged particles is roughly doubled. Therefore, an initial electron with energy E generates an electromagnetic shower in which the average energy per particle is given by

$$\langle E \rangle \approx \frac{E}{2^n}, \tag{3.22}$$

where n is the number of radiation lengths. As soon as $\langle E \rangle < E_c$, the cascade stops since then the energy loss of the particles is dominated by ionization processes. An electromagnetic shower can also be started by a photon that produces a e^+e^- pair. The schematic behavior of an electromagnetic shower is depicted in figure 3.8. In order to reconstruct the initial energy of an electron or photon, this cascading behavior of electromagnetic showers can be used by measuring the amount of scintillation light that is created by the electrons while passing through the scintillating material of the electromagnetic calorimeter. The amount of measured light is thus proportional to the incident particle's energy [40, 9].

Interestingly, the energy resolution of electromagnetic calorimeters is limited by statistics. This can be derived from the simplified toy model used in the explanation above. Since the number of charged particles after n radiation lengths is approximately

$$N \approx 2^n, \tag{3.23}$$

the incident particle's energy E is

$$E = N \cdot E_c \tag{3.24}$$

and the process follows Poisson statistics, the energy resolution can be calculated from

$$\sigma(N) = \sqrt{N} \tag{3.25}$$

$$\sigma(E) = \sqrt{N} E_c \tag{3.26}$$

$$\frac{\sigma(E)}{E} = \frac{\sqrt{N} E_c}{E} = \sqrt{\frac{E}{E_c}} \cdot \frac{E_c}{E} \tag{3.27}$$

to be inversely proportional to the square root of the incident particle's energy as

$$\frac{\sigma(E)}{E} \propto \frac{1}{\sqrt{E}}. \tag{3.28}$$

Modern electromagnetic calorimeters can achieve an energy resolution of [40]

$$\frac{\sigma_E}{E} \sim \frac{3\% - 10\%}{\sqrt{E/\text{GeV}}}. \tag{3.29}$$
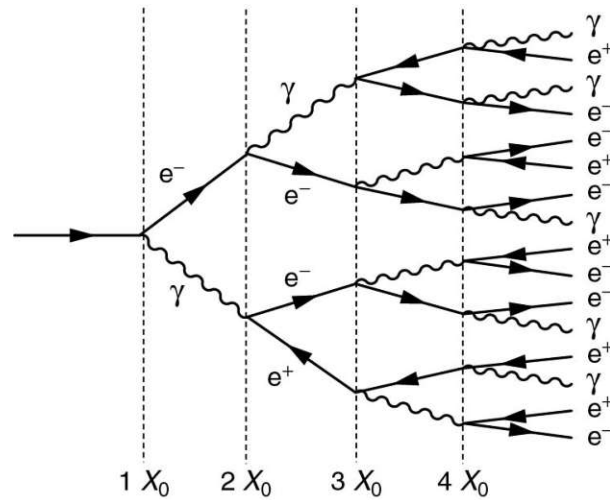
Figure 3.8: Schematic of an electromagnetic shower [40].

The same principle of measuring a particle's energy can be used for hadrons. However, the interaction length λ is much larger than X_0 for electrons and photons and therefore hadronic calorimeters have to be much larger in size. Furthermore, due to factors like $\pi^0 \to \gamma\gamma$ decays, whose photons themselves produce electromagnetic showers, and energy losses by emitted neutrons and K^0 mesons which are undetected by the calorimeter, the energy resolution of hadronic calorimeters is with [40]

$$\frac{\sigma_E}{E} \gtrsim \frac{50\%}{\sqrt{E/\text{GeV}}} \tag{3.30}$$

lower than the resolution of electromagnetic calorimeters [40, 9].

3.2.4   Cherenkov radiation

If a charged particle travels through a medium with a speed greater than the speed of light for the medium, it causes the radiation of photons on a cone with a specific opening angle θ_C. This is called Cherenkov radiation [8].

While passing through a dielectric medium, a charged particle polarizes the atoms of the medium by electromagnetic interactions, which will eventually relax back to their original unpolarized state by radiating photons. Since the speed of light in a dielectric medium is reduced by a factor of $1/n$ in comparison to the speed of light in vacuum, where n is the refractive index, particles can travel with speeds greater than the speed of light in the medium $\tilde{c} = c/n$ through the medium. In this case, the electromagnetic waves emitted from different atoms interfere constructively and result in a coherent wavefront, which is called Cherenkov radiation. If the particle's velocity is smaller than $\tilde{c}$, the interference of waves is destructive [40].
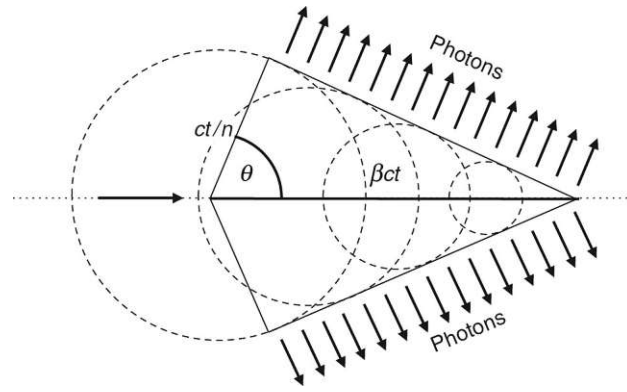
Figure 3.9: Geometric construction for Cherenkov radiation [40].

From the geometry depicted in figure 3.9 the relation

$$\cos\theta_C = \frac{1}{n\beta},\tag{3.31}$$

where $\beta = v/c$, can be deduced. By measuring the angular and spatial distribution of the emitted Cherenkov radiation, information about the charged particles passing through the medium can be gained. For example, only by particles with $\beta > 1/n$ and relativistic particles which satisfy

$$mc < \sqrt{(n^2 - 1)}p\tag{3.32}$$

Cherenkov radiation will be emitted [40].

3.3 SuperKEKB

SuperKEKB is an asymmetric e^+e^- synchrotron particle collider with a circumference of about 3 km and classifies as a B-factory, since the collisions provide a high B meson yield. By colliding electrons with an energy of 7 GeV and positrons with an energy of 4 GeV, $\Upsilon(4S)$ resonances are created, that subsequently decay to $B\bar{B}$ meson pairs as described in a previous chapter. The schematic layout of SuperKEKB is shown in figure 3.10. The basic building blocks are [2, 4]:

- **Electron ring:** The high energy ring for the 7 GeV electrons.

- **Positron ring:** The low energy ring for the 4 GeV positrons.

- **Belle II detector:** The particle detector surrounding the interaction region.

- **Electron-positron injector linac:** A linear accelerator that accelerates the electrons and positrons over a length of 600 meters from their source towards the electron and positron rings and injects them into the synchrotron. As sources for electron and positron production a photocathode RF gun, thermionic gun, flux concentrator and large-aperture accelerating structures are utilized.

- **Positron damping ring:** In order to reduce the emittance of the positron beam, positrons pass through a 1.1 GeV damping ring prior to their injection into the synchrotron. Since the positrons loose energy due to synchrotron radiation inside the damping ring, two 0.7 MV RF accelerating cavities compensate the energy loss. Overall, the particle's energy thus stays the same, but the phase-space distribution of the momentum changes and therefore the beam emittance is reduced. Emittance is a measure of how spread out the particles are in the phase space. It is defined as the area of an ellipse in phase space containing a certain percentage of particles, for example 95% [6].
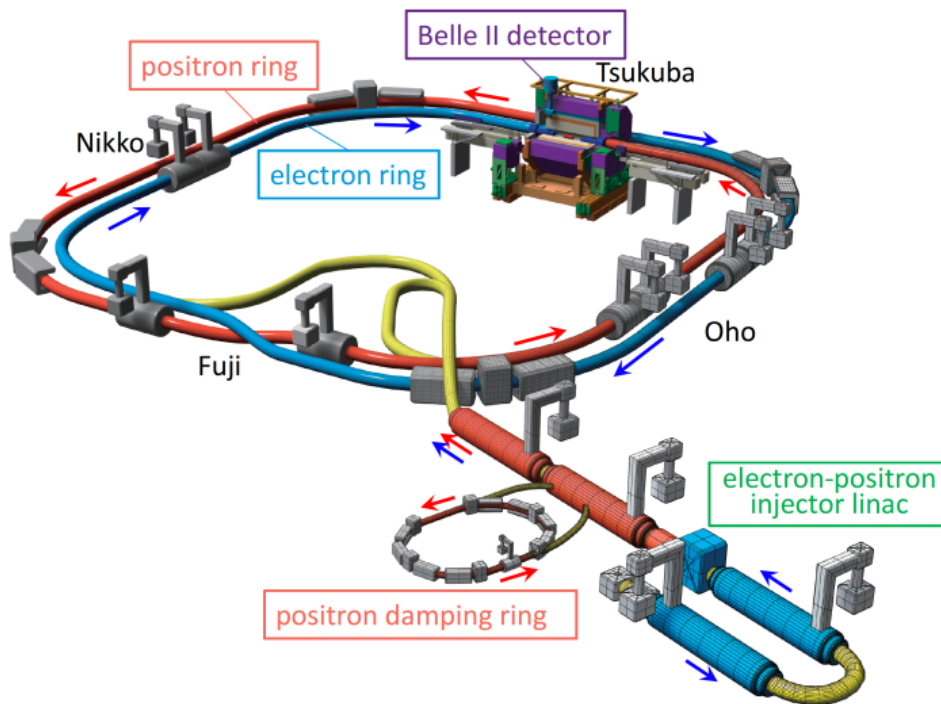
Figure 3.10: Layout of SuperKEKB [4].

SuperKEKB is designed for a peak luminosity of $8 \cdot 10^{35}$ cm^{-2}s^{-1}, which is about 40 times larger than KEKB's, and targets an integrated luminosity of 50 ab^{-1}. In comparison, KEKB accumulated an integrated luminosity of 1.041 ab^{-1}. In order to achieve this luminosity, SuperKEKB uses a nano-beam scheme, which reduces the beta function at the interaction point β_y^* of the electron and positron beams by lowering the size of longitudinal interaction regions of the beams [2, 4]. This nano-beam scheme is depicted in figure 3.11 and a roadmap for the planned luminosity in figure 3.12.
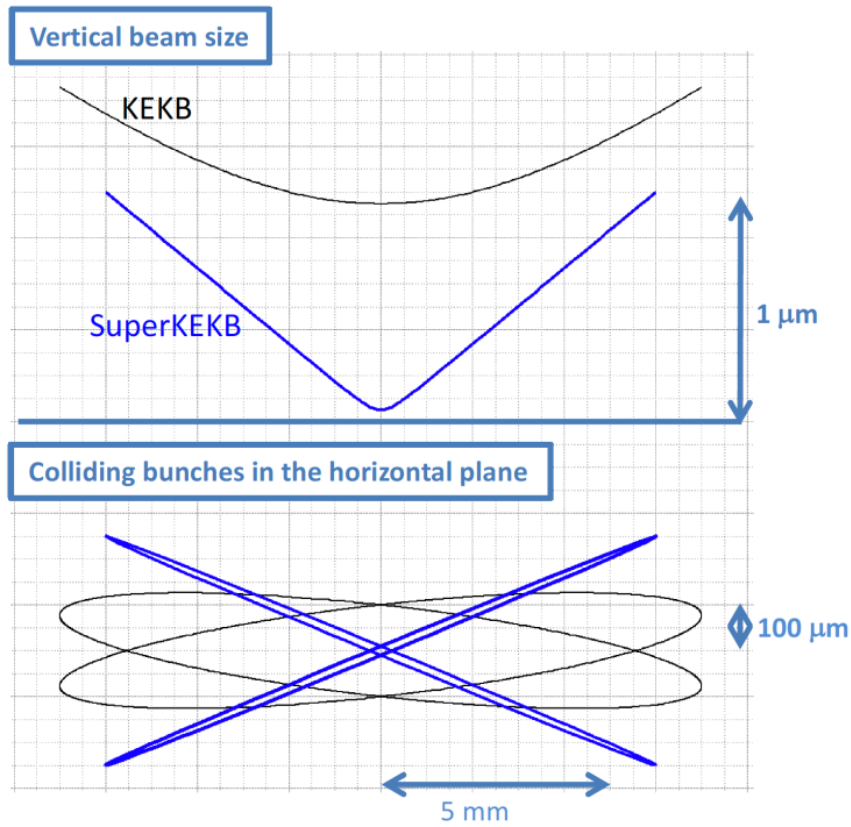
Figure 3.11: Illustration of the vertical beam size and the nano-beam scheme at SuperKEKB in comparison with its predecessor KEKB [4].
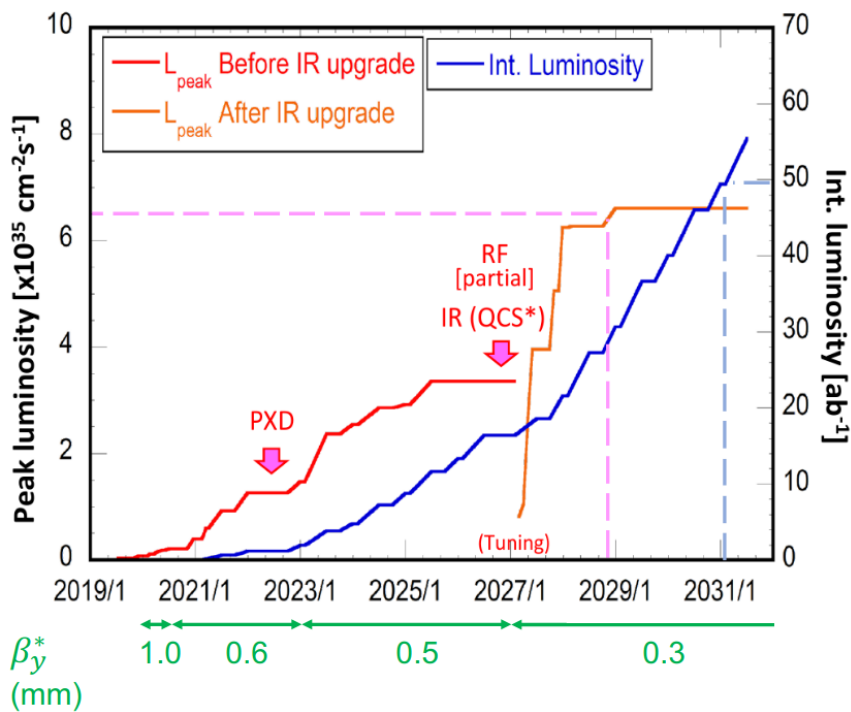
Figure 3.12: Roadmap for the luminosity of SuperKEKB [41].

3.4 Belle II

The Belle II particle detector is used in conjunction with the SuperKEKB particle accelerator, which are both operated by the Japanese High-Energy Accelerator Research Organisation (KEK), located in Tsukuba, Japan. Belle II and SuperKEKB are upgrades from their predecessors Belle and KEKB, that were in operation between 1998 and 2010 [2]. During this period, the experimental verification of the proposed Kobayashi-Maskawa theory "for the discovery of the origin of the broken symmetry which predicts the existence of at least three families of quarks in nature" [1] led to the Nobel prize in physics in the year 2008.

The Belle II detector consists of multiple sub-detector systems, that each serves a different purpose. The layout of Belle II is shown in figures 3.13 and 3.14. Depending on which sub-detectors register hits and their location, the measurements provided by the different systems can be combined to reconstruct the tracks of particles and gain information about their charge, mass, energy and momentum. From the interaction point outwards, they are:

- **Vertex Detector:** Detects the vertices of short-lived particles.

- **Central Drift Chamber:** Measures the tracks of charged particles and their momentum.

- **Particle Identification System:** Distinguishes between kaons, pions, muons and electrons.

- **Electromagnetic Calorimeter:** Measures the energy of charged particles and completely stops photons and electrons.

- K_L **and muon detector:** A hadronic calorimeter, that is used to distinguish between K_L mesons, muons and hadrons.
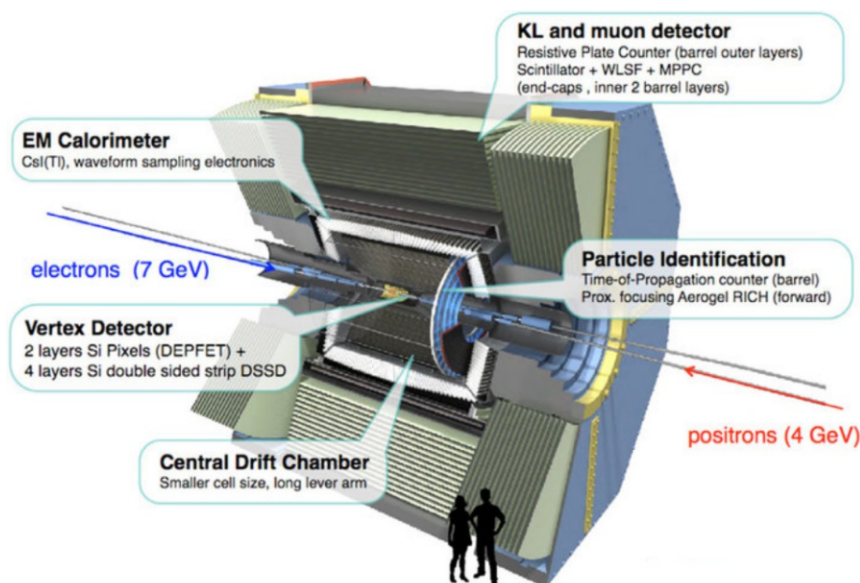
Figure 3.13: The Belle II detector [36].
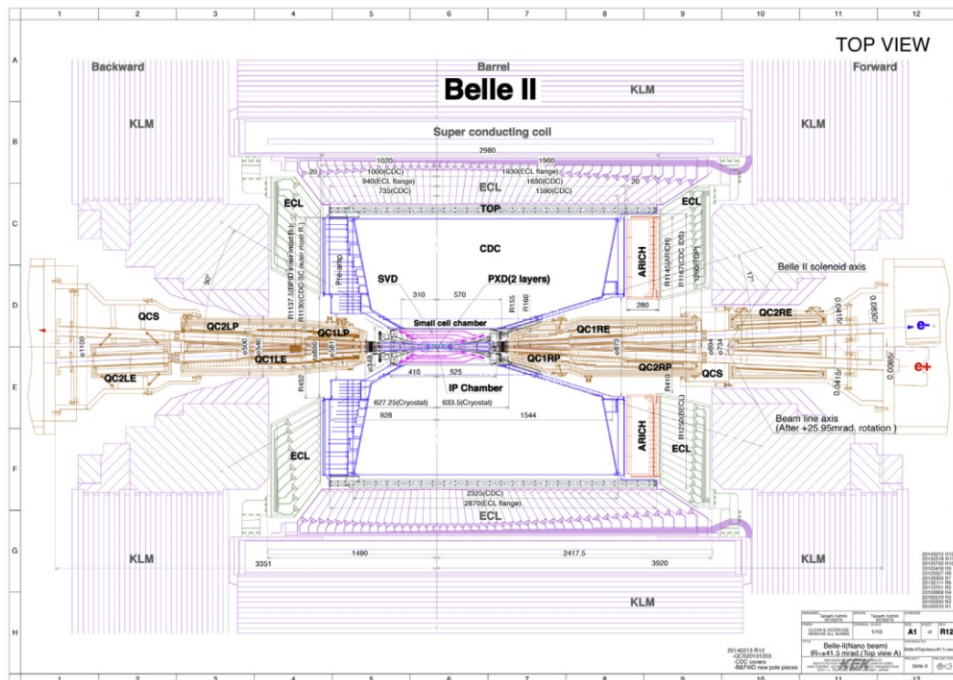
Figure 3.14: Top view of the Belle II layout [3]

3.4.1 Vertex Detector (VXD)

The Vertex Detector consists of the two sub-detector systems: Silicon Pixel Detector (PXD) and Silicon Vertex Detector (SVD). It is made up of six detector layers closest to the interaction region of the collider. Due to the nano-beam scheme at SuperKEKB, the beampipe radius at the interaction region is only about 10 mm. Since the background increases proportional to $1/r^2$, using only silicon strip detectors would give rise to a significant drawback, because of their high occupancy. The occupancy is defined as the ratio of the number of channels which register a hit to the overall number of channels of the detector. This high occupancy of silicon strip detectors in the vicinity of the interaction region renders them insufficient for the vertex reconstruction of B decays. Therefore, Belle II utilizes PXDs, which provide a significantly lower occupancy in comparison with silicon strip detectors, for the two innermost detector layers. For radii from 38 mm upwards, multiple layers of SVDs are used [2].

Figure 3.15 depicts the general structure of the vertex detector. Table 3.1 lists the radii and the number of ladders for each layer of the vertex detector [2].
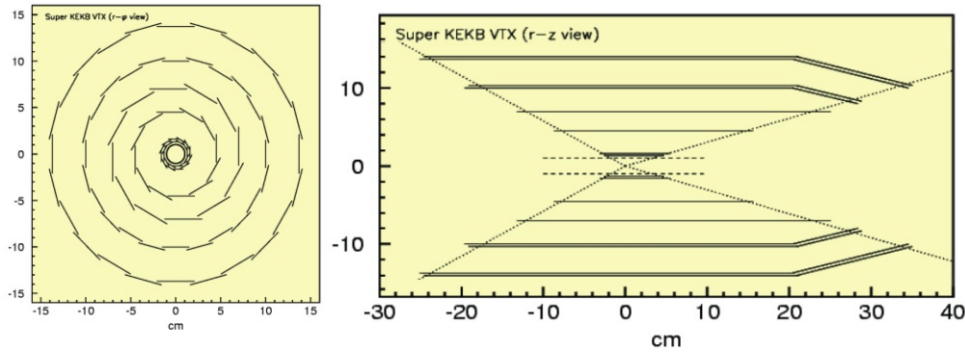
Figure 3.15: Schematic overview of the vertex detector. The two inner-most layers are the PXD, the SVD contains the adjacent 4 layers [30].

Detector	Radius [mm]	Num. of ladders
PXD	14	8
PXD	22	12
SVD	38	8
SVD	80	10
SVD	115	14
SVD	140	17

Table 3.1: Radii of the VXD layers.

3.4.2   Silicon Pixel Detector (PXD)

As mentioned above, the PXD contains the two detector layers in closest proximity to the interaction region of the collider. Since the PXD is based on DEPFETs (DEPleted Field Effect Transistors), it is equipped with a larger number of channels per area, resulting in a lower occupancy than silicon strip detectors. The layout of the PXD is depicted in figure 3.16. In the PXD, multiple DEPFETs are arrange in a matrix, where each cell is read out successively. Further advantages of the PXD layers include their thinness of about 50 μm and less multiple-scattering effects, as they are significantly thinner than SVD layers, which are about 300 μm thick, and the readout electronics are kept outside of the acceptance region [2].
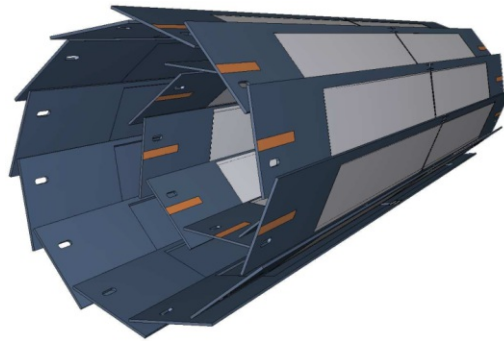
Figure 3.16: Geometrical layout of the two layers of PXD sensors. The grey areas correspond to the DEPFET pixel matrices. [2]

A DEPFET consists of a depleted bulk of silicon detector substrate with a p-channel MOSFET on top of it, which is shown in figure 3.17. When a charged particle or photon passes through the silicon bulk, electron-hole-pairs are created. The holes travel to the negatively charged back contact and the electrons drift to the internal gate under the FET gate. If the DEPFET is switched on, this accumulated charge of the electrons influences the current in the FET. Therefore, since the modulation of the FET current depends on the amount of electrons at the internal gate, its measurement not only allows for particle detection, but also enables the determination of the incident particle's energy [2].
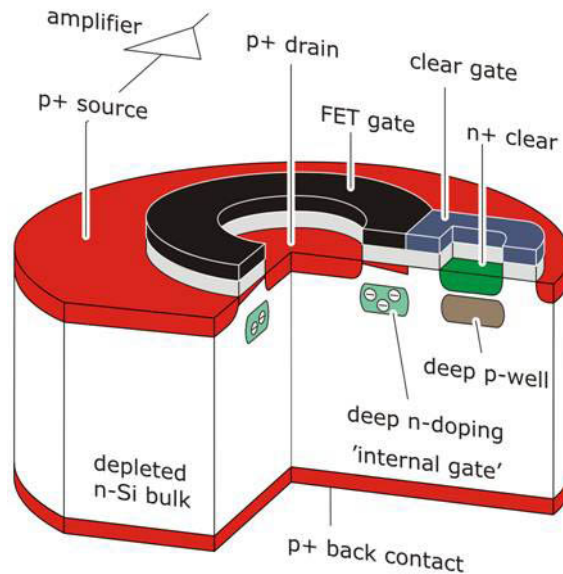
Figure 3.17: Schematic of a DEPFET [34].

3.4.3 Silicon Vertex Detector (SVD)

Adjacent to the PXD, the SVD is the second sub-detector of the vertex detector. Arranged in a ladder-configuration similar to the PXD, the SVD consists of four layers of double-sided silicon strip detectors (DSSD), with different numbers of ladders in each layer [2]. The working principle of silicon strip detectors is explained in a previous chapter of this thesis and the layout of the SVD is depicted in figure 3.18.
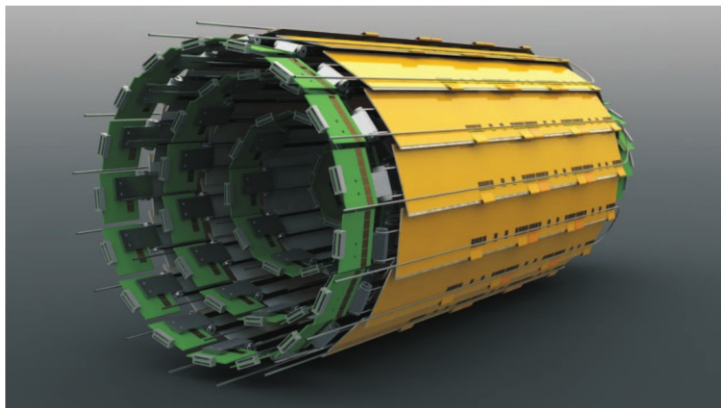
Figure 3.18: 3-D rendering of the four-layer SVD [2].

3.4.4 Central Drift Chamber (CDC)

The CDC is a gas-filled wire drift chamber and the main part of the Belle II tracking system. Its inner radius is 160 mm and its outer radius is 1130 mm. The CDC is structured into 9 superlayers, which contain 56 layers (8 in the first superlayer and 6 in each of the following ones) that consist of a total of 14336 gold-plated tungsten sense wires with a diameter of 30 μm and 42240 aluminium field wires. A schematic overview of the CDC wire configuration is depicted in figure 3.23 and its superlayer structure in figure 3.21. The sense wires are used for the detection of the electrons and the surrounding field wires provide a uniform electric field, which is shown in figure 3.19. In order to achieve a three-dimensional spacial tracking, two different wire types are alternated with each consecutive superlayer: axial wires in the beam-direction for the spacial detection in the r-ϕ-plane and stereo wires for the detection in the r-z-plane. The two types are shown in figure 3.20. The gas in use is a mixture of 50% He and 50% H_2C_6. Due to the magnetic field created by the solenoid surrounding large portions of Belle II, charged particles are forced on helical paths by the Lorentz force [2, 30, 39, 36].

Its three main purposes are [2, 30]:

- Reconstruction of charged tracks and the measurement of the incident particle's momentum.

- Particle identification due to the energy loss in the gas (following the Bethe-Bloch equation).

- Providing trigger signals to the electronics for charged particles.

sense wire ⊙
field wire •
drift circle ◯
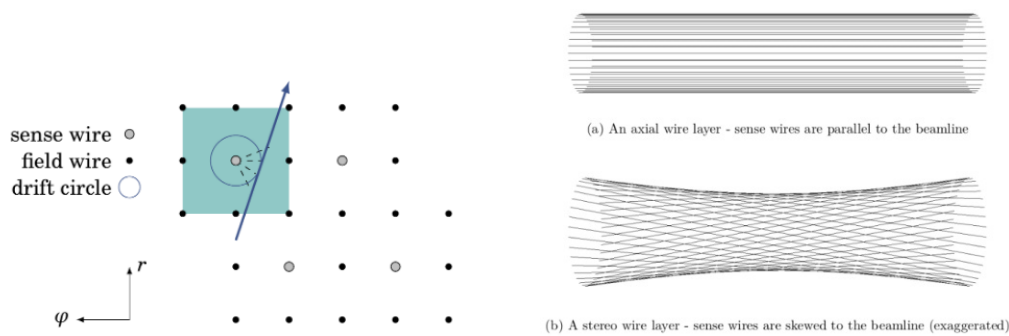
Figure 3.19: A wire cell inside the CDC [39].

(a) An axial wire layer - sense wires are parallel to the beamline

(b) A stereo wire layer - sense wires are skewed to the beamline (exaggerated)

Figure 3.20: Axial wire layer (top) and stereo wire layer (bottom) [39].
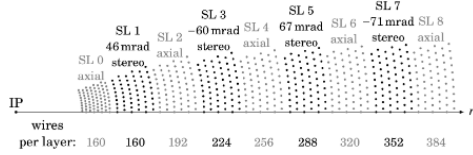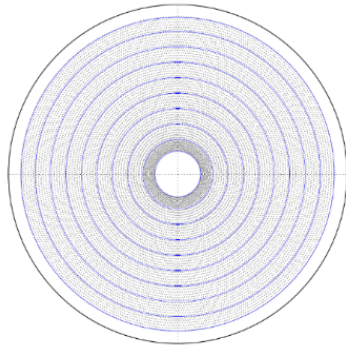
Figure 3.21: CDC superlayer structure [39].
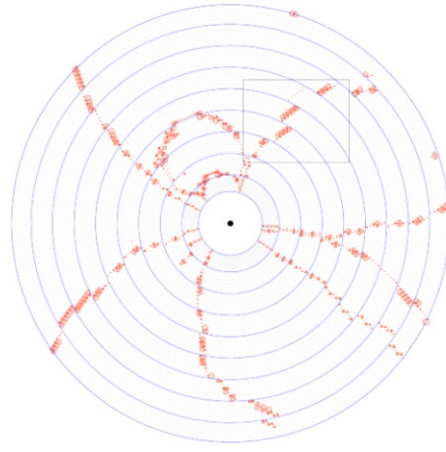
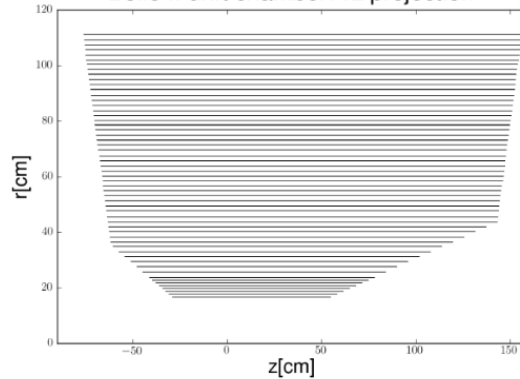Figure 3.22: An $\Upsilon(4S)$ event in the CDC [39].

Figure 3.23: Wire layout in the CDC [39].

3.4.5 Particle Identification System

In addition to the basic particle identification ability of the CDC, Belle II houses two distinct detector sub-systems for particle identification. These are a time-of-propagation (TOP) counter and an aerogel Cherenkov ring imaging detector (ARICH), which are both Cherenkov detectors. Their main task is to distinguish between kaons and pions. In the barrel region, the CDC is surrounded by 16 modules of TOP counters, each of which being made of a 45 cm × 2 cm quartz radiator. The ARICH detector is located at the forward end-cap region of the Belle II detector [2, 30].

TOP

The TOP counter is placed in the barrel region and consists of a quartz radiator and a photon detector. Its basic operating principle is depicted in figures 3.24 and 3.25.

When a charged particle passes through the quartz radiator, it produces Cherenkov radiation, which is reflected inside the radiator and eventually reaches the photon detector. Since the Cherenkov angle θ_C depends on the velocity of the incident particle, the Cherenkov photons for particles with different velocities will take separate paths inside the radiator. The information

about the point at which the particle enters the quartz radiator is provided by the CDC. A longer path takes the photons more time to reach the detector than a shorter one. Thus, measuring the time of propagation enables the determination of the incident particle's velocity. Furthermore, with the knowledge of the momentum and velocity of the particle, its mass can be calculated, which allows for the distinction of kaons and pions, due to their difference in mass [2, 30].
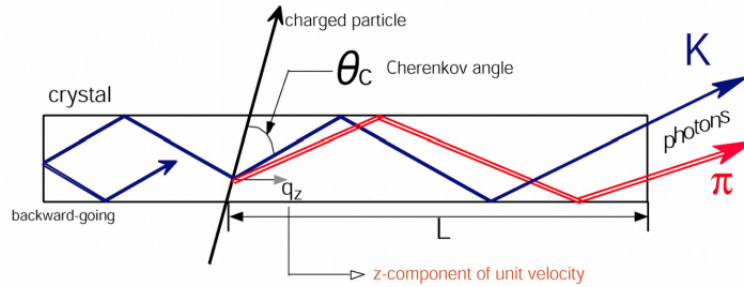

Figure 3.24: Physical working principle of the TOP counter [29].
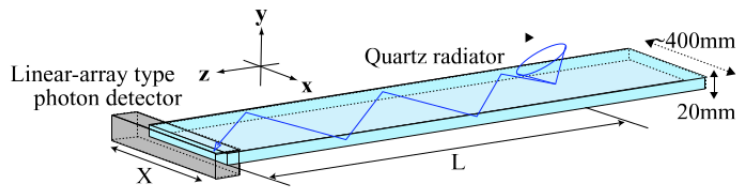
Figure 3.25: Schematic 3-D render of a TOP counter [2].

ARICH

The main purpose of ARICH is the identification of kaons and pions over their entire momentum range and the distinction between pions, muons and electrons with energies below 1 GeV. The ARICH detector and a visualization of a ring of Cherenkov photons hitting the detector are shown in figure 3.26. Similar to TOP, ARICH is also based on the detection of Cherenkov radiation. The ARICH detector is composed of 420 hybrid avalanche photon detectors (HAPD) grouped into seven concentric rings, which are located between two cylinders with inner and outer radii of 42 cm and 114 cm [2, 30, 33].

(a)   (b)
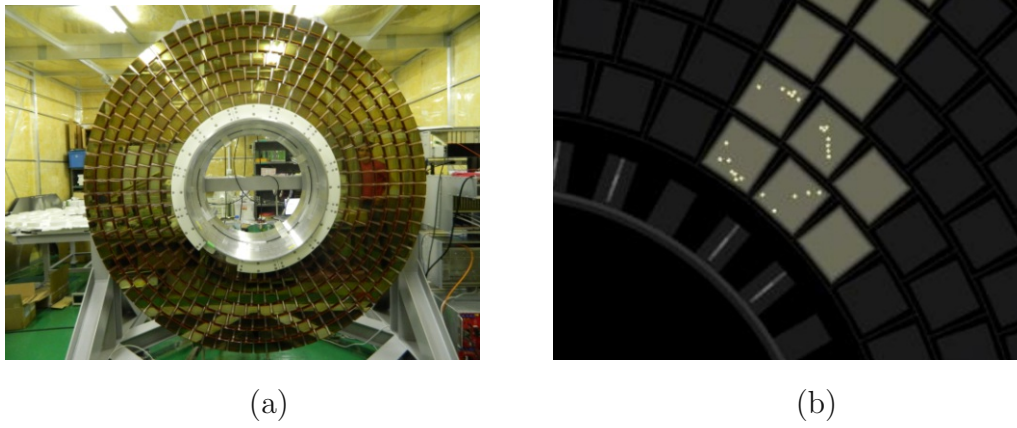
Figure 3.26: (a) The HAPDs of the ARICH detector. (b) Reconstructed hits of Cherenkov photons created by a cosmic muon [30].

While passing through the aerogel radiator, a charged particle produces Cherenkov radiation. The Cherenkov photons travel in the 20 cm long expansion volume until they reach the photon detector, where the hits are registered. The hits form the shape of a ring, from which the Cherenkov angle θ_C and, analogous to TOP, the mass of the incident particle can be determined. In order to focus the photons and achieve a higher yield, the aerogel radiator consists of two 2 cm thick layers with different refractive indices n_1 and n_2 [2, 30]. This working principle is depicted in figure 3.27.
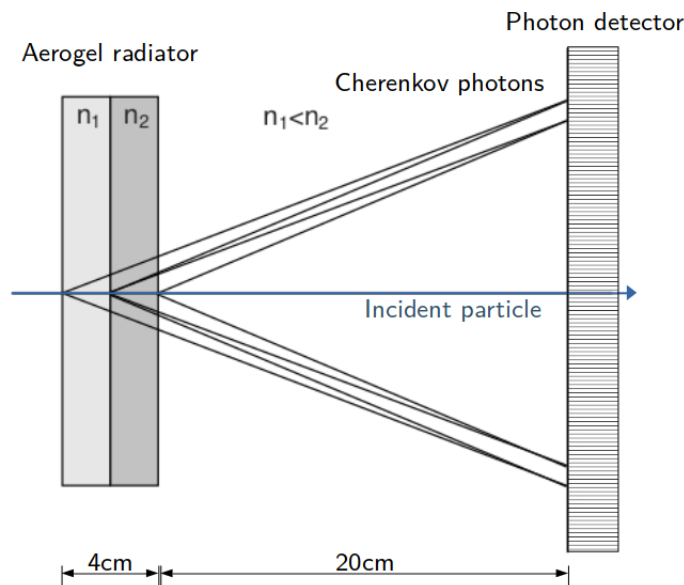
Figure 3.27: Schematic working principle of ARICH (figure adapted from [2]).

3.4.6 Electromagnetic Calorimeter (ECL)

The ECL of Belle II serves multiple purposes, which include, but are not limited to, the detection of photons and the measurement of their momentum and location, as well as the distinction between electrons and hadrons. Detecting photons is of utmost importance at Belle II, since nearly $1/3$ of all B decays include $\pi^0 \to \gamma\gamma$ sub-decays [2, 30]. Electrons and photons are completely stopped in the ECL.

The location of the ECL in the Belle II detector is shown in figure 3.14. Spanning across 90% of the CMS-frame solid angle, it consists of 8736 crystals, of which 6624 are thallium-doped caesium iodide CsI(Tl) crystals in the 3 m long barrel region and 2112 pure CsI crystals in the end-cap regions. Each crystal in the form of a truncated pyramid has a cross section of about 6×6 cm^2 and a length of 30 cm, which is approximately 16 X_0 [2, 30].

3.4.7 K_L and muon detector (KLM)

Being the only sub-detector system of Belle II that is located outside of the 1.5 T strong superconducting solenoid, the KLM is used to detect K_L mesons and muons. It consists of alternating layers of 4.7 cm thick iron plates, that also function as a magnetic field return for the solenoid field and additional material for K_L mesons to create hadronic showers, and active detector elements. Muons and non-showering hadrons with a momentum above 0.6 GeV pass through the KLM without generating hadronic showers, but leave hits. K_L mesons produce hadronic showers and are stopped in the KLM [2, 30].

In order to identify muons, the following procedure is performed [2]:

- Reconstruction of a charged track in the CDC.

- Extrapolation of the track beyond the last CDC layer into the KLM using the pion hypothesis.

- Further consideration of the track, if at least the first resistive plate chamber layer of the KLM is reached, which is the case for a momentum greater than 0.6 GeV.

- Comparison of the outermost KLM layer, that should be hit by the extrapolated track, and the layer, that actually registered a hit.

- If those values differ significantly, the particle is identified as a hadron, otherwise, a new extrapolation is executed using the muon hypothesis.

Hits in the KLM that are close together are grouped into clusters. Under certain conditions, clusters are discarded. Otherwise, the K_L candidates are classified as KLM-only K_L candidates, if the cluster has hits in at least two different layers of the KLM, or KLM+ECL K_L candidates, if the cluster contains at least one hit in the KLM and ECL [2]. The tracking at Belle II will be described in more detail in the following chapter.

3.4.8 Trigger system

Due to the tremendous amount of events generated at SuperKEKB, it is not feasible to store the entire data. This is especially necessary because of SuperKEKB's high design luminosity of $8 \cdot 10^{35}$ cm^{-2} s^{-1}. Therefore, only information that could be relevant for later analysis should be kept. At Belle II, the decision about which events are being stored and which data is discarded is made by the trigger system [30].

The trigger system consists of two stages [30, 2]:

- **Low level trigger (L1):** Hardware based trigger used while SuperKEKB is running, that decides, which data is stored.

- **High level trigger (HLT):** Software based trigger applied to a full event reconstruction based on data input from all detectors that passed L1 to decrease the amount of data for subsequent analysis.

The low level trigger has to fulfill many requirements, for example, a high efficiency for hadronic events from $\Upsilon(4S) \to B\bar{B}$, a minimum event separation of 200 ns, a 30 kHz maximum trigger rate and a less than 10 ns precision of timing [2, 28, 27]. It is composed of four sub-triggers, that independently gather trigger information, which is combined in the global decision logic (GDL) (see figure 3.28) to a final trigger decision [30, 2, 27, 28]:

- **CDC trigger:** Detects charged tracks based on the CDC information (e.g. momentum and position).

- **ECL trigger:** Yields information about the total energy of particles, clusters and the identification of Bhabha and $\gamma\gamma$ events from the energy deposited in the ECL.

- **BPID trigger:** Uses the measurements from TOP to gain information about the hit topology and timing.

- **KLM trigger:** Provides muon tracking information.
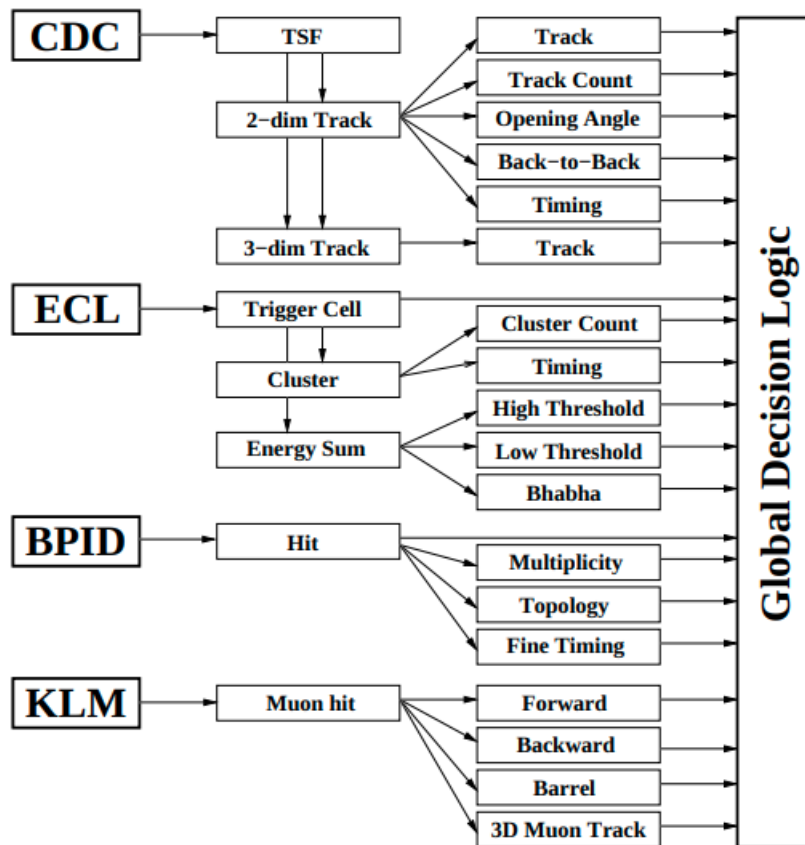
Figure 3.28: Overview of the trigger information flow from the sub-triggers to the GDL [27].

Chapter 4

Track reconstruction at Belle II

The reconstruction of charged tracks consists of two main steps. At first, hits in the tracking detectors – PXD, SVD and CDC – are combined to possible tracks of charged particles. This step is called track finding. Secondly, in order to gain information about the track parameters, a process called track fitting is performed. Those track parameters are needed for the extrapolation of particle tracks beyond the tracking detectors into TOP, ARICH, ECL and KLM [14]. Particle identification is made possible by combining the additional information from TOP, ARICH, ECL and KLM with the extrapolated tracks.

4.1 Track finding

In this section, the track finding at Belle II will be described closely following the references [12, 14]. The aim of track finding is to utilize the information from the PXD, SVD and CDC in order to combine their registered hits into the tracks of particles passing through the Belle II detector. Furthermore, the information gained from the reconstructed tracks is used for the identification of particles. Due to the different benefits and disadvantages of the tracking detectors, there is not one single algorithm suited for the PXD, SVD and CDC. Therefore, for the process of track finding, multiple algorithms considering the detectors' behavior are used independently and their results are combined. A simplified overview of this workflow is shown in figure 4.1.

4.1.1 CDC algorithm

The track reconstruction for CDC hits consists of two algorithms, the global and the local algorithm. The first one searches for hit patterns that are consistent with helix trajectories and the latter one is used for the reconstruction of short tracks and tracks whose origin is offset to the interaction point. The local algorithm is applied after the global algorithm.

Calculated from the drift time, the CDC provides the relative distance to the sense wires at which particles passed through the CDC as input for the CDC track finding algorithms. Furthermore, the amplitudes measured at the sense wires give information about the energy loss of the traversing particle and are used for particle identification [12].
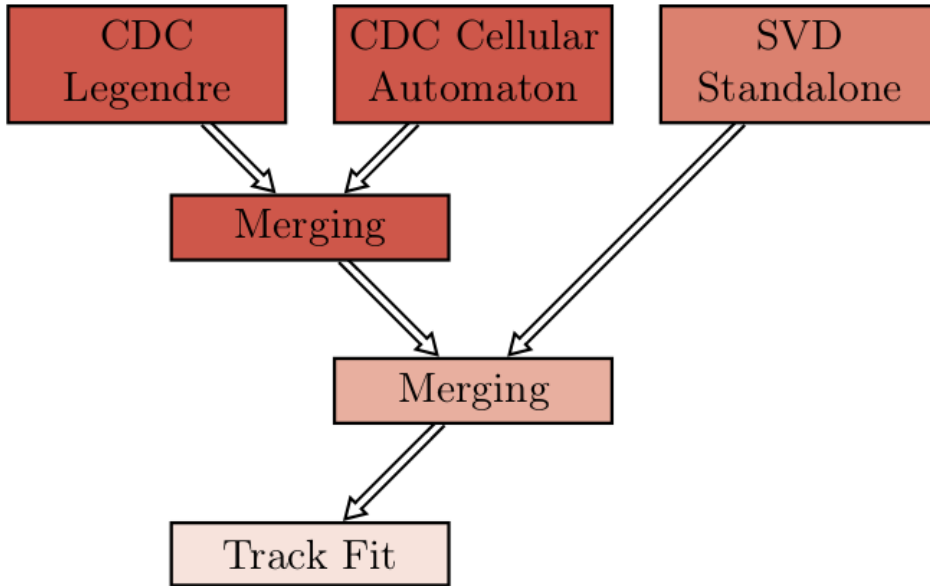
Figure 4.1: Schematic overview of the algorithms used in the track finding process [14].

Global algorithm

The global algorithm is the primary algorithm used for the CDC reconstruction and is based on the Legendre transformation. It is called global algorithm, since a conformal mapping is applied to all CDC hits simultaneously. At first, two-dimensional track finding in the r-ϕ plane of the detector is performed using the information of axial wires. Subsequently, the track finding is expanded to three dimensions by adding the information of stereo wires. Representing a CDC wire in the r-ϕ plane, the relative distance only gives information about the value of r relative to the CDC wire and no information about ϕ. Therefore, a particle could have passed the sense wire at all values of ϕ with a fixed value of r. This defines a so called drift circle [12, 14].

The usage of the Legendre transformation is motivated by the fact that the particle's path has to be tangent to every drift circle along its way through the CDC. This is shown in figure 4.2a. In order to calculate the Legendre transformation of a circle with its origin at (x_0, y_0) and a radius of R, the circle is defined piecewise as [5]

$$
\begin{cases}
f_1(x) = y_0 + \sqrt{R^2 - (x - x_0)^2} \\
f_2(x) = y_0 - \sqrt{R^2 - (x - x_0)^2}
\end{cases}
\tag{4.1}
$$

for the concave and convex parts, which is depicted in figure 4.2b. The Legendre transformation

$$
\begin{cases}
F_1(p) = f_1(x(p)) - px(p) \\
F_2(p) = f_2(x(p)) - px(p)
\end{cases}
\tag{4.2}
$$

with

$$
p = \frac{df}{dx}
\tag{4.3}
$$

yields

$$
\begin{cases}
F_1(p) = y_0 - px_0 + R\sqrt{p^2 + 1} \\
F_2(p) = x_0 p - y_0 + R\sqrt{p^2 + 1}
\end{cases}
.
\tag{4.4}
$$
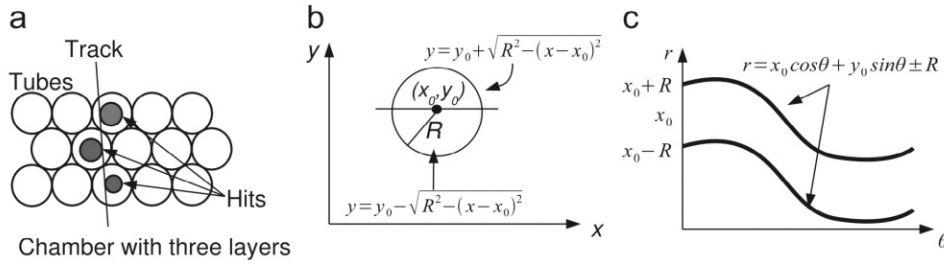
Figure 4.2: (a) A charged track passing by CDC wires and their drift circles. (b) Piecewise definition of a circle. (c) r-θ representation of the Legendre transformed circle [5].

Using the geometric relations shown in figure 4.3, this result can be written as

$$\rho = x_0 \cos(\theta) + y_0 \sin(\theta) \pm R_{dr}, \tag{4.5}$$

where R_{dr} is the radius of the drift circle. In some papers, the variable r is used instead of ρ, for example in reference [5]. Therefore, the Legendre transformation transforms every drift circle into a pair of sinusoids in the ρ-θ parameter space, which is depicted in figure 4.2c. Thus, the task of track-finding is reduced to finding the areas in the ρ-θ space with the highest density, which is performed by a two-dimensional binary search algorithm. This is shown in figures 4.4 and 4.5, respectively. A similar approach is used for the expansion of the track finding to three dimensions by including the information of the stereo wires [12].
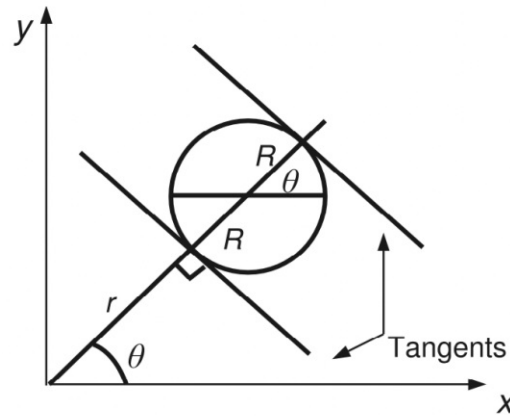
Figure 4.3: Geometry on which the r-θ parametrization is based on [5].

Local algorithm

The local algorithm is used after the global algorithm and has no predefined assumptions about the origin of the tracks. Searching for segments (associated hits in the superlayers of the CDC) is the main purpose of the algorithm and it even works if the information of one CDC layer is missing. It is based on a weighted cellular automaton, which enables to perform track finding by maximizing the energy function

$$E_i = \sum w_{ij} + \sum \Theta_j, \tag{4.6}$$
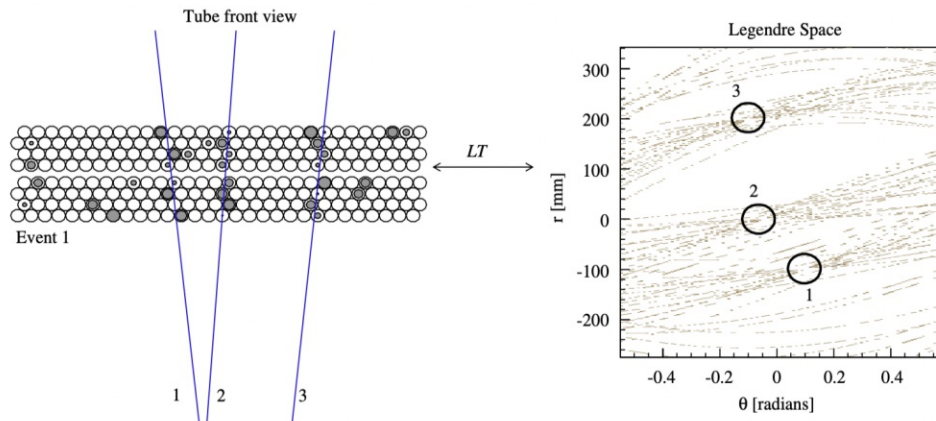
Figure 4.4: An example for the Legendre transformation of CDC hits [5].
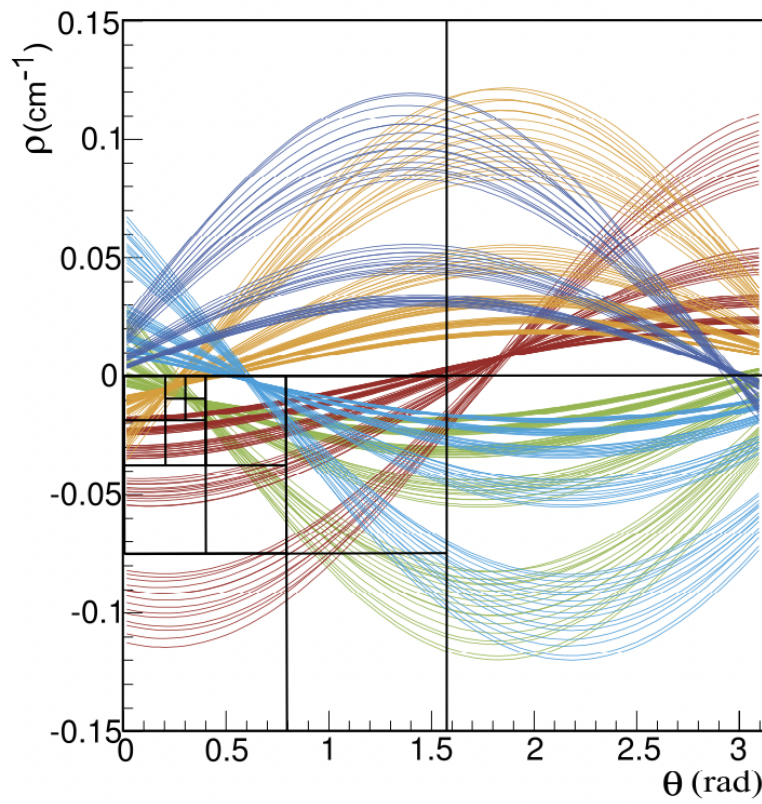
Figure 4.5: Visualization of the two-dimensional binary search [12].

where Θ_i and w_{ij} are the weights of the vertex i and edge between the vertices i and j, respectively [12, 14].

Since it is heavily used in the local algorithm, the χ^2 value calculation will be briefly described. Parameters of a function can be fitted by minimizing χ^2, the squared distance between the mathematical model and the measured data. It is defined as [14]

$$\chi^2 = (\mathbf{y} - \mathbf{f}(\mathbf{x}))^T \mathbf{V}^{-1} (\mathbf{y} - \mathbf{f}(\mathbf{x})). \qquad (4.7)$$

Here, $\mathbf{y} = (y_1, y_2, \ldots, y_n)$ is the data vector, $\mathbf{f} = (f_1, f_2, \ldots, f_n)$ the functions of the mathematical model, depending on m parameters $\mathbf{x} = (x_1, x_2, \ldots, x_m)$, and $\mathbf{V}$ the covariance matrix of the data. Even though the minimization can be performed directly and efficiently if the functions $\mathbf{f}$ are analytically known, it quickly becomes unfeasible when iterative numerical calculations, for example gradient-descent methods, have to be applied. Therefore, the χ^2 minimization is only used in intermediate stages and the final track fit is calculated with a customized Kalman filter [14]. A short description of the Kalman filter will be given in the next section.

The local algorithm consists of the following two steps [12]:

1. **Segment building:** At first, vertices are created by combining three neighbouring hits. A least-squares method is used to calculate a trajectory tangent to all three drift circles. The corresponding χ^2 value of this fit is used to yield the weight Θ_j. If vertices share two drift circles, they are combined to edges. Their weights w_{ij} are calculated from the χ^2 value of the fit of a straight line tangent to all drift circles of the edge.

2. **Track building:** The segments in the axial- and stereo-wire superlayers built in the previous step are now combined to tracks. Vertices consisting of a pair of adjacent segments in axial- and stereo-wire superlayers are formed. Their weights Θ_i are calculated with a χ^2 circle fit employing the Riemann method. The edges of the cellular automaton are created from vertices that share a common segment. Their weights w_{ij} are yielded from the χ^2 value of a fit taking into account for hits in every segment. This process of track building from the nodes and edges of the constructed graph using a cellular automaton is depicted in figure 4.6. The reconstruction is then performed by searching for the path with the largest possible sum of weights, es written in equation 4.6.

Combination of the results

In order to benefit from the individual advantages of the global and local algorithms, the results of both track finding algorithms are combined. On the one hand, the global algorithm works even with missing information from several layers. On the other hand, the efficiency of the local algorithm is independent of the track's origin. The global track finding candidates provide the foundation to which the local track finding candidates are added by using FastBDT, a multivariate decision tree [12].
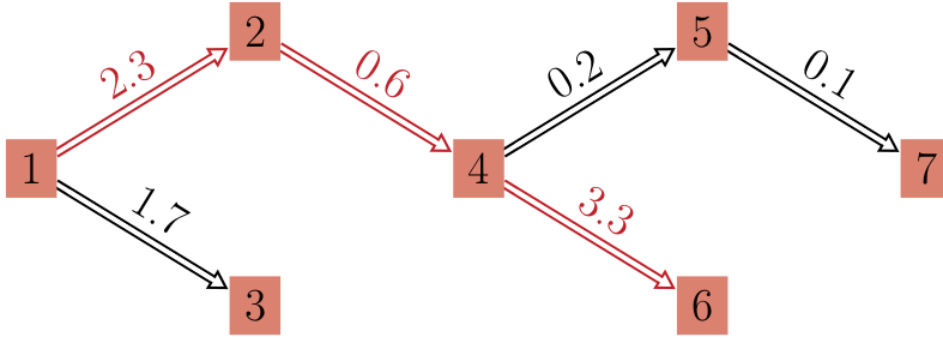
Figure 4.6: Example of path finding by maximizing the sum of weights using a cellular automaton. Here, the red path yields the largest sum [14].

4.1.2 Combinatorial Kalman Filter

In general, the Kalman filter is an iterative estimator algorithm, that based on an initial start configuration enhances its precision with each step. For linear dynamic systems, the linear Kalman filter represents the best recursive estimator. This is achieved by comparing each calculated prediction with its corresponding measurement and correcting the prediction with this information to increase the agreement. In order to apply the Kalman Filter, the evolution of the state $\mathbf{x}(z_k)$ of the discrete system is expressed in the form of [26]

$$\mathbf{x}(z_k) = \mathbf{x}_k = \mathbf{f}_{k-1}(\mathbf{x}_{k-1}) + \mathbf{w}_{k-1}, \tag{4.8}$$

where $\mathbf{f}_{k-1}$ is the propagator function from step $k-1 \to k$ and $\mathbf{w}_{k-1}$ is a random variable, called process noise. The variables of the state vector in the case of Belle II are five parameters that describe the helical trajectory of a charged particle in a magnetic field, which are described in section 4.2. Since it is often impossible to observe the state $\mathbf{x}_k$ itself, the measurements $\mathbf{m}_k$ are defined as

$$\mathbf{m}_k = \mathbf{h}_k(\mathbf{x}_k) + \boldsymbol{\epsilon}_k, \tag{4.9}$$

with the detector response $\mathbf{h}_k$ and noise $\boldsymbol{\epsilon}_k$. Furthermore, it is assumed that the mean value of $\mathbf{w}_k$ and $\boldsymbol{\epsilon}_k$ is equal to zero and that all of their values are independent [14, 26].

For discrete linear dynamic systems these relations can be expressed with vectors and matrices as

$$\mathbf{x}_k = \mathbf{F}_{k-1}\mathbf{x}_{k-1} + \mathbf{w}_{k-1} \tag{4.10}$$

$$\mathbf{m}_k = \mathbf{H}_k\mathbf{x}_k + \boldsymbol{\epsilon}_k. \tag{4.11}$$

The extrapolation for the state vector $\mathbf{x}_k^{k-1}$, taking into account measurements until $k-1$, and its covariance matrix $\mathbf{C_k^{k-1}} = \text{cov}(\mathbf{x}_k^{k-1} - \mathbf{x}_{k,t})$, where $\mathbf{x}_{k,t}$ is the true value of the state, is calculated by

$$\mathbf{x}_k^{k-1} = \mathbf{F}_{k-1}\mathbf{x}_{k-1} \tag{4.12}$$

$$\mathbf{C}_k^{k-1} = \mathbf{F}_{k-1}\mathbf{C}_{k-1}\mathbf{F}_{k-1}^T + \mathbf{Q}_{k-1}, \tag{4.13}$$

where $\mathbf{Q}_{k-1} = \text{cov}(\mathbf{w}_{k-1})$ [14, 26].

Next, the state vector is corrected using the residual $\mathbf{r}_k^{k-1} = \mathbf{m}_k - \mathbf{H}_k\mathbf{x}_k^{k-1}$, which is the deviation of the prediction from the measurement. With the Kalman gain matrix defined as

$$\mathbf{K}_k = \mathbf{C}_k^{k-1}\mathbf{H}_k^T \left(\mathbf{V}_k + \mathbf{H}_k\mathbf{C}_k^{k-1}\mathbf{H}_k^T\right)^{-1}, \tag{4.14}$$

the state vector and covariance updates are calculated by [26]

$$\mathbf{x}_k = \mathbf{m}_k^{k-1} + \mathbf{K}_k \left(\mathbf{m}_k - \mathbf{H}_k \mathbf{x}_k^{k-1} \right) \tag{4.15}$$

$$\mathbf{C}_k = \left(\mathbb{1} - \mathbf{K}_k \mathbf{H}_k \right) \mathbf{C}_k^{k-1}. \tag{4.16}$$

Using the above formulas, the Kalman filter algorithm follows the steps [14, 26, 13]:

- **Initialization:** The initial state values $\mathbf{x}_0$ and their covariance matrix $\mathbf{C}_0$ are chosen.

- **Extrapolation:** The state $\mathbf{x}_k$ and its covariance matrix $\mathbf{C}_k$ are predicted from $\mathbf{x}_{k-1}$ and $\mathbf{C}_{k-1}$.

- **Update:** The deviation of the prediction $\mathbf{x}_k$ from the measurement $\mathbf{m}_k$ is used to correct $\mathbf{x}_k$. Repeat from the extrapolation with $k \rightarrow k+1$, until the iteration reached the last data point.

- **Smoothing:** Rerun the algorithm with the calculated states as new seeds and also rerun it in reverse order, so from the last to the first data point. A smoothed track is obtained by calculating the weighted average of the forward and backward runs. This yields a better estimation.

A flow chart for the Kalman filter is shown in figure 4.8 and one such iteration is depicted in figure 4.7.

(a) Estimate of the parameters (blue) with uncertainties (blue band) before using data from layer 5.

(b) Extrapolation of the state (red) to the next layer (4 to 5).

(c) Kalman update of the state (blue) using the extrapolated position (red) and the measurement (black) on layer 5.

(d) Usage of the updated states for the next extrapolation (red).
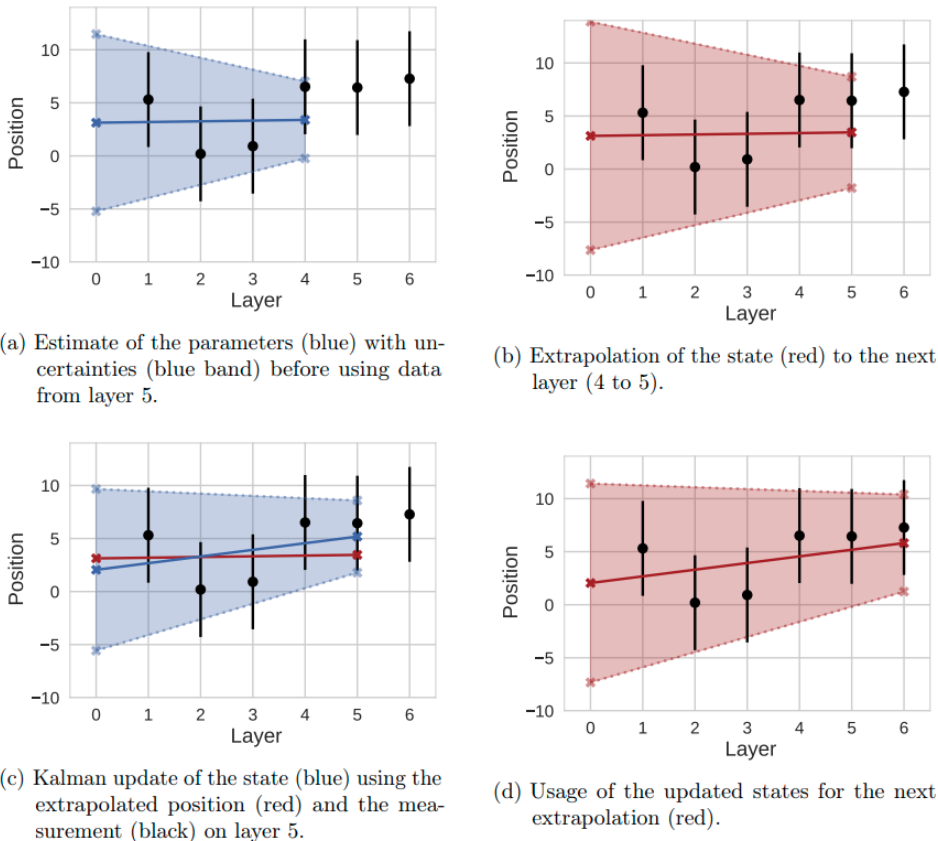
Figure 4.7: A visualization of one iteration of the Kalman filter, taken from [14].
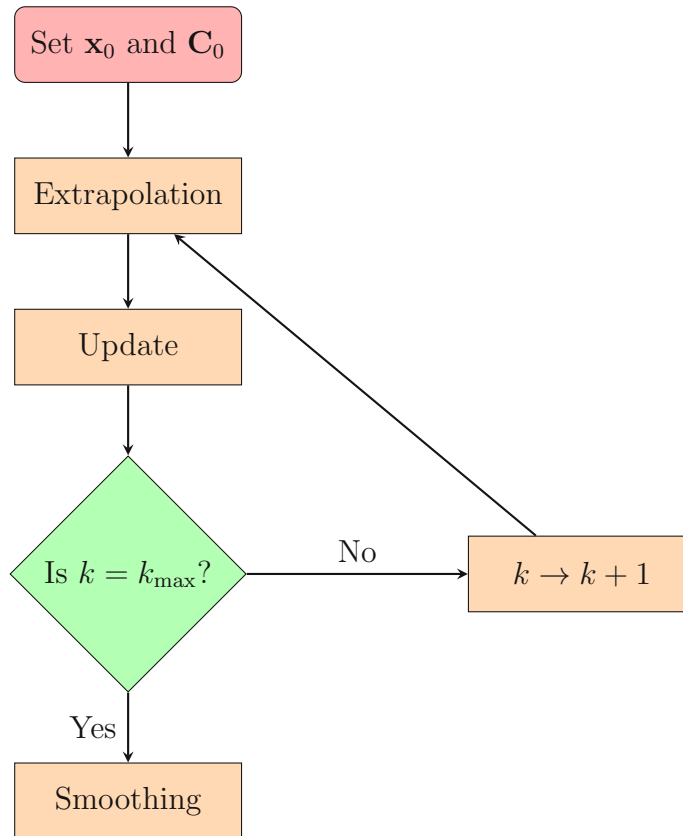
Figure 4.8: Flow chart for the Kalman filter.

At Belle II, an adapted and extended version of the Kalman Filter, the combinatorial Kalman filter (CKF), is used to combine the previously reconstructed CDC tracks with SVD hits. The CDC track candidates act as the seeds for the CKF and are extrapolated into the detector volume using the Runge-Kutta-Nyström method. Assuming the pion mass hypothesis, since pions constitute the majority of charged particles in $\Upsilon(4S)$ events (as seen in figure 4.9), the CDC seeds are fitted with a deterministic annealing filter (DAF) algorithm. The underlying principle of the DAF is a Kalman filter, which is extended to calculate weighted averages of the hits in a layer. Its main advantage is the rejection of outliers [12, 13].

Based on the extrapolated track position and considering track uncertainties, the next SVD hit candidate is selected and added to the track candidate. A new track extrapolation is calculated including the newly added SVD hit and again, a plausible SVD hit candidate is chosen and added to the track. This process is iterated until the track candidate reaches the PXD. Afterwards, a slightly different process is used on the remaining unmatched SVD space points [12].

In order to suppress background hits, a filter based on FastBDT, that has previously been trained on simulated Monte Carlo data, is applied during the algorithm.

The reconstructed CDC-SVD tracks are used to locate regions of interest in the PXD. PXD clusters in those regions provide the input for another CKF application, in which appropriate clusters are attached to the CDC-SVD tracks.
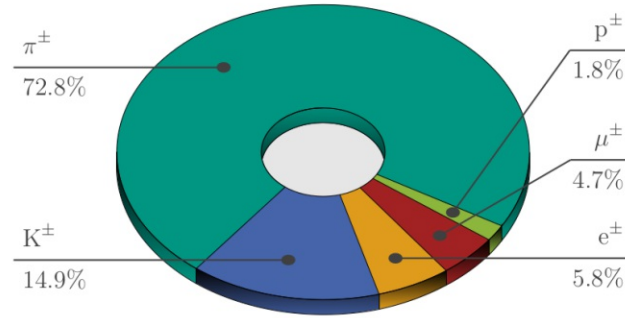
Figure 4.9: Fractions of charged particles in $\Upsilon(4S)$ events [12].

4.1.3 SVD standalone algorithm

Supplementary to the CKF, an additional algorithm is applied for the reconstruction of SVD hits of low momentum particles, for example slow pions. Particles with a transverse momentum $p_t < 100$ MeV do not result in enough CDC hits to be eligible for the CKF algorithm. The SVD standalone algorithm consists of three parts [12]:

1. Related SVD space points are connected by graphs based on geometrical information. Hereby a Sector Map is utilized.

2. A cellular automaton is used on the graphs to acquire a set of possible paths.

3. Selection of the optimal paths.

Sector Map

At first, each SVD sensor is split into a 3×3 array of sectors. The Sector Map is a construct that stores the information about possible tracks that connect the space points in the different sectors. Using the temporal data of the hits, the direction of the track can be deduced. In order to filter out background events, multiple selection criteria are implemented at the creation of the Sector Map, e.g. the distance, detection time, ϕ and θ angles between space points. The Sector Map is trained on Monte Carlo simulation data to learn the possible directed relations between the individual sectors, the SVD geometry and ranges for the selection criteria [12].

Track finding algorithm

At first, a directed graph that uses all sectors with registered hits as nodes is built per event. This graph is called a sector network. The above mentioned Sector Map provides information about the edges connecting the nodes for each active sector [12].

Secondly, all SVD space points on the active sectors form the nodes of a graph, called space point network. It obtains its edges, that pairwise combine space points to segments, from the sector network. These two steps are shown in figure 4.10(a) and (b). If pairs of segments share a common space point, they form space point triplets, as depicted in figure 4.10(c). Thereby, a new graph with segments as nodes is created – the segment network. During the combination steps Sector Map filters are applied [12].

The edges of the segment network form paths, of which all paths with a length of at least three space points are selected as possible track candidates. In order to identify the longest path of the graph, a similar cellular automaton to the one for the local CDC algorithm is utilized [12].

All tracks sharing SVD clusters are discarded from the final set of track candidates. This increases the purity of the tracks by a factor of about 2. For the case that two or more track candidates include common hits, their χ^2 value of the Triplet Fit (based on [10]) is used to calculate a quality indicator for each track. Subsequently, the track with the highest quality indicator is chosen, see figure 4.10(d) [12].

(a) Space point creation.

(b) Two hit combinations.

(c) Three hit combinations.

(d) Final track.
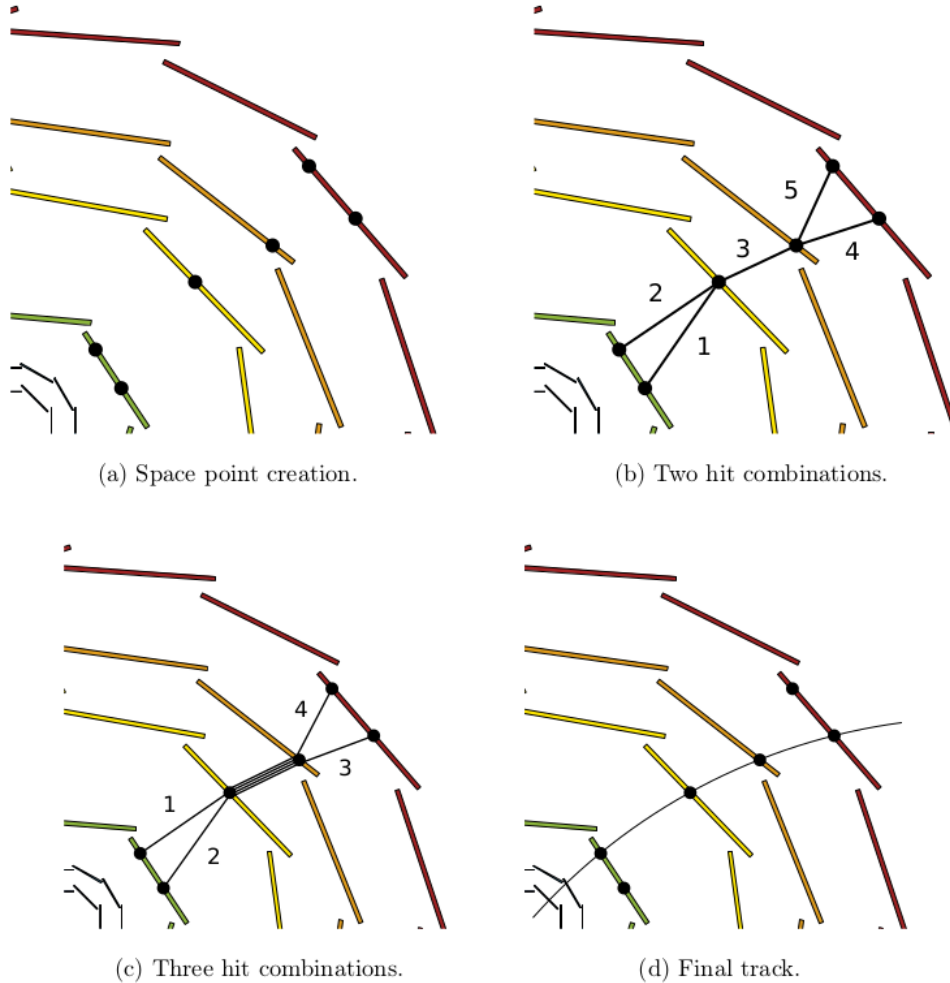
Figure 4.10: Steps of the SVD standalone algorithm as described in the section above [14].

4.2 Track fitting

The primary track fitting algorithm at Belle II is based on a deterministic annealing filter, that itself is based on a Kalman filter considering the particle-material interactions. In order to fit the track candidates to the PXD, SVD and CDC hits, Belle II uses a parametrization for the particle trajectories set in relation to the particle's point of closest approach (POCA) to the origin of the r-ϕ plane. The five parameters for the helical particle trajectories in the magnetic field are [12, 30]:

- **d_0**: The signed distance between the POCA and the z-axis, which is the origin of the r-ϕ plane.

- **z_0**: The longitudinal distance between the POCA and the origin, which is equivalent to the z-coordinate at the POCA.

- **ϕ_0**: The angle between the x-axis and the transverse momentum at the POCA.

- **$\tan(\lambda)$**: The tangent of the angle between the momentum at the POCA and the r-ϕ plane.

- **w**: The charge dependent signed curvature of the charged track.

4.3   ECL reconstruction

The position and size of hit clusters left in the ECL by electromagnetic showers from charged and neutral incident particles are used for the energy and position reconstruction of particles. Since photons and neutral hadrons do not leave hits in the PXD, SVD and CDC, the ECL reconstruction is especially important for their track reconstruction. However, it can also improve the reconstruction of electrons and charged particles, if they did not leave enough hits in the tracking detectors. Furthermore, the information gather from the ECL reconstruction is used to differentiate between photons, electrons, muons, charged and neutral hadrons. Additionally, measuring the whole deposited energy in the ECL provides a way to determine boundaries for the missing energy of neutrinos, which otherwise pass through the detector without a trace [30].

The clusters are reconstructed by searching for ECL crystals with a local energy maximum exceeding a certain threshold. Adjacent crystals with an energy above a background-suppressing threshold are combined to connected regions. In each connected region, crystals with a local energy maximum are declared as origins of clusters. Using different weights calculated from the ECL measurements, every crystal of a connected region is allocated to a cluster. Finally, the weighted center of each cluster and its weighted total energy are calculated [30].

4.4   Particle identification

4.4.1 V^0-like particle reconstruction

In general, V^0-like particles are neutral particles with long lifetimes that decay into two charged particles. Due to their neutral charge, they do not leave hits in the tracking detectors. Therefore, they are reconstructed by combining the tracks of their two charged decay products to a common vertex.

All tracks with opposite charge are pairwise extrapolated to their hits closest to the interaction point. Successfully extrapolated tracks are subsequently fitted to their interaction vertex using the software package RAVE [42]. A combination is discarded from the candidate list, if this reconstruction fails. Successful candidates are further filtered with criteria based on the χ^2 value of the vertex fit and their mass. The V^0 reconstruction is performed after the charged track reconstruction [30].

4.4.2 Charged particle identification

The identification of charged particles at Belle II is based on the measurements of the PID detectors, TOP and ARICH, in combination with the information about ionization energy loss dE/dx gained from the SVD and CDC. Additionally, the ECL and KLM provide information for the identification of electrons and muons, respectively [30].

At first, the PID information of every detector system is analyzed by individually considering each of the long-lived charged particle hypotheses. Those consist of hypotheses for electrons, muons, pion, kaons, protons and deuterons. Subsequently, the difference of the log-likelihood functions $\mathcal{L}(\alpha)$ and $\mathcal{L}(\beta)$ of two different particle hypotheses α and β are used to calculate the PID value $\mathcal{L}(\alpha : \beta)$ as

$$\mathcal{L}(\alpha : \beta) = \frac{1}{1 + e^{\ln(\mathcal{L}(\alpha)) - \ln(\mathcal{L}(\beta))}} = \frac{\prod_{\mathrm{det}} \mathcal{L}(\alpha)}{\prod_{\mathrm{det}} \mathcal{L}(\alpha) + \prod_{\mathrm{det}} \mathcal{L}(\beta)}, \tag{4.17}$$

where the product is taken over the detectors corresponding to the particle hypothesis in question. If $\mathcal{L}(\alpha : \beta) > 0.5$, the track is more likely to stem from a particle of type α than β [30].

dE/dx measurements

The energy loss due to ionization of particles traversing the CDC and SVD follows the Bethe-Bloch equation, which is explained in a previous section of this thesis. The dE/dx measurement should only depend on $\beta\gamma = \frac{p}{m}$ and, because of the similar behavior of the dE/dx for pions and kaons with larger values of $\beta\gamma$, the particle identification based on dE/dx information is better suited for low momentum particles, with $p \lesssim 1$ GeV. From the dE/dx measurements, a prediction, the amount of hits and the track's polar angel, a χ value for each particle type is calculated, which can be transformed into a likelihood [30].

The likelihood calculations for TOP, ARICH and KLM are more involved, thus their discussion is outside the scope of this thesis.

For the identification of electrons, the CDC, SVD, ECL ionization energy loss, TOP and ARICH likelihoods are combined to a final resulting likelihood. Furthermore, the value of E/p provides a good measure for the distinction of electrons and other charged particles for $p \geq 1$ GeV [30].

4.4.3 Photons, π^0 and K_L^0

Due to its cylindrical symmetry and exponential energy loss, the shape of electromagnetic showers generated by photons in the ECL is very distinctive. Furthermore, photon candidates are only built from ECL clusters, which have not been matched to track candidates, since photons leave no hits in the SVD and CDC. By combining two photon candidates, π^0 mesons are reconstructed, since the $\pi^0 \to \gamma\gamma$ decay has a branching fraction of about 98.8 % [44]. K_L^0 clusters are classified using the ECL and KLM information in conjunction with the application of Stochastically Gradient Boosted Decision Trees [30].

Chapter 5

Determination of the relative slow pion efficiency

The aim of this chapter is to describe the different stages of the data analysis that has been performed for this thesis. In principle, the goal is to calculate the ratio between the signal yield of the real and Monte Carlo (MC) data in order to gain insights about the slow pion tracking efficiency. This real data signal yield is extracted from the data containing both signal and background events, by fitting simulated MC events, that are known to be either signal or background, to the experimental data. A short overview of the analysis procedure is given in the following.

At first, the $B^0 \rightarrow D^{*-}\pi^+ \rightarrow \left(\bar{D}^0\pi_s^-\right)\pi^+$ decays for four different modes of D^0 decays are reconstructed from raw data. Next, signal and background templates of MC simulation data are fitted to the real detector data in order to determine the amount of signal contained in it. As a validation of the fitting procedure, a pull distribution test is performed using toy MC data. Subsequently, the yield-ratios are calculated from the information gather by the previous fits.

Since for the number of signal events N_{Sig} the relation

$$N_{\text{Sig}} = N_{B\bar{B}} \cdot \prod_i Br(i) \cdot \epsilon \tag{5.1}$$

holds, where the product is taken over the branching fractions $Br(i)$ of all sub-decays of the decay chain, $N_{B\bar{B}}$ is the number of $B\bar{B}$ events and ϵ is the detector efficiency, the yield-ratio

$$y = \frac{N_{\text{RE, Sig}}}{N_{\text{MC, Sig}}} \propto \frac{\epsilon_{\text{RE}}}{\epsilon_{\text{MC}}}, \tag{5.2}$$

is an appropriate measure for the relative slow pion tracking efficiency. The above formula also shows, that the yield-ratio can diverge from 1 if the branching fractions in the MC simulation do not match the real values, even if the efficiencies would be equal. Due to the assumption of a good agreement between the MC and experimental data for slow pions with a rather high momentum, the yield-ratios are scaled with respect to the normalized yield-ratio in the highest bin.

These yield-ratios and their uncertainties for different modes are weighted according to their uncertainties to obtain a better result. This weighting method is tested with a χ^2 calculation. Finally, in order to obtain a result for the global slow pion tracking efficiency uncertainty, the weighted yield-ratio uncertainties are weighted again, however, this time with respect to the number of events per

p_{π_s} bin. A simplified flow chart of the analysis process is shown in figure 5.1. In this figure, the green squares indicate processes on the computer cluster GRID, blue squares are steps performed on a local machine and the red one is the end result.
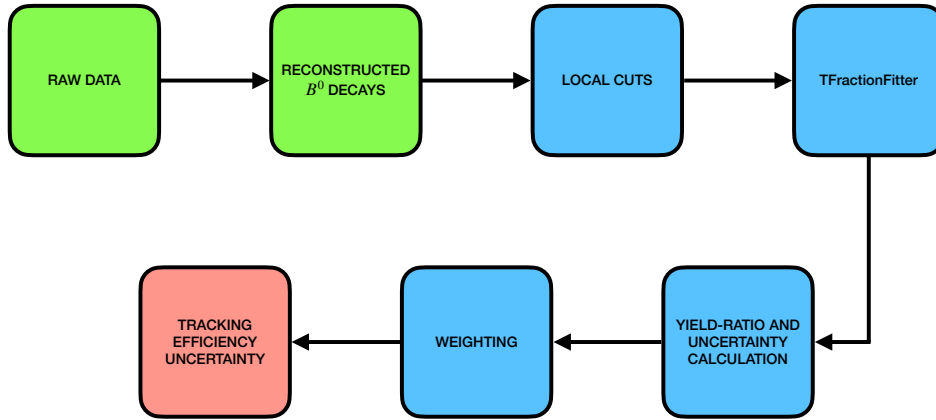
Figure 5.1: Overview of the analysis procedure.

5.1 Reconstruction

The analysis is based on experimental data that has been collected in the time between 2019 and 2020 at Belle II[1] and data from MC simulations. The real data set has an integrated luminosity of 72 fb^{-1}, of which 62.8 fb^{-1} are on-resonance and 9.2 fb^{-1} off-resonance data. The 62.8 fb^{-1} $\Upsilon(4S)$ data corresponds with $(68.21 \pm 0.06(\text{stat.}) \pm 0.78(\text{syst.})) \cdot 10^6$ $B\bar{B}$ events [18]. For the MC simulation data, subsets of the MC13a data set with an integrated luminosity of 200 fb^{-1} are used. These subsets are `mixed`, `charged`, u$\bar{\text{u}}$, d$\bar{\text{d}}$, c$\bar{\text{c}}$, s$\bar{\text{s}}$ and `taupair` samples.

The slow pion tracking efficiency analysis in this thesis is based on the slow pions origination from the decay $D^{*-} \to \bar{D}^0 \pi_s^-$. For the subsequent D^0 decays, four different modes have been taken into account. Starting from the B^0 mesons produced at Belle II, the decay chains for the four modes are depicted in figure 5.2.

Utilizing the Belle II analysis software framework (`basf2` [31]), the B^0 mesons are reconstructed from the final state particles – kaons and pions – in reverse order. At first, the D^0 meson is built from $K^{\pm}$, K_s, $\pi^{\pm}$ and π^0, depending on the mode. Next, the D^0 meson is combined with the slow pion π_s to the D^* meson. Finally, the B^0 meson is reconstructed from the D^* meson and another pion.

These instructions for `basf2` are written into a `python` script. It is commonly known as steering file, since it provides a rather human-readable interface that takes care of the orchestration of the underlying, complex and highly optimized `C++` code. The steering file includes all instructions and information needed in order to reconstruct the involved particles. This reconstruction process is performed on an international computing cluster called GRID, which has access to the raw data of the Belle II detector and MC simulations.

---

[1]Moriond 2021 dataset: experiments 8, 9 and 10 (proc 11) and 12 (buckets 9-15)

In order to reduce the amount of background events, multiple selections are applied to the particle candidates and events. Those so called cuts, which have been used for the reconstruction, are listed in table 5.1. Due to the working principle of `basf2`, these cuts are hard-coded into the steering file and changing them would require to rerun the whole analysis over the raw data on the GRID. Therefore, rather loose cuts are used in the steering file, with additional cuts being implemented at the later stage of fitting.

In table 5.1, dr is the radial distance from the interaction point in the r-ϕ plane, dz is the distance from the interaction point along the beam axis, thetaInCDCAcceptance demands that $17° < \theta < 150°$ (which means that the particle's polar angle is within the acceptance range of the CDC), nTracks is the number of reconstructed tracks per event and the visibleEnergyOfEventCMS is the visible energy per event in the center-of-mass frame.

The beam-energy constrained mass $M_{bc} = \sqrt{(E^*_{\text{beam}})^2 - (p^*_B)^2}$ and the energy difference $\Delta E = E^*_B - E^*_{\text{beam}}$ are the two variables that are later used to fit MC simulations to the real data [15].

$$D^0 \rightarrow K^- \pi^+$$

$$D^0 \rightarrow K^- \pi^+ \pi^- \pi^+$$

$$D^0 \rightarrow K^- \pi^+ \pi^0$$

$$D^0 \rightarrow K_s \pi^+ \pi^-$$
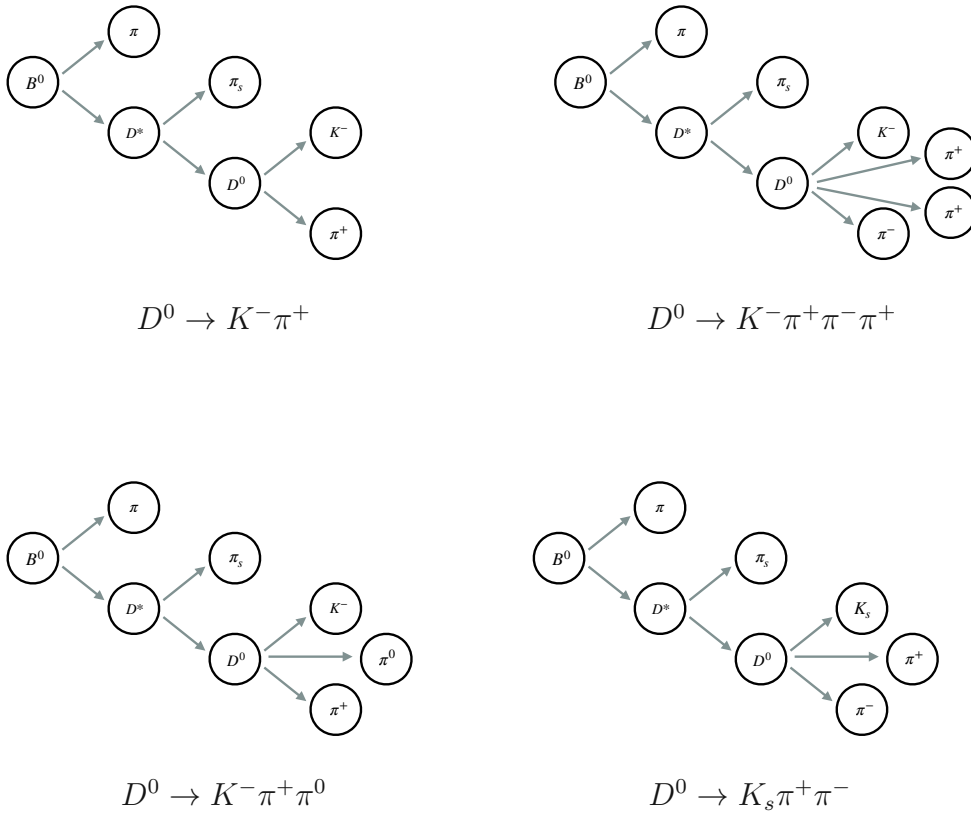
Figure 5.2: The four D^0 decay modes used in this thesis.

Where	Cuts
$K^{\pm}$, $\pi^{\pm}$	dr < 0.5 [cm] |dz| < 2 [cm] thetaInCDCAcceptance
π^0	Neutral performance group may 2020 recommendation
D^0	$1.84 < m_{D^0} < 1.89$ [GeV]
D^*	$0.134 < (m_{D^*} - m_{D^0}) < 0.158$ [GeV]
B^0	$M_{bc} > 5.25$ [GeV] $\|\Delta E\| < 0.3$ [GeV]
Event	nTracks > 3 visibleEnergyOfEventCMS > 4 [GeV]

Table 5.1: Steering file cuts.

5.2 TFractionFitter fits

TFractionFitter is a ROOT [16] class that is used to fit multiple fractions of data, for example signal and background components of MC simulations, to real data. It is based on the concepts described in reference [7]. To perform the fit, TFractionFitter maximizes the likelihood function in each bin.

In order to use TFractionFitter for this analysis, the MC data is split into signal and background subsets. Since the MC data includes the truth about the identity of each particle, this classification is possible. These two subsets provide the templates that are used to fit the signal and background fractions of the real data.

In this analysis, the M_{bc} distribution of the B^0 meson is used for the fit. The fits of the ΔE distribution provide a valuable option for cross checking the results at a later stage. Following the analyses in reference [32] and [11], a similar binning of the slow pions regarding their momentum into the bins $(0.05, 0.12)$, $(0.12, 0.16)$, $(0.16, 0.20)$ and $(0.20, 0.30)$ [GeV] is used. In addition to the hard-coded steering file cuts mentioned in table 5.1, different cuts for each mode are utilized before fitting, in order to suppress background events and improve the signal to background ratio. These cuts are listed in table 5.2, where dM describes the difference between the reconstructed and nominal mass of the particle. Figure 5.3 depicts the impact on the signal to background ratio of these additional cuts in the M_{bc} and ΔE distributions for the $D^0 \to K^- \pi^+$ mode of MC data.

Fit	Mode	Cuts
M_{bc}, ΔE	$D^0 \to K^- \pi^+$	$3.2429 < (m_{B^0} - m_{D^*}) < 3.301$ [GeV] $0.1429 < \mathrm{dM}_{D^*} < 0.1476$ [GeV]
M_{bc}, ΔE	$D^0 \to K^- \pi^+ \pi^- \pi^+$	$0.142 < \mathrm{dM}_{D^*} < 0.149$ [GeV]
M_{bc}, ΔE	$D^0 \to K^- \pi^+ \pi^0$	kaonID > 0.6 $p_{\pi_0} > 0.275$ [GeV] $0.1423 < \mathrm{dM}_{D^*} < 0.1488$ [GeV]
M_{bc}, ΔE	$D^0 \to K_s \pi^+ \pi^-$	$0.1423 < \mathrm{dM}_{D^*} < 0.1487$ [GeV]
M_{bc}	all	$M_{bc} > 5.265$ [GeV] $\lvert \Delta E \rvert < 0.1$ [GeV]
ΔE	all	$M_{bc} > 5.27$ [GeV] $\lvert \Delta E \rvert < 0.15$ [GeV]

Table 5.2: Additional cuts for each mode.

The resulting signal fractions η and the corresponding uncertainties σ_η of the M_{bc} and ΔE fits for each mode and bin are listed in the tables 5.3 and 5.4, respectively. Figures 5.4 to 5.11 show the corresponding post-fit distributions.
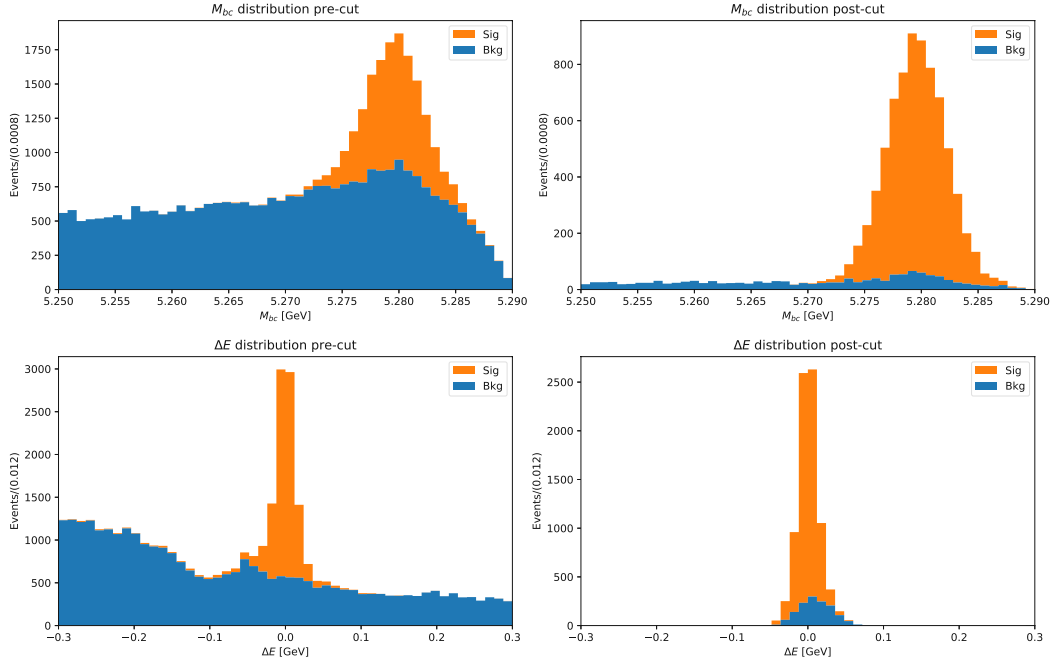
Figure 5.3: The consequences of the cuts in table 5.2 for the M_{bc} and ΔE distributions for the $D^0 \rightarrow K^- \pi^+$ mode of MC data.

Mode	Bin [GeV]	η	σ_η
$D^0 \rightarrow K^- \pi^+$	(0.05, 0.12)	0.6380	0.0491
	(0.12, 0.16)	0.6594	0.0382
	(0.16, 0.20)	0.6004	0.0390
	(0.20, 0.30)	0.6670	0.0319
$D^0 \rightarrow K^+ \pi^+ \pi^- \pi^+$	(0.05, 0.12)	0.3480	0.0291
	(0.12, 0.16)	0.3167	0.0204
	(0.16, 0.20)	0.2481	0.0203
	(0.20, 0.30)	0.3014	0.0186
$D^0 \rightarrow K^- \pi^+ \pi^0$	(0.05, 0.12)	0.2203	0.0277
	(0.12, 0.16)	0.2018	0.0182
	(0.16, 0.20)	0.1897	0.0184
	(0.20, 0.30)	0.1886	0.0153
$D^0 \rightarrow K_s \pi^+ \pi^-$	(0.05, 0.12)	0.2518	0.0540
	(0.12, 0.16)	0.2709	0.0349
	(0.16, 0.20)	0.1478	0.0349
	(0.20, 0.30)	0.2582	0.0321

Table 5.3: `TFractionFitter` output for the M_{bc} fit.

Mode	Bin [GeV]	η	σ_η
$D^0 \to K^-\pi^+$	(0.05, 0.12)	0.5805	0.0388
	(0.12, 0.16)	0.5656	0.0290
	(0.16, 0.20)	0.5426	0.0315
	(0.20, 0.30)	0.5702	0.0254
$D^0 \to K^-\pi^+\pi^-\pi^+$	(0.05, 0.12)	0.2437	0.0191
	(0.12, 0.16)	0.2574	0.0135
	(0.16, 0.20)	0.1972	0.0133
	(0.20, 0.30)	0.2533	0.0127
$D^0 \to K^-\pi^+\pi^0$	(0.05, 0.12)	0.1379	0.0185
	(0.12, 0.16)	0.1073	0.0115
	(0.16, 0.20)	0.1104	0.0121
	(0.20, 0.30)	0.1178	0.0098
$D^0 \to K_s\pi^+\pi^-$	(0.05, 0.12)	0.1924	0.0371
	(0.12, 0.16)	0.1595	0.0218
	(0.16, 0.20)	0.1491	0.0234
	(0.20, 0.30)	0.1799	0.0203

Table 5.4: `TFractionFitter` output for the ΔE fit.
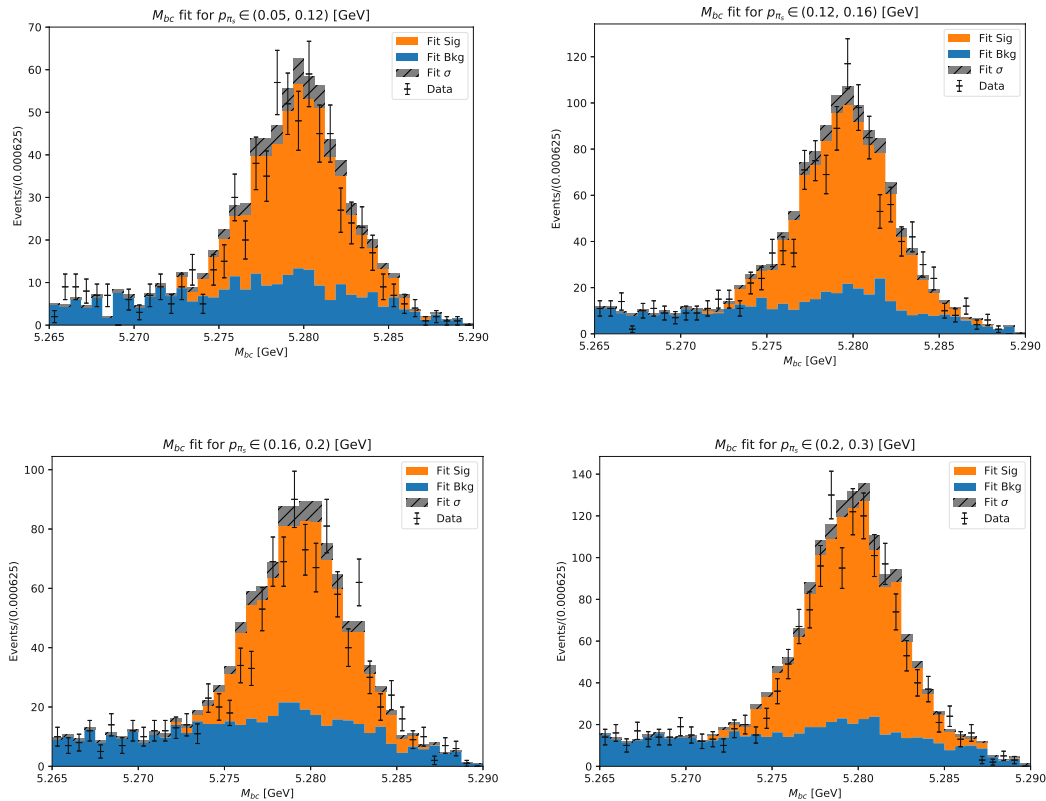
Figure 5.4: M_{bc} fits of the $D^0 \to K^-\pi^+$ mode.
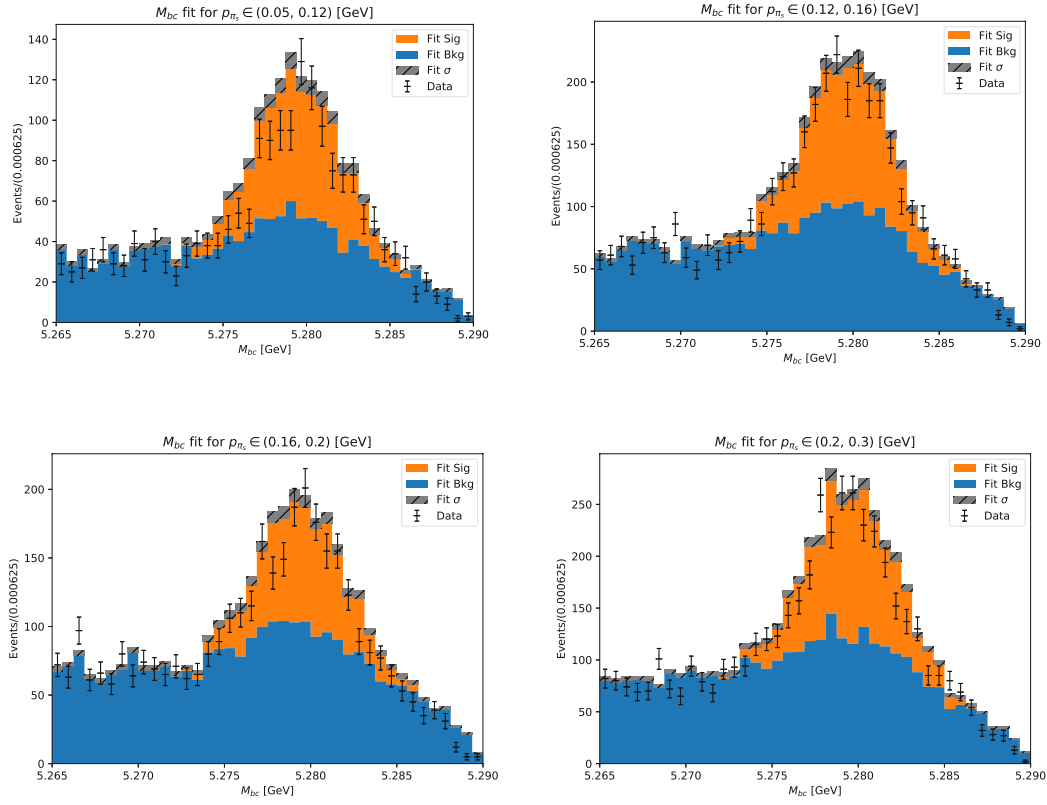
Figure 5.5: M_{bc} fits of the $D^0 \to K^- \pi^+ \pi^- \pi^+$ mode.
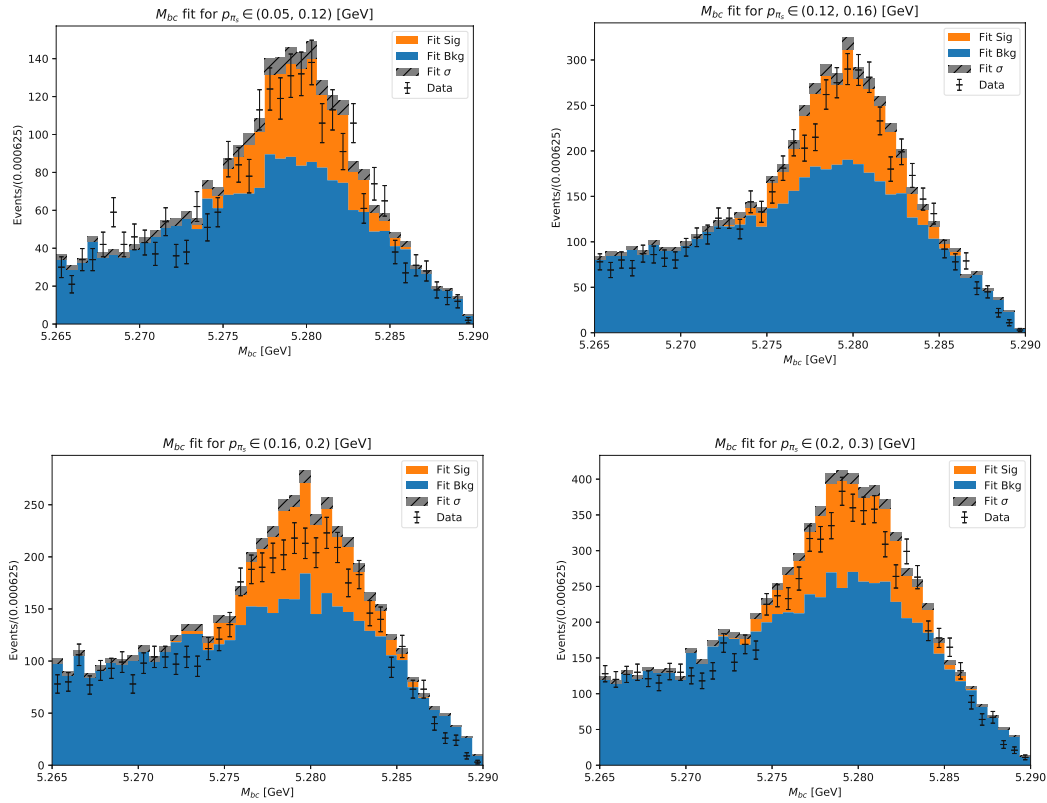
Figure 5.6: M_{bc} fits of the $D^0 \to K^- \pi^+ \pi^0$ mode.
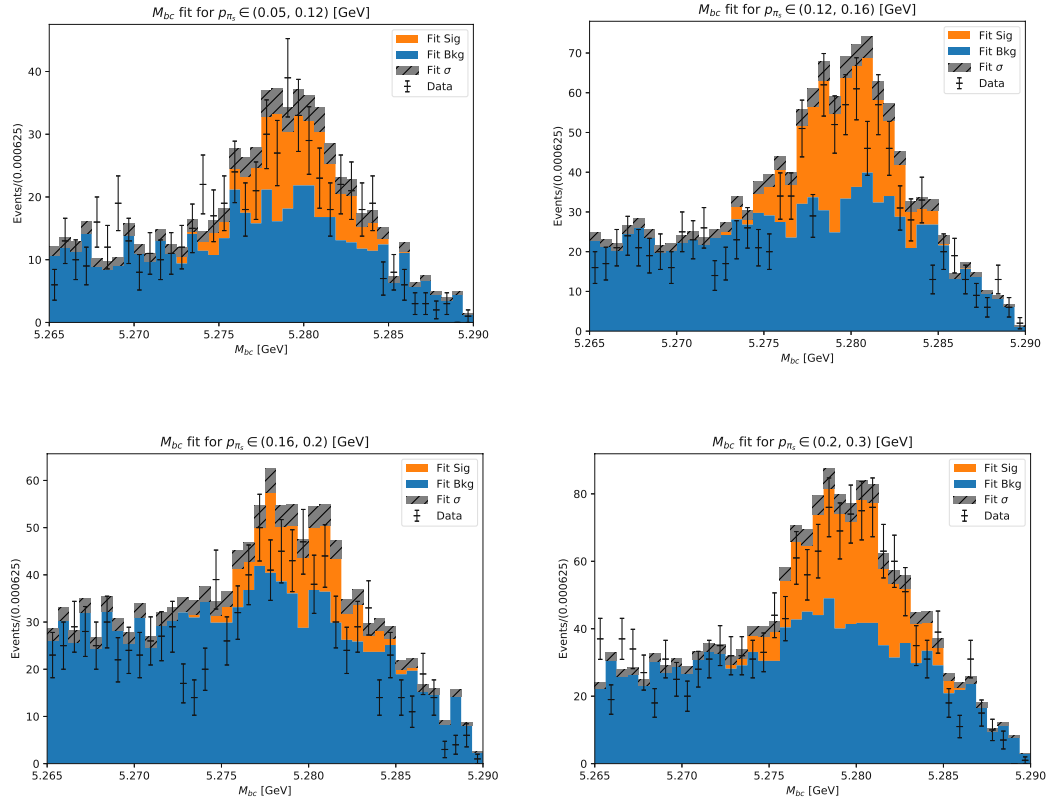
Figure 5.7: M_{bc} fits of the $D^0 \to K_s\pi^+\pi^-$ mode.
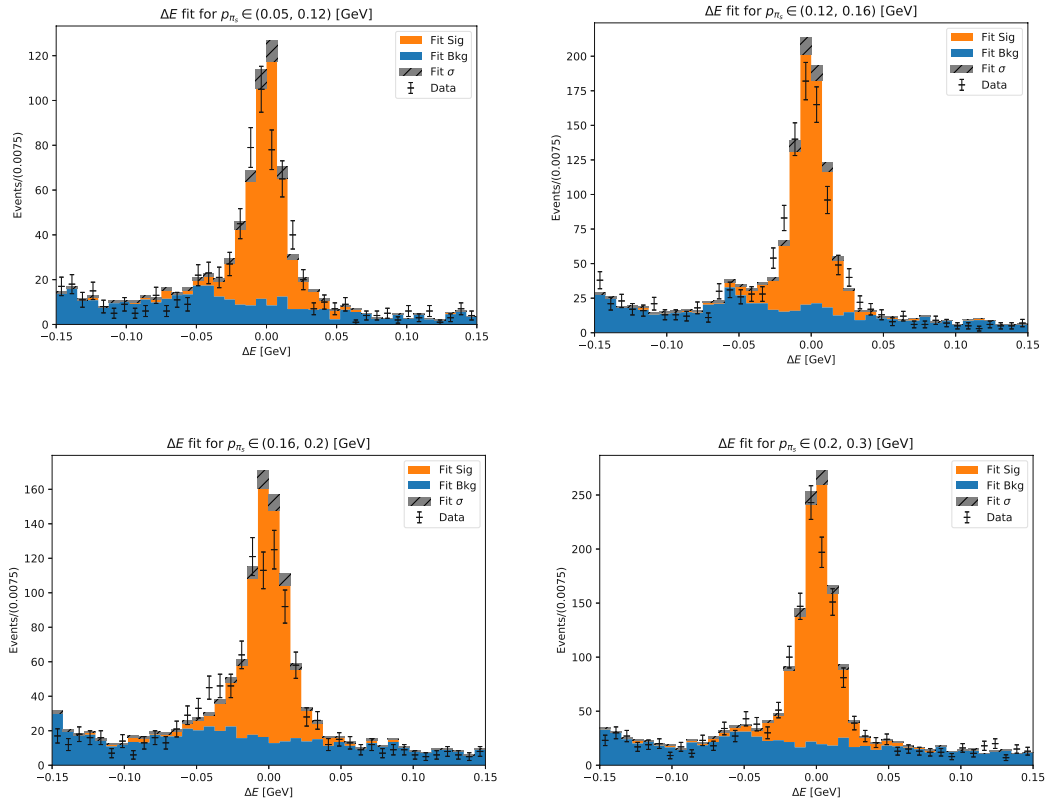
Figure 5.8: ΔE fits of the $D^0 \to K^-\pi^+$ mode.
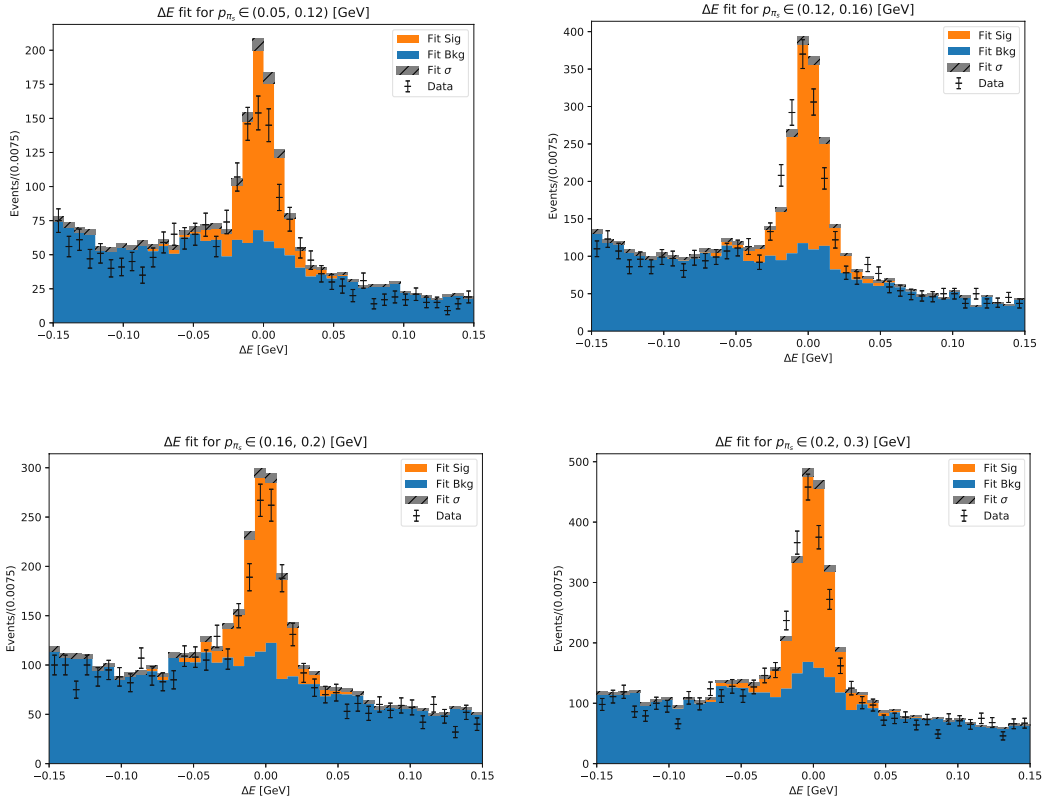
Figure 5.9: ΔE fits of the $D^0 \to K^- \pi^+ \pi^- \pi^+$ mode.
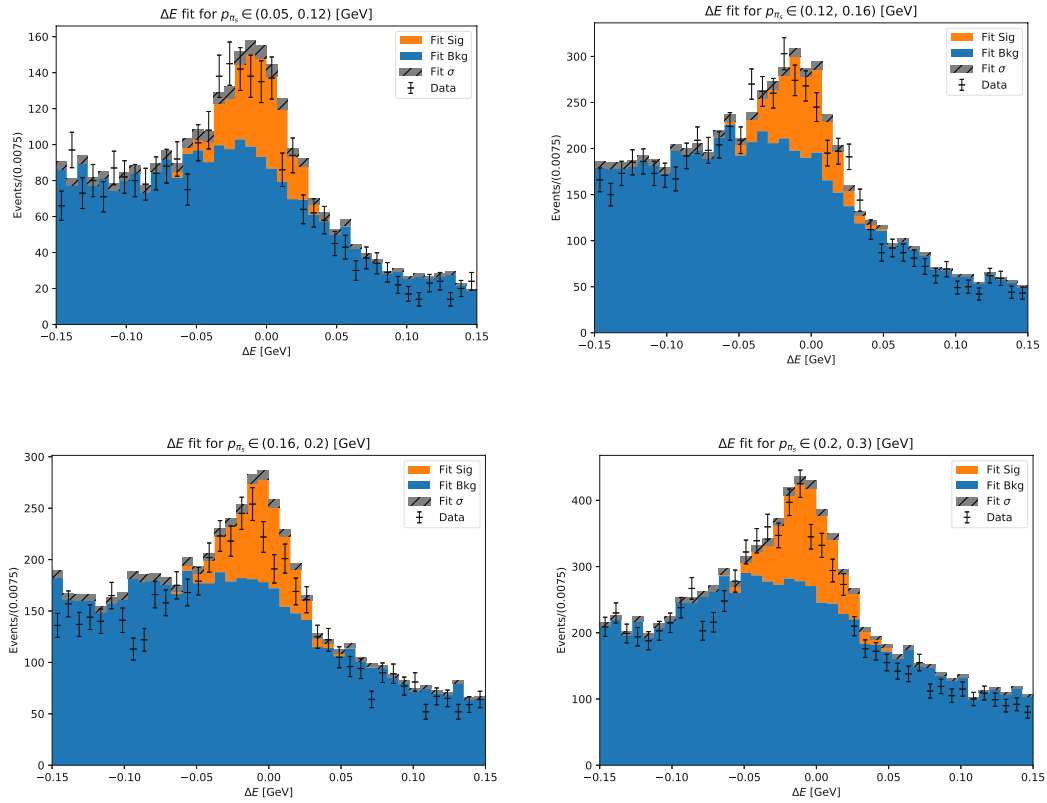
Figure 5.10: ΔE fits of the $D^0 \to K^- \pi^+ \pi^0$ mode.
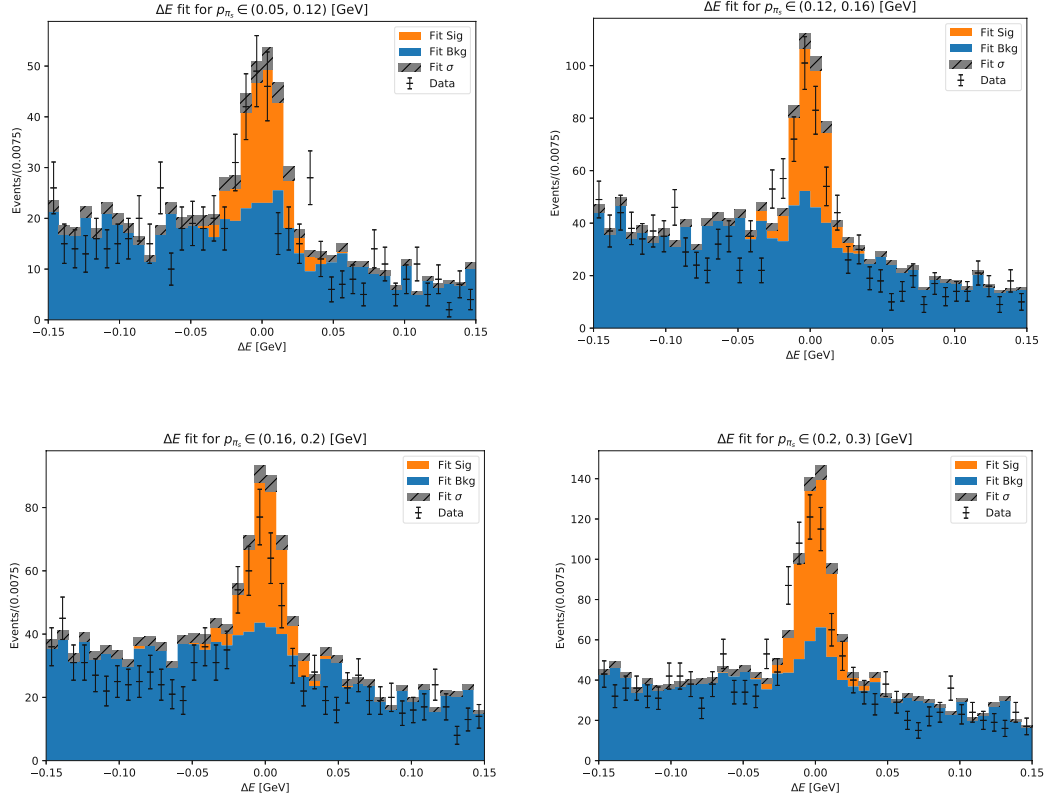
Figure 5.11: ΔE fits of the $D^0 \rightarrow K_s \pi^+ \pi^-$ mode.

5.3 Fit validation

In order to validate the fit, the pull distribution for toy MC models is calculated. At first, the M_{bc} and ΔE distributions of the signal and background MC data subsets are resampled under the assumption that the number of events per bin follows a Poisson distribution. This resampling is done by choosing a random variate of a Poisson probability distribution for each bin, where the parameter of the Poisson distribution is equal to the number of events in the bin. The procedure is performed 10000 times for the MC templates which are used for the fit and the MC data that is being fitted. Next, the pull distribution g is calculated by [22]

$$g = \frac{\hat{x} - x}{\sigma_{\hat{x}}}, \tag{5.3}$$

where $\hat{x}$ is the fitted signal fraction, $\sigma_{\hat{x}}$ its uncertainty and x the true signal fraction obtained from the MC truth as

$$x = \frac{N_{\text{MC, Sig}}}{N_{\text{MC}}}. \tag{5.4}$$

In the case of a valid fitting procedure, the pull distribution follows a Gaussian distribution with a mean value of $\mu = 0$ and a standard deviation of $\sigma = 1$, so $g \sim \mathcal{N}(0, 1)$. A deviation from $\mu = 0$ would imply an inherent bias of the fit and a value of $\sigma \neq 1$ would indicate that the uncertainty is either underestimated ($\sigma > 1$) or overestimated ($\sigma < 1$), respectively [44, 22]. The resulting normalized pull distribution with a Gaussian fit for the M_{bc} and ΔE `TFractionFitter` fits is depicted in figures 5.12 and 5.13. These figures also include the calculated values of μ and σ. Since $\mu \approx 0$ for all modes in both M_{bc}

and ΔE fits, the fit is considered to be unbiased. Furthermore, $\sigma \lesssim 1$ holds for all modes and therefore the fits are validated.
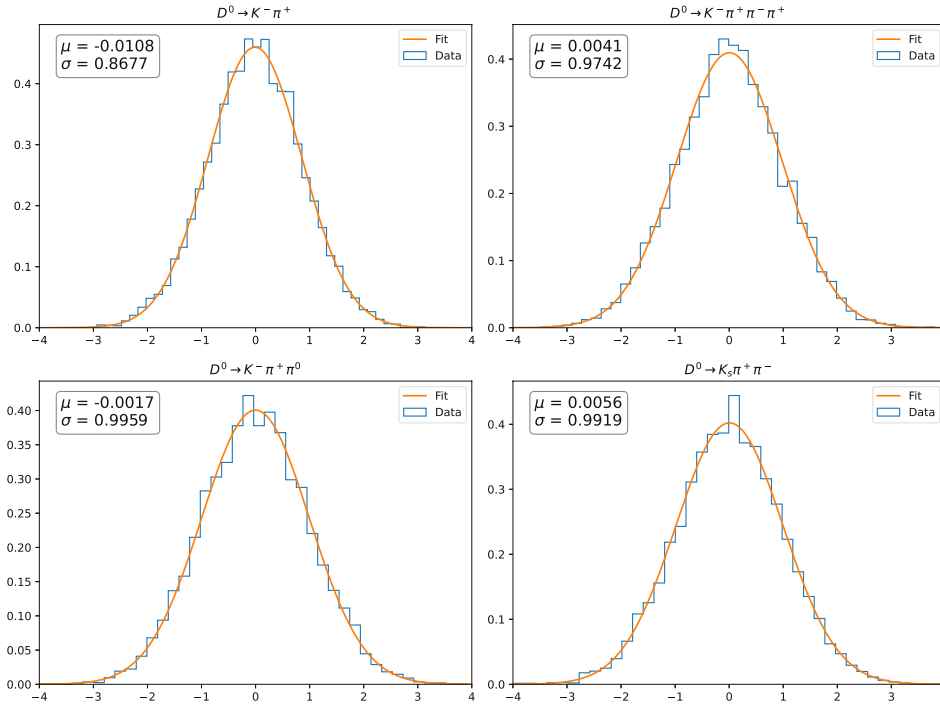
Figure 5.12: Pull distributions for the M_{bc} fit.
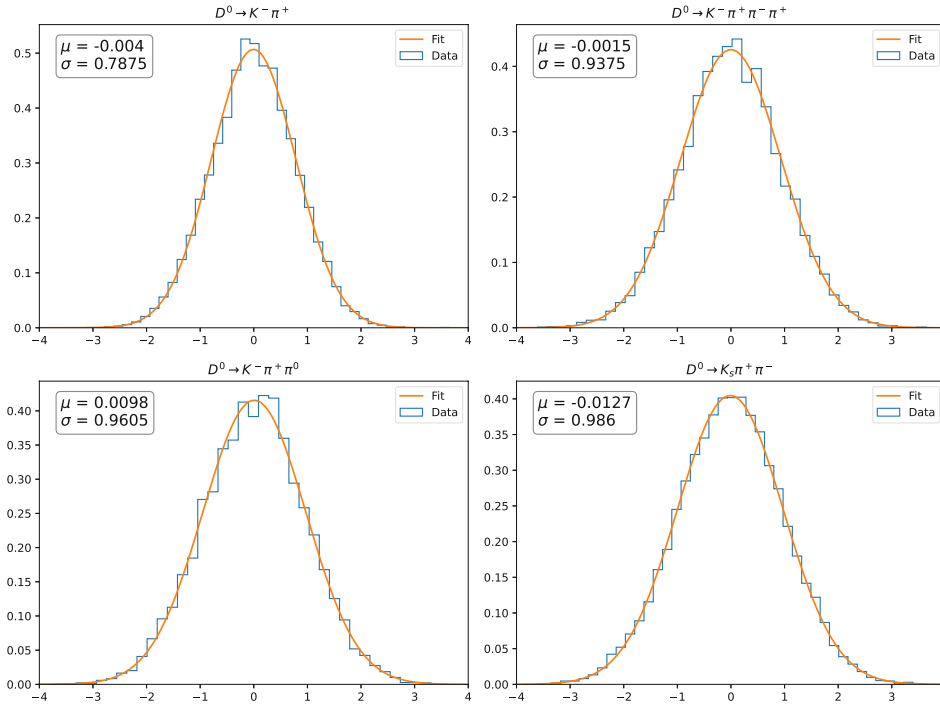
Figure 5.13: Pull distributions for the ΔE fit.

5.4   Yield-ratios

The yield-ratio y describes the ratio of the signal yield of the real data to the signal yield of the MC data. Therefore, the value of the yield-ratio provides information about the agreement of the reconstruction efficiency of the real and MC data. If $y = 1$, the real world data and the MC simulation are in perfect agreement. For $y < 1$, the proportion of signal events to all events is smaller for the real measurements than the simulation predicted. Respectively, $y > 1$ indicates a higher signal yield in the real data than the MC simulation. This could be due to a different than expected detector tracking efficiency or other parameters of the simulation that are not in alignment with the experiment.

From the result of `TFractionFitter` η and the knowledge of the number of events in the real and MC data, the yield-ratio is calculated as

$$y = \frac{N_{\text{RE, Sig}}}{N_{\text{MC, Sig}}} \tag{5.5}$$

$$= \frac{\eta \cdot N_{\text{RE}}}{N_{\text{MC, Sig}}}, \tag{5.6}$$

where N_{RE} is the number of total events in the real data set after applying all selections and $N_{\text{RE, Sig}}$ and $N_{\text{MC, Sig}}$ are the number of signal events in the real and MC data, respectively. Therefore, it is necessary to scale the MC data to match the real data luminosity, which is done by multiplying the number of MC events by $72/200$, since the luminosity of the real data is $72\ \text{fb}^{-1}$ and of the MC data $200\ \text{fb}^{-1}$. Furthermore, under the assumption of a good agreement between the MC simulation and the experimental data for slow pions on the upper end of their momentum spectrum, the yield-ratios are normalized with respect to the $(0.20, 0.30)$ [GeV] bin. A large deviation of the yield-ratio from one would necessitate the introduction of scaling factors to counteract it.

Due to `TFractionFitter` already taking into account different statistical uncertainties in its output value for the uncertainty σ_η, the error of the yield-ratios can be calculated by

$$\sigma_y = \frac{\sigma_\eta}{\eta} \cdot y. \tag{5.7}$$

As seen in figure 5.14, the yield-ratio of the mode $D^0 \to K_s \pi^+ \pi^-$ is not compatible with the other three modes because of the outlier in the $(0.16, 0.20)$ [GeV] bin and is therefore not taken into account for the subsequent analysis. This incompatibility could be due to the low number of events, however, further investigations were not part of this thesis. The yield-ratios for the ΔE fits are shown in figure 5.15.

		M_{bc} fit		ΔE fit	
Mode	Bin [GeV]	y	σ_y	y	σ_y
$D^0 \to K^-\pi^+$	(0.05, 0.12)	0.9285	0.0715	1.0015	0.0669
	(0.12, 0.16)	0.9908	0.0575	1.0076	0.0516
	(0.16, 0.20)	0.9594	0.0624	1.0038	0.0583
	(0.20, 0.30)	1.0000	0.0479	1.0000	0.0445
$D^0 \to K^+\pi^+\pi^-\pi^+$	(0.05, 0.12)	1.1217	0.0938	0.9401	0.0736
	(0.12, 0.16)	1.1590	0.0748	1.1222	0.0587
	(0.16, 0.20)	1.0500	0.0860	0.9908	0.0667
	(0.20, 0.30)	1.0000	0.0617	1.0000	0.0501
$D^0 \to K^-\pi^+\pi^0$	(0.05, 0.12)	1.0576	0.1328	1.0651	0.1426
	(0.12, 0.16)	1.0472	0.0942	0.9094	0.0975
	(0.16, 0.20)	1.1868	0.1154	1.1170	0.1220
	(0.20, 0.30)	1.0000	0.0813	1.0000	0.0835
$D^0 \to K_s\pi^+\pi^-$	(0.05, 0.12)	0.9416	0.2017	1.0069	0.1942
	(0.12, 0.16)	0.9158	0.1180	0.8408	0.1151
	(0.16, 0.20)	0.6143	0.1453	0.8947	0.1404
	(0.20, 0.30)	1.0000	0.1243	1.0000	0.1126

Table 5.5: Yield-ratios and uncertainties.
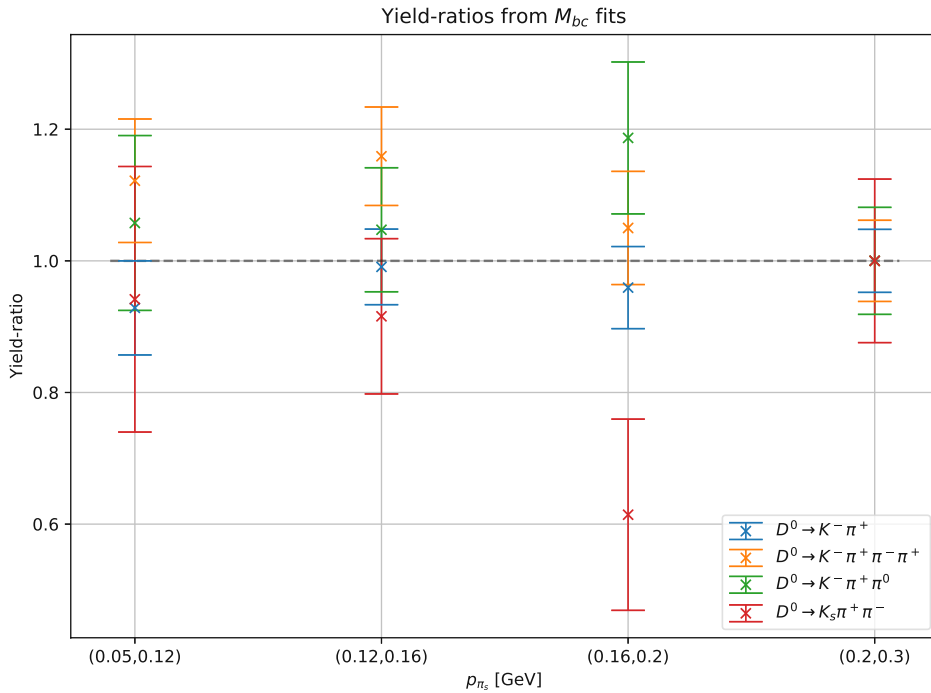
Figure 5.14: The yield-ratios from M_{bc} fits for four modes.
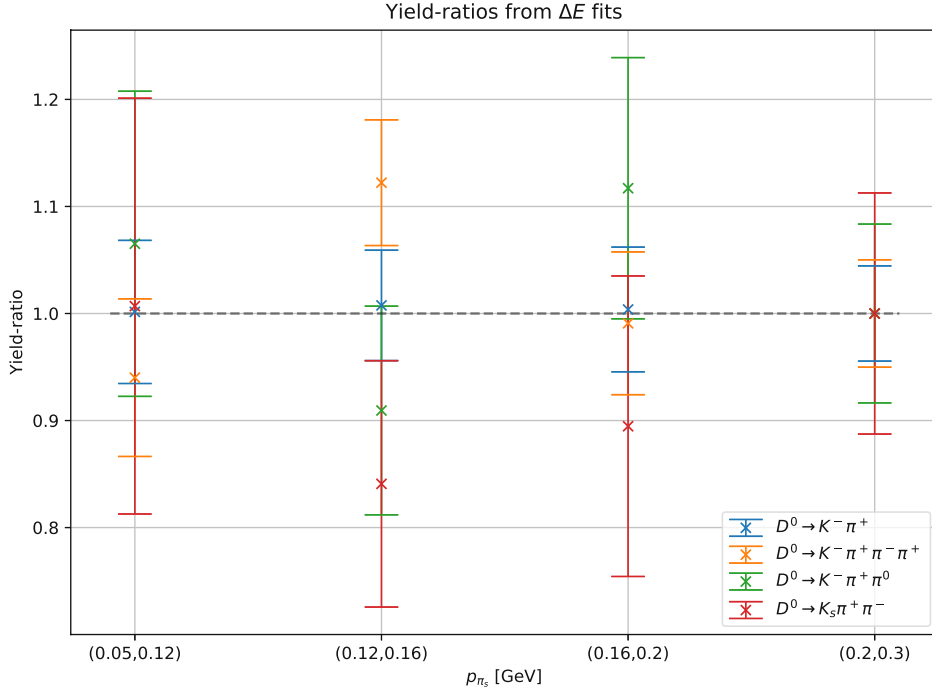
Figure 5.15: The yield-ratios from ΔE fits for four modes.

Next, the calculated yield-ratios y_i and variances σ_i^2 for the modes i are weighted for each bin using [44]

$$\hat{\mu} = \frac{1}{w} \sum_{i=1}^{3} w_i y_i, \tag{5.8}$$

$$w_i = \frac{1}{\sigma_i^2} \tag{5.9}$$

$$w = \sum_{i}^{n} w_i. \tag{5.10}$$

The corresponding standard deviation of $\hat{\mu}$ is given by

$$\hat{\sigma} = \frac{1}{\sqrt{w}}. \tag{5.11}$$

The results of this weighting procedure for the yield-ratios of the modes $D^0 \to K^-\pi^+$, $D^0 \to K^-\pi^+\pi^-\pi^+$, and $D^0 \to K^-\pi^+\pi^0$ are listed in table 5.6 and depicted in figure 5.16, respectively. Cross checking the M_{bc} with the ΔE results, a good agreement in all bins is observed, which validates the analysis up to this point.

Bin	M_{bc} fit		ΔE fit	
	$\hat{\mu}$	$\hat{\sigma}$	$\hat{\mu}$	$\hat{\sigma}$
$(0.05, 0.12)$	1.0085	0.0523	0.9835	0.0468
$(0.12, 0.16)$	1.0520	0.0410	1.0373	0.0360
$(0.16, 0.20)$	1.0221	0.0463	1.0118	0.0413
$(0.20, 0.30)$	1.0000	0.0343	1.0000	0.0309

Table 5.6: Weighted yield-ratios and their standard deviations.
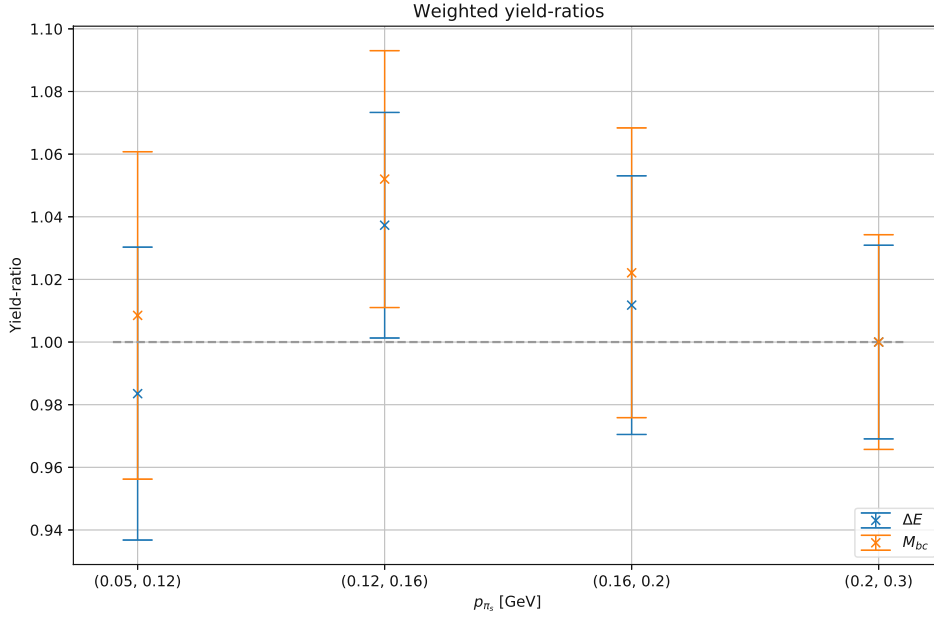
Figure 5.16: A comparison of the weighted yield-ratios from M_{bc} and ΔE fits.

5.5 χ^2 calculation

In order to validate the agreement of the weighted yield-ratios with the individual modes, the χ^2/n values are calculated for each bin using [44]

$$\frac{\chi^2}{n} = \frac{1}{n} \sum_{i=1}^{3} \left(\frac{y_i - \hat{\mu}}{\sigma_i} \right)^2, \tag{5.12}$$

where n is the number of degrees of freedom, y_i and σ_i are the yield-ratio and its uncertainty for the mode i in the bin, $\hat{y}$ is the weighted yield-ratio of the bin and the sum is over all i modes. For the calculation of three modes, the number of degrees of freedom is $n = 2$, since one degree of freedom is used by the calculation of the weighted yield-ratio. If $\chi^2/n \approx 1$, there is a good agreement between $\hat{\mu}$ and the yield-ratios of the individual modes in the bin, since for a large number of random independent Gaussian variables, the above sum converges to the probability density function of the $\chi^2(n)$ distribution divided by n [44]. The resulting χ^2/n values are shown in table 5.7.

Bin	M_{bc} χ^2/n	ΔE χ^2/n
$(0.05, 0.12)$	1.42	0.37
$(0.12, 0.16)$	1.59	2.07
$(0.16, 0.20)$	1.58	0.43
$(0.20, 0.30)$	0.00	0.00

Table 5.7: χ^2/n values for the M_{bc} und ΔE fits.

5.6   Results

Finally, since the momentum spectrum of the slow pions is not uniformly distributed, as depicted in figure 5.17, the distribution has to be taken into account for the uncertainty calculation. A large uncertainty in a sparsely populated momentum bin is not as problematic as it would be in a bin including a substantial number of events. Therefore, the weighted yield-ratios obtained in the previous section are weighted with the number of events per bin, which is shown in figure 5.17, in the slow pion momentum spectrum. This is done by simply calculating

$$\bar{\sigma} = \sum_{i=1}^{4} \lambda_i \cdot \hat{\sigma}_i, \tag{5.13}$$

where $\lambda_i = N_i/N$ is the ratio of the number of events in bin i, N_i, and the total number of events N and $\hat{\sigma}_i$ is the weighted uncertainty in bin i. The values of λ_i are $\{0.15, 0.27, 0.22, 0.36\}$.

Therefore the result of the uncertainty of the slow pion tracking efficiency is calculated to be

$$\bar{\sigma} = 4.06\% \tag{5.14}$$

for the M_{bc} fit and for the ΔE fit

$$\bar{\sigma} = 3.66\%. \tag{5.15}$$

Since the ΔE based yield-ratio calculation merely serves as a cross check for the M_{bc} based one and due to the worse χ^2/n values of the ΔE procedure, only the $\bar{\sigma} = 4.06\%$ result from the M_{bc} fit is to be quoted.

Comparing the $\bar{\sigma} = 4.06\%$ result to the currently proposed uncertainty values from the independently performed analysis by Chaoyi Lyu [11] of about 5-6% per bin, it seems to be plausible. The result of this thesis also manages to surpass the present uncertainty of about 10% by more than a factor of 2. Furthermore, the weighted yield-ratios of this analysis and Chaoyi Lyu's are compatible within the margins of error of $\pm 1\sigma$.
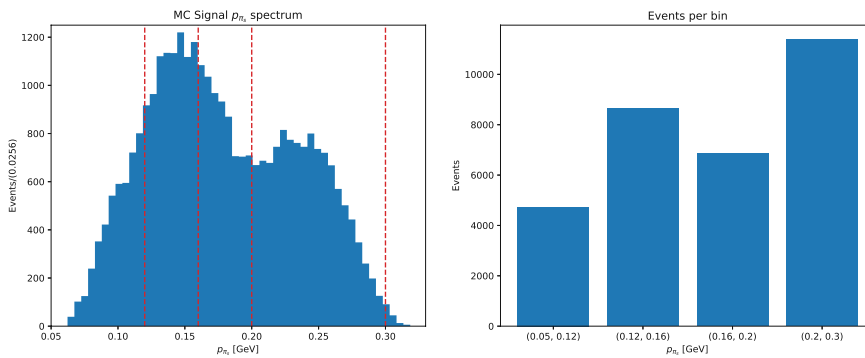
Figure 5.17: π_s momentum spectrum with the bin edges indicated (left). The number of events per p_{π_s} bin (right).

Chapter 6

Summary

In this thesis, the uncertainty of the reconstruction efficiency for slow pions at Belle II was analyzed. The analysis is based on the Moriond 2021 data set, which has been collected at Belle II in the years 2019 and 2020, and data from Monte Carlo simulations. Their integrated luminosity is 72 fb^{-1} for the real data and 200 fb^{-1} for the MC data.

At first, $B^0 \to D^{*-}\pi^+ \to \left(\bar{D}^0 \pi_s^-\right)\pi^+$ decays, with four different modes of D^0 decays ($D^0 \to K^-\pi^+$, $D^0 \to K^-\pi^+\pi^-\pi^+$, $D^0 \to K^-\pi^+\pi^0$ and $D^0 \to K_s\pi^+\pi^-$), were reconstructed. Using the MC-truth information of the MC data, multiple cuts have been applied for each mode in order to suppress background events and increase the signal-to-background ratio.

Next, to extract the number of signal events out of all events from the real data, `TFractionFitter`, a bin-wise likelihood fitting algorithm, was utilized to fit MC signal and background data templates to the real data. The fits were performed on the M_{bc} and ΔE distributions of the reconstructed B^0 mesons. The final results were obtained from the M_{bc} fits and the ΔE fits were used to cross check the results. Before the fit, the events were binned with regard to their slow pion momentum into $(0.05, 0.12)$, $(0.12, 0.16)$, $(0.16, 0.20)$ and $(0.20, 0.30)$ [GeV] bins. The ratio of the signal yields for all four modes and bins of both data sets were calculated using the results from the fits. Assuming a good agreement between the simulation and experimental data for slow pions with a momentum on the upper end of their possible range, the yield-ratios were normalized to the $(0.20, 0.30)$ [GeV] bin.

After examining the compatibility of the yield-ratios of the four modes, the $D^0 \to K_s\pi^+\pi^-$ mode has been discarded due to an outlier in one of the bins. The yield-ratios and their respective uncertainties of the other three modes were weighted for each bin, taking into account their uncertainties.

Since no substantial deviation of the weighted yield-ratios from unity has been observed in all bins, there was no necessity to introduce correction factors to counteract differences in the signal yields for the real and simulated data.

Furthermore, the number of events is not uniformly distributed across the slow pion momentum bins. Therefore, the mode-weighted yield-ratio uncertainties were weighted a second time, however, this time with regard to the number of events per p_{π_s} bin, as large uncertainty with only a few events could be compensated by a densely populated bin with a smaller uncertainty.

The result of this weighting is a global uncertainty factor for the slow pion tracking-efficiency at Belle II. Is has been calculated to be

$$\sigma_{p_{\pi_s}} = 4.06\,\%, \tag{6.1}$$

which surpasses the previous result of about 10% [21] and is in good agreement with current independent results of Chaoyi Lyu [11]. Additionally, the weighted yield-ratios obtained in this thesis and Chaoyi Lyu's results are compatible within the margins of error of $\pm 1\sigma$.

Hopefully, this analysis of the slow pion tracking efficiency uncertainty is able to provide at least a small, valuable contribution to the quest of determining more precise $|V_{cb}|$ results at Belle II in the future.

Acknowledgments

I am dedicating special thanks to my parents and siblings for their unconditional support throughout my whole life.

Furthermore, I would like to thank my supervisor Christoph Schwanda for his outstanding dedication, guidance and countless insights over the course of this thesis. Last, but definitely not least, I am thankful for the whole Belle II semileptonic group at HEPHY for always helping me out with advice when it was needed.

List of Figures

List of Tables

Bibliography

[1]   Nobel Prize Outreach AB 2021. *Nobel Prize Press Release 2008*. Sept. 2021. URL: https://www.nobelprize.org/prizes/physics/2008/press-release/ (visited on 09/22/2021).

[2]   T. Abe et al. *Belle II Technical Design Report*. 2010. arXiv: 1011.0352 [physics.ins-det].

[3]   I. Adachi et al. "Detectors for extreme luminosity: Belle II". In: *Nuclear Instruments and Methods in Physics Research Section A: Accelerators, Spectrometers, Detectors and Associated Equipment* 907 (2018). Advances in Instrumentation and Experimental Methods (Special Issue in Honour of Kai Siegbahn), pp. 46–59. ISSN: 0168-9002. DOI: https://doi.org/10.1016/j.nima.2018.03.068. URL: https://www.sciencedirect.com/science/article/pii/S0168900218304200.

[4]   Kazunori Akai, Kazuro Furukawa, and Haruyo Koiso. "SuperKEKB collider". In: *Nuclear Instruments and Methods in Physics Research Section A: Accelerators, Spectrometers, Detectors and Associated Equipment* 907 (Nov. 2018), pp. 188–199. ISSN: 0168-9002. DOI: 10.1016/j.nima.2018.08.017. URL: http://dx.doi.org/10.1016/j.nima.2018.08.017.

[5]   T. Alexopoulos et al. "Implementation of the Legendre Transform for track segment reconstruction in drift tube chambers". In: *Nucl. Instrum. Meth. A* 592 (2008), pp. 456–462. DOI: 10.1016/j.nima.2008.04.038.

[6]   S Baird. *Accelerators for pedestrians; rev. version*. Tech. rep. Geneva: CERN, Feb. 2007. URL: https://cds.cern.ch/record/1017689.

[7]   Roger Barlow and Christine Beeston. "Fitting using finite Monte Carlo samples". In: *Computer Physics Communications* 77.2 (1993), pp. 219–228. ISSN: 0010-4655. DOI: https://doi.org/10.1016/0010-4655(93)90005-W. URL: https://www.sciencedirect.com/science/article/pii/001046559390005W.

[8]   Matthias Bartelmann et al. *Theoretische Physik*. 1st ed. Springer Spektrum, 2015. ISBN: 978-3-642-54617-4. DOI: 10.1007/978-3-642-54618-1.

[9]   Christoph Berger. *Elementarteilchenphysik. Von den Grundlagen zu den modernen Experimenten*. 3rd ed. Springer Spektrum, 2014. ISBN: 978-3-642-41752-8. DOI: 10.1007/978-3-642-41753-5.

[10]   Niklaus Berger et al. "A new three-dimensional track fit with multiple scattering". In: *Nuclear Instruments and Methods in Physics Research Section A: Accelerators, Spectrometers, Detectors and Associated Equipment* 844 (2017), pp. 135–140. ISSN: 0168-9002. DOI: https://doi.org/10.1016/j.nima.2016.11.012. URL: https://www.sciencedirect.com/science/article/pii/S016890021631138X.

[11] Florian Bernlochner and Chaoyi Lyu. *Status of Slow π Tracking Efficiency*. Pre-B2GM tracking meeting. Oct. 2021.

[12] Valerio Bertacchi et al. "Track finding at Belle II". In: *Computer Physics Communications* 259 (Feb. 2021), p. 107610. ISSN: 0010-4655. DOI: `10.1016/j.cpc.2020.107610`. URL: `http://dx.doi.org/10.1016/j.cpc.2020.107610`.

[13] Tadeas Bilka et al. *Implementation of GENFIT2 as an experiment independent track-fitting framework*. 2019. arXiv: `1902.04405`.

[14] Nils Lennart Braun. "Combinatorial Kalman Filter and High Level Trigger Reconstruction for the Belle II Experiment". PhD thesis. Karlsruher Institut für Technologie (KIT), 2019. 189 pp. DOI: `10.5445/IR/1000089317`.

[15] Jolanta Brodzicka et al. *Physics Achievements from the Belle Experiment*. 2012. arXiv: `1212.5342 [hep-ex]`.

[16] Rene Brun and Fons Rademakers. "ROOT — An object oriented data analysis framework". In: *Nuclear Instruments and Methods in Physics Research Section A: Accelerators, Spectrometers, Detectors and Associated Equipment* 389.1 (1997). New Computing Techniques in Physics Research V, pp. 81–86. ISSN: 0168-9002. DOI: `https://doi.org/10.1016/S0168-9002(97)00048-X`. URL: `https://www.sciencedirect.com/science/article/pii/S016890029700048X`.

[17] Irinel Caprini, Laurent Lellouch, and Matthias Neubert. "Dispersive bounds on the shape of form factors". In: *Nuclear Physics B* 530.1-2 (Oct. 1998), pp. 153–181. ISSN: 0550-3213. DOI: `10.1016/s0550-3213(98)00350-2`. URL: `http://dx.doi.org/10.1016/S0550-3213(98)00350-2`.

[18] Claudia Cecchi et al. "B counting measurement in "Moriond 2021" Belle II dataset". In: (Mar. 2021).

[19] CERN. *LHC Season 2. facts & figures*. URL: `https://home.cern/sites/home.web.cern.ch/files/2018-07/factsandfigures-en_0.pdf` (visited on 09/24/2021).

[20] User: Chetvorno. *Linear accelerator animation*. 2018. URL: `https://en.wikipedia.org/wiki/File:Linear_accelerator_animation_16frames_1.6sec.gif` (visited on 09/08/2021).

[21] Belle II Collaboration et al. *Studies of the semileptonic $\bar{B}^0 \to D^{*+}\ell^-\bar{\nu}_\ell$ and $B^- \to D^0\ell^-\bar{\nu}_\ell$ decay processes with 34.6 fb^{-1} of Belle II data*. 2020. arXiv: `2008.07198 [hep-ex]`.

[22] Luc Demortier and Louis Lyons. *Everything you always wanted to know about pulls*. Version 3. Apr. 2008. URL: `https://lucdemortier.github.io/assets/papers/cdf5776_pulls.pdf` (visited on 11/17/2021).

[23] Wolfgang Demtröder. *Experimentalphysik 2. Elektrizität und Optik*. 6th ed. Springer-Verlag Berlin Heidelberg, 2013. ISBN: 978-3-642-29943-8. DOI: `10.1007/978-3-642-29944-5`.

[24] W. Dungel et al. "Measurement of the form factors of the decay $B^0 \to D^{*-}l^+\nu_l$ and determination of the CKM matrix element $|V_{cb}|$". In: *Physical Review D* 82.11 (Dec. 2010). ISSN: 1550-2368. DOI: `10.1103/physrevd.82.112007`. URL: `http://dx.doi.org/10.1103/PhysRevD.82.112007`.

[25] Richard Feynman, Robert Leighton, and Matthew Sands. *The Feynman Lectures on Physics. The New Millennium Edition Vol II: Mainly Electromagnetism and Matter*. Basic Books, 2011. ISBN: 978-0-465-02494-0.

[26] R. Frühwirth. "Application of Kalman filtering to track and vertex fitting". In: *Nucl. Instrum. Meth. A* 262 (1987), pp. 444–450. DOI: `10.1016/0168-9002(87)90887-4`.

[27] Yoshihito Iwasaki et al. "Level 1 Trigger System for the Belle II Experiment". In: vol. 58. June 2010, pp. 1–9. DOI: `10.1109/RTC.2010.5750454`.

[28] C.-H. Kim et al. "Trigger slow control system of the Belle II experiment". In: *Nuclear Instruments and Methods in Physics Research Section A: Accelerators, Spectrometers, Detectors and Associated Equipment* 1014 (Oct. 2021), p. 165748. ISSN: 0168-9002. DOI: `10.1016/j.nima.2021.165748`. URL: `http://dx.doi.org/10.1016/j.nima.2021.165748`.

[29] Dmitri Kotchetkov et al. "Front-end electronic readout system for the Belle II imaging Time-Of-Propagation detector". In: *Nuclear Instruments and Methods in Physics Research Section A: Accelerators, Spectrometers, Detectors and Associated Equipment* 941 (Oct. 2019), p. 162342. ISSN: 0168-9002. DOI: `10.1016/j.nima.2019.162342`. URL: `http://dx.doi.org/10.1016/j.nima.2019.162342`.

[30] E Kou et al. "The Belle II Physics Book". In: *Progress of Theoretical and Experimental Physics* 2019.12 (Dec. 2019). ISSN: 2050-3911. DOI: `10.1093/ptep/ptz106`. URL: `http://dx.doi.org/10.1093/ptep/ptz106`.

[31] Thomas Kuhr et al. "The Belle II Core Software". In: (July 2018). URL: `https://docs.belle2.org/record/1044/` (visited on 11/13/2021).

[32] S. Maity et al. "Study of slow-pion tracking efficiency using $B^0 \to D^*\pi$ and $B^0 \to D^*\rho$ decays". In: (2020). Belle II note 2020-036.

[33] Manca Mrvar. "Calibration of aerogel ring-imaging Cherenkov detector in Belle II spectrometer". Presented on 10 01 2019. PhD thesis. Ljubljana, Slovenia: Ljubljana, Slovenia, University of Ljubljana, 2019.

[34] NASA. *WFI-DEPFET sensor*. URL: `https://asd.gsfc.nasa.gov/archive/ixo/images/technology/details/wfihxi_depfetSchematic.jpg` (visited on 09/16/2021).

[35] Antonio Pich. *The Standard Model of Electroweak Interactions*. 2007. arXiv: `0705.4264 [hep-ph]`.

[36] Petar Rados. *Belle II Tracking Performance. CHEP 2019*. Nov. 2019. URL: `https://indico.cern.ch/event/773049/contributions/3474751/attachments/1940572/3217515/Belle2_TrackPerf_CHEP_7Nov2019.pdf` (visited on 09/19/2021).

[37] Michael Schmid. *Wire chamber schematic*. 2005. URL: `https://en.wikipedia.org/wiki/File:Wire_chamber_schematic.svg` (visited on 09/06/2021).

[38] *Standard Model of Elementary Particles*. 2019. URL: `https://en.wikipedia.org/wiki/File:Standard_Model_of_Elementary_Particles.svg` (visited on 07/27/2021).

[39] Henrikas Svidras. *The Central Drift Chamber of Belle 2. 5th Belle II Starterkit Workshop.* Jan. 2020. URL: https://indico.belle2.org/event/1307/sessions/378/attachments/3070/5652/CDC_B2SK.pdf (visited on 09/19/2021).

[40] Mark Thomson. *Modern Particle Physics.* Cambridge University Press, 2013. DOI: 10.1017/CBO9781139525367.

[41] Katsuo Tokushuku. *Belle II/SuperKEKB perspective from KEK.* 2020. URL: https://indico.bnl.gov/event/9843/contributions/42497/attachments/31087/49083/KEK-perspective-tokushuku_v4.pdf (visited on 09/15/2021).

[42] Wolfgang Waltenberger. "RAVE—A Detector-Independent Toolkit to Reconstruct Vertices". In: *IEEE Transactions on Nuclear Science* 58.2 (2011), pp. 434–444. DOI: 10.1109/TNS.2011.2119492.

[43] C. S. Wu et al. "Experimental Test of Parity Conservation in Beta Decay". In: *Phys. Rev.* 105 (4 Feb. 1957), pp. 1413–1415. DOI: 10.1103/PhysRev.105.1413. URL: https://link.aps.org/doi/10.1103/PhysRev.105.1413.

[44] P.A. Zyla et al. "Review of Particle Physics". In: *PTEP* 2020.8 (2020), p. 083C01. DOI: 10.1093/ptep/ptaa104.